3. Electric Machinery Research and Technology Development

3.1 Uncluttered CVT Machine

Principal Investigator: John Hsu
Oak Ridge National Laboratory
National Transportation Research Center
2360 Cherahala Boulevard
Knoxville, TN 37932
Voice: 865-946-1325; Fax: 865-946-1210; E-mail: hsujs @ornl.gov

DOE Technology Development Manager: Susan A. Rogers
Voice: 202-586-8997; Fax: 202-586-1600; E-mail: Susan.Rogers@ee.doe.gov

ORNL Program Manager: Mitch Olszewski
Voice: 865-946-1350; Fax: 865-946-1262; E-mail: olszewskim@ornl.gov

Objectives

Develop a new machine that combines motor and generator into one unit with a continuously variable transmission (CVT).

- The design enables additional torque coupling between the two rotors for producing more wheel torque.
- The combination of a motor and generator into one machine with only a single permanent magnet rotor has the potential to be simpler and less costly than conventional CVTs.
- The output power of the uncluttered rotor can be doubled.

Approach

- The uncluttered rotor CVT machine project has an ultimate multi-year goal of producing an electric machine with double the power density of current-technology machines at a given rotor speed.
- The principle of the uncluttered rotor was proved in FY 2001 through modification and testing of an induction machine with a specially wound rotor. The FY 2006 effort completed the second step of the proof-of-concept machine and eliminated the windings in the uncluttered rotor.
- The specific FY 2006 goal was to design and build a proof-of-concept uncluttered rotor without windings and a half stator that couples with the uncluttered rotor.

Major Accomplishments

- The design of the proof-of-concept uncluttered rotor without windings and a half stator wound core to couple to the uncluttered rotor was completed. The uncluttered rotor and its half stator were fabricated, and the uncluttered rotor teeth were machined out of solid steel instead of laminations in order to lower costs for the proof-of-concept prototype. The uncluttered rotor concept for the brushless rotating stator (or armature) was proved through tests conducted on the prototype.

Technical Discussion

The physics of the uncluttered CVT can be understood through an examination of a conventional motor. Figure 1 shows that for any conventional motor, the stator sees a counter-torque to the shaft torque. The magnitude of the stator torque is the same as that of the shaft torque. Anchor bolts are used to hold the stator down in practically all motor installations.

Figure 2 shows that the stator counter-torque can be used to double the shaft torque at a given rotor speed by removing the mounting bolts, allowing the stator to rotate on the added bearings, and transferring the stator torque to the shaft through gears, such as a set of planetary gears. Figure 2 also

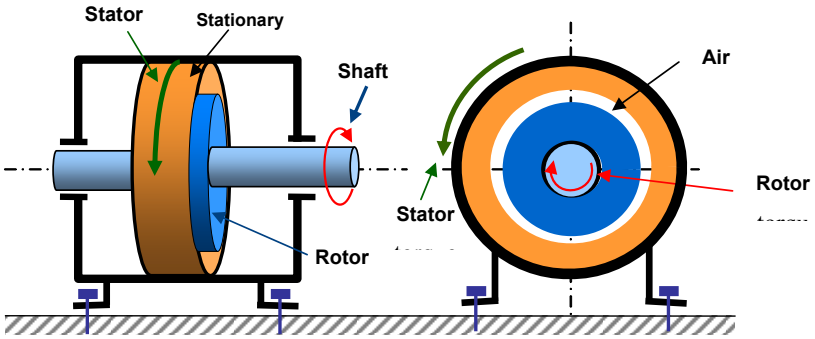

Figure 1. Shaft torque and stator torque of a motor.

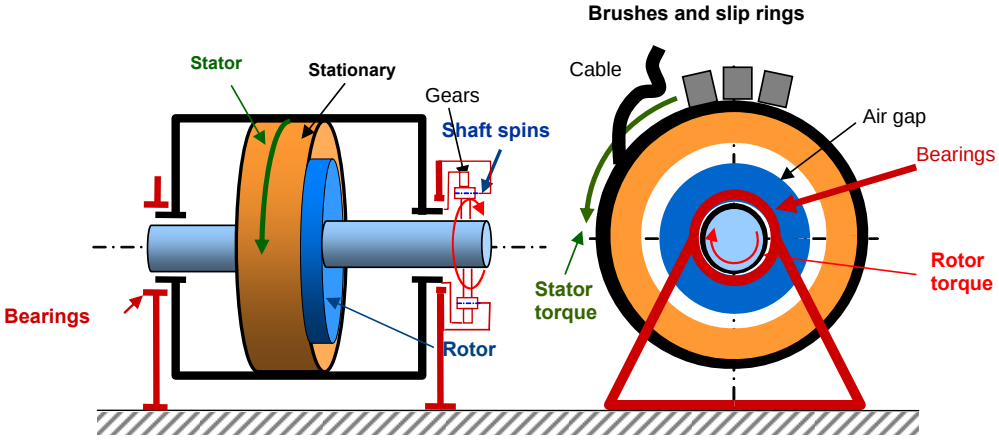

Figure 2. Doubling shaft torque at a given shaft speed.

shows that to harvest the torque of a rotating stator (or armature), brushes and slip rings would normally be required. Oak Ridge National Laboratory's (ORNL's) uncluttered CVT is a novel approach that doubles the torque at a given rotor speed and eliminates the brushes and slip rings. The absence of brushes and slip rings in the ORNL technology is emphasized in Figure 3.

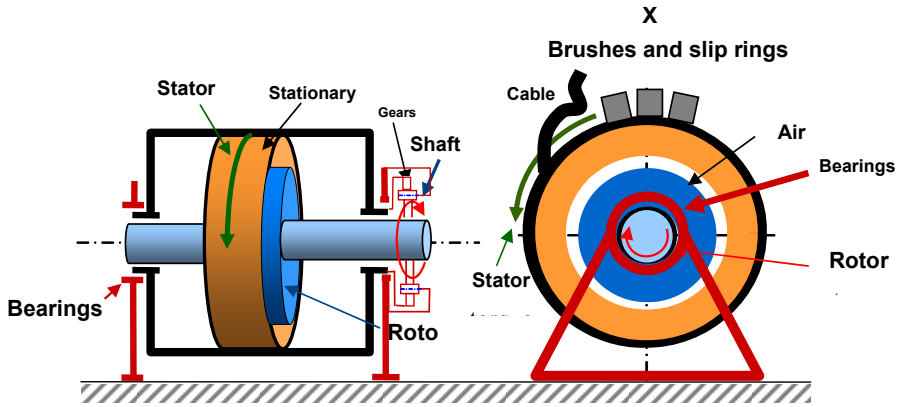

Figure 3. ORNL technology does not have brushes and slip rings.

Uncluttered Rotor

The ORNL technology for eliminating the brushes and slip rings is derived from the uncluttered rotor concept, which is explained through a conventional wound-stator core. When 3-phase currents are fed to the windings of a conventional wound-stator core, a rotating magnetic flux is produced, which goes through the air gap and reaches the rotor to return the rotating flux. The rotating speed of this rotating flux observed from the stator, regardless of whether the stator is stationary or rotating, is determined only by the frequency and number of poles of the winding. Therefore, the function of an uncluttered rotor is to produce a rotating flux. The rotating speed of this flux observed from the uncluttered rotor is determined only by the excitation frequency and by the number of poles of the uncluttered rotor. There are no brushes and slip rings for the excitation of the uncluttered rotor. The excitation wound core for the uncluttered rotor is stationary. The uncluttered rotor has no conductor; hence, no brushes and slip rings are required. The term "uncluttered" arises from the fact that when the current frequency is fed to the stationary excitation coil, the rotor speed does not change the corresponding rotating flux speed viewed from the rotor. The rotor speed influence is totally isolated to prevent a cluttered outcome.

Many variations of the uncluttered rotor and its excitation can be achieved. For example, Figure 4 shows an 18-pole, axial-gap, 2-phase uncluttered rotor that has two sides. The side facing the uncluttered rotor excitation core has rings. The flux has a tangential coupling between the excitation core and the rings. Because the rotation of the rings does not cause a change in the flux entering or leaving the rings, no torque is produced for this tangential magnetic coupling.

The opposite side of the sample axial-gap rotor has conventional teeth. When this side is coupled to a permanent magnet rotor with poles or to a conventional stator with teeth, the radial coupling produces torque. Figure 5 shows the ring side of the actual prototype uncluttered rotor. The opposite side of the rotor with teeth is shown in Figure 6.

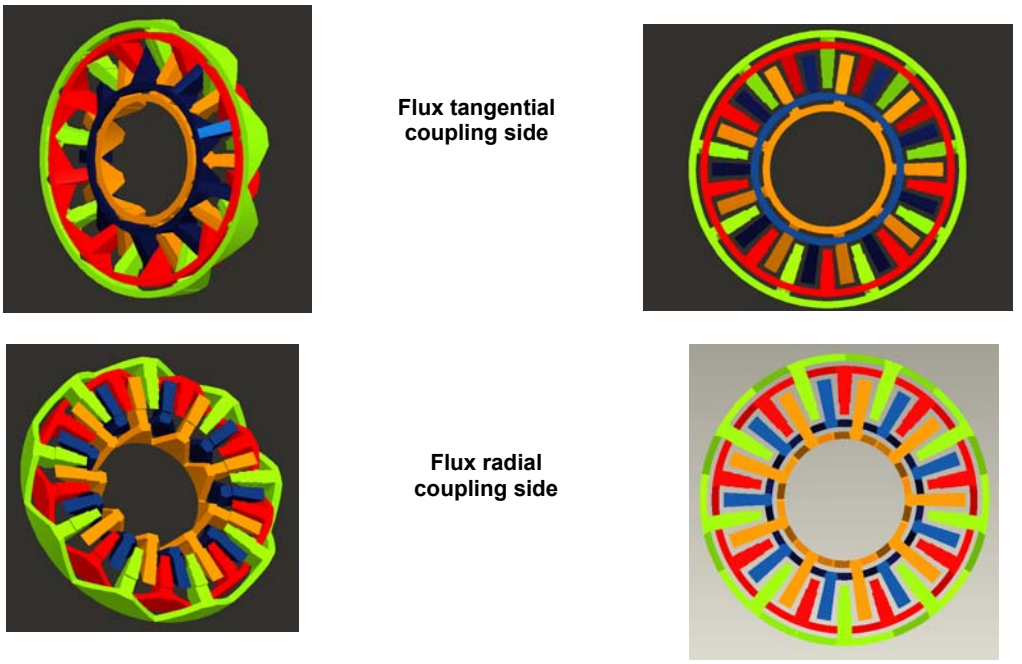

Figure 4. Example of an 18-pole, axial-gap, 2-phase uncluttered rotor.

Figure 5. One side of the proof-of-concept uncluttered rotor with rings.

Figure 6. The opposite side of the proof-of -concept uncluttered rotor with teeth.

The excitation core for the uncluttered rotor is shown in Figure 7. The two circular slots are for the 2-phase excitation coils. The resistance values and the inductance values of these 2-phase coils are designed to be equal for balanced 2-phase operation. The resistance value can be controlled by the wire size and the inductance value by the ring and slot dimensions. For the 3-phase option, three rings would be required, instead of the four rings required for the 2-phase option. In short, the uncluttered rotor made of flux-conducting material produces an equivalent rotating armature without brushes and slip rings.

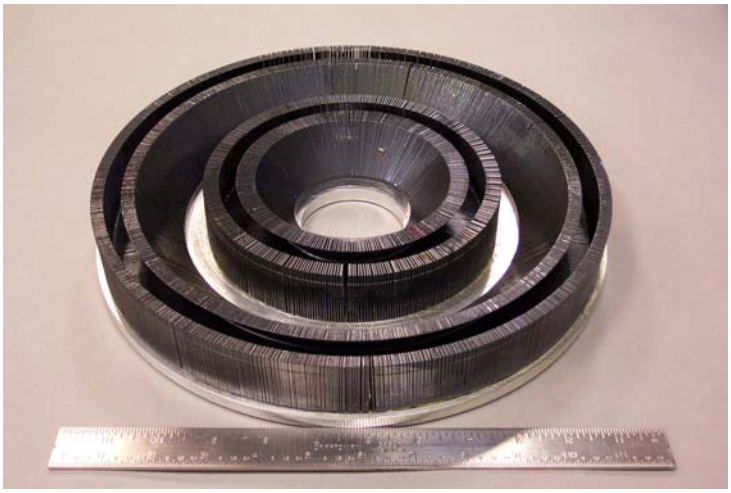

Figure 7. Two-phase excitation core for the uncluttered rotor.

Uncluttered CVT

An uncluttered CVT offers these benefits:

- Rotating stator for harvesting the reaction torque
- Brushless operation
- Combination motor and generator
- Single set of permanent magnets
- Smaller size, lighter weight, and lower cost

Figure 8 shows an example of the uncluttered rotor concept used for a CVT. The portion marked "Completed in FY 06" was to prove the brushless rotating armature concept. Inside this portion, the uncluttered rotor is sandwiched between the uncluttered rotor excitation core on the left and an air gap facing the rotating field of the permanent magnet rotor on the right. The combination of the excitation core and the uncluttered rotor is equivalent to a rotating stator without brushes. The energy going into the stationary excitation core is transferred through the air gap to the uncluttered rotor. Because the magnetic coupling at this air gap is a tangential coupling, no torque is produced during the transfer. The other side of the uncluttered rotor has a radial coupling between the uncluttered rotor and the permanent magnet rotor. Torque would be produced between the uncluttered rotor and the permanent magnet rotor in this air gap.

For the initial concept validation, the permanent magnet rotor was taken out and the wound stator used on the right side was substituted to produce a rotating field.

A possible axial-gap example of an uncluttered CVT is shown in Figure 9. For FY 2006, the experimental setup for using the uncluttered rotor concept to prove the brushless rotating armature concept is shown in Figure 10.

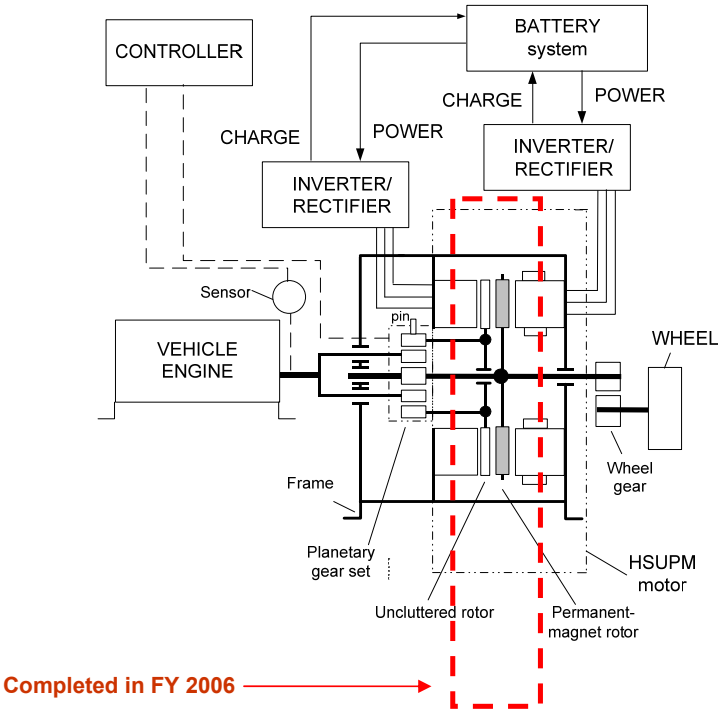

Figure 8. An example of an uncluttered CVT.

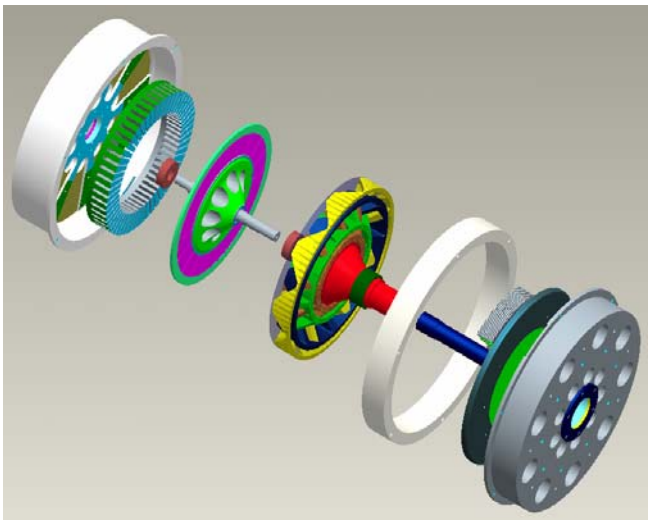

Figure 9. A possible axial-gap example of an uncluttered CVT.

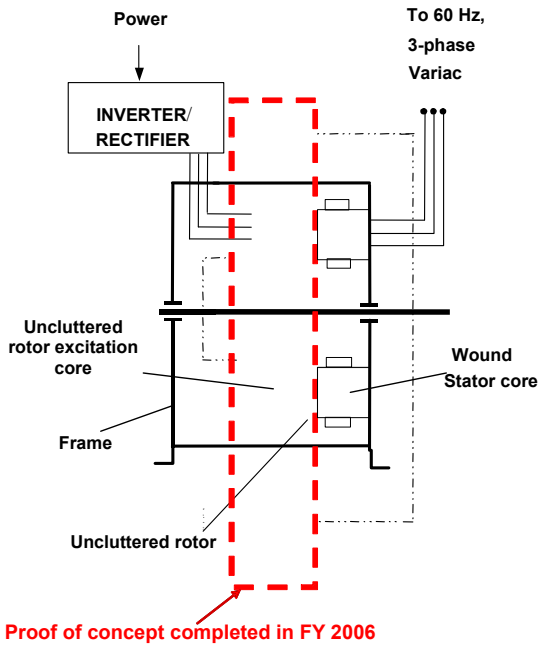

Figure 10. Experimental setup for proving the brushless rotating armature concept.

Figure 11 shows the prototype for the uncluttered rotor proof of concept completed in FY 2006. There are no brushes or slip rings in the machine. The 3-phase wound stator leads are connected to one side of the conventional axial-gap stator that provides a rotating field for the emulation of the rotating permanent magnet rotor. The uncluttered rotor shaft and the uncluttered rotor brushless excitation leads are also shown. The cut view of the proof-of-concept uncluttered rotor prototype is shown in Figure 12.

Tests on the Uncluttered Rotor

The following tests were performed on the prototype.

Induction Mode Test

In this test, the uncluttered rotor and its stator were viewed as a rotating stator or as a rotating wound armature. This rotating wound armature was magnetically coupled to another rotating field produced by the permanent magnet. In this test, the rotating field produced by the permanent magnets was replaced by the rotating field produced by a 3-phase wound core. If the frequency going into the 3-phase wound core is changed, the synchronous speed of the rotating field will be equivalent to the speed of the permanent magnet rotor. Therefore, the rotating wound armature coupled to the rotating field at a synchronous speed will actually be equivalent to an induction motor. In this equivalent setup, the rotating armature will act like a rotor of an induction motor, and the permanent magnet rotor will act like a stator of an induction motor that produces a synchronous magnetic field. The speed of the uncluttered rotor acting as the rotor of an induction motor would have a slip that is lower than the synchronous speed. The speed could be controlled by varying the resistance of the stationary uncluttered- rotor excitation coils. This expectation was clearly confirmed by the test.

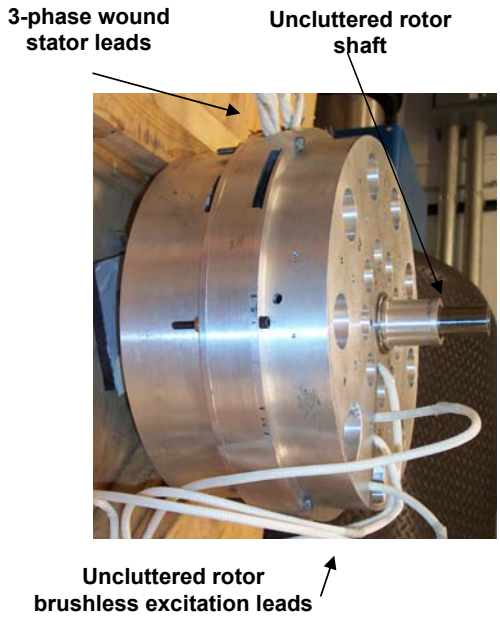

Figure 11. The prototype for the uncluttered rotor proof of concept completed in FY 2006.

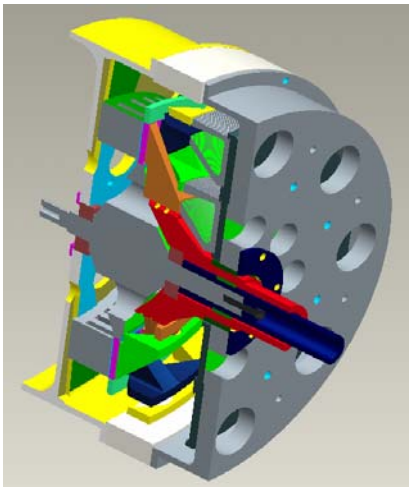

Figure 12. Cut view of the uncluttered rotor proof-of-concept prototype.

dc Mode Test

In this test, a dc current was fed to the stationary uncluttered-rotor excitation coils. The dc flux produced by the dc current went through the flux rings of the uncluttered rotor and turned into 8-pole flux on the other side of the rotor. This 8-pole flux interacted with the rotating flux produced by the 3-phase wound core that resulted in a synchronous motor. The rotor speed should be the synchronous speed of 400 rpm. This expectation was confirmed by the test.

Variable Frequency Mode Test

In this test, a set of variable-frequency two-phase currents was fed to the stationary uncluttered-rotor excitation coils. The variable-frequency flux produced by the variable-frequency currents went through the flux rings of the uncluttered rotor and transformed into an 8-pole rotating flux on the other side of the rotor. The speed of the uncluttered rotor went higher than the synchronous speed of the 3-phase wound core when the 2-phase sequence was opposite to the 3-phase sequence. If the 2-phase sequence is the same as the 3-phase sequence, the speed of the uncluttered rotor would go lower than the synchronous speed of the 3-phase wound core. This expectation was confirmed by the test.
Note that the number of phases of the uncluttered rotor excitation coils can be changed to two, three, or other practical numbers.

Conclusion

The concept of using an uncluttered rotor for the rotating brushless stator armature was proved through induction mode, dc mode, and variable-frequency mode tests. In FY 2006, a prototype was built and the concept for the rotating brushless stator armature was validated.

Future Direction

The next step is to simulate the performance of the uncluttered rotor and subsequently the uncluttered CVT assembly through design iteration and to start work on control of the uncluttered rotor.

Patents

John Hsu, "Hybrid-Secondary Uncluttered Permanent Magnet Machine and Method," U.S. Patent 6,977,454, December 20, 2005.

John Hsu, "Simplified Hybrid-Secondary Uncluttered Machine and Method," U.S. Patent 6,891,301, May 10, 2005.

John Hsu, "Hybrid Secondary Uncluttered Induction Machine," U.S. Patent No. 6,310,417, October 30, 2001.

References

1. J. Hsu, "Hybrid-Secondary Uncluttered Induction (HSUI) Machine," *IEEE Transactions on Energy Conversion* **16**(2), ITCNE4, (ISSN 0885-8969), 192–197 (June 2001).
2. J. Perahia, "Discussion of Hybrid-Secondary-Uncluttered Induction (HSUI) Machine," *IEEE Transactions on Energy Conversion* **17**(1), ITCNE4, (ISSN 0885-8969), 150 (March 2002).
3. J. Hsu, "Closure on Hybrid-Secondary-Uncluttered Induction (HSUI) Machine," *IEEE Transactions on Energy Conversion* **17**(1), ITCNE4, (ISSN 0885-8969), 150 (March 2002).

3.2 Interior Permanent Magnet Reluctance Machines

3.2.1 Interior Permanent Magnet Reluctance Machines with Brushless Field Excitation—16,000 rpm

Principal Investigator: John Hsu
Oak Ridge National Laboratory
National Transportation Research Center
2360 Cherahala Boulevard
Knoxville, TN 37932
Voice: 865-946-1325; Fax: 865-946-1210; E-mail: hsujs @ornl.gov

DOE Technology Development Manager: Susan A. Rogers
Voice: 202-586-8997; Fax: 202-586-1600; E-mail: Susan.Rogers@ee.doe.gov

ORNL Program Manager: Mitch Olszewski
Voice: 865-946-1350; Fax: 865-946-1262; E-mail: olszewskim@ornl.gov

---

Objective

Develop an interior permanent magnet (IPM) reluctance motor with brushless field excitation that offers high torque per ampere per core length by using a brushless excitation coil to enhance the flux. The motor does not require a dc/dc boost converter at medium and high speeds. The core loss is low, because the flux can be weakened by not supplying current to the excitation coil.

Approach

Increase motor speed to reduce size, weight, and cost.

- Achieve field weakening and enhancement by incorporating an additional flux path using external field excitation.
- Improve existing IPM design by adding side magnets without additional brushless field excitation.

Positives

1. The system does not require a dc/dc boost converter, resulting in a reduction in system costs.
2. Sufficiently higher torque per ampere per core length can be attained at low speeds.
3. Lower core losses at low torque regions, especially at high speeds, are attained.
4. Safety and reliability are increased because burning is prevented under the fault condition of a shorted winding.

Negatives

The system has an unconventional rotor structure and unconventional brushless field excitation.

Barriers/Challenges

For 16,000-rpm motors, mechanical stress is a challenge. Thicker bridges that link the rotor punching segments have to be increased. Consequently, the rotor flux leakages significantly lower the motor performance. This barrier can be overcome by the use of external excitation to ensure sufficient rotor flux.

Tasks

- Perform electromagnetic simulations and mechanical analysis.
- Complete fabrication of motor.

- Conduct evaluation tests upon completion of motor assembly.
- Complete testing in FY 2007.

Accomplishments

The assembly of the ORNL 16,000-rpm motor design is shown in Figure 1. Table 1 compares the dimensions of the ORNL 16,000-rpm motor and those of the Toyota/Prius motor.[1,2] The masses and sizes derived from this table provide a basis for a cost comparison with the Prius motor. The extra excitation coils and cores of the ORNL motor are made of copper wires and mild steel. The savings realized by a shorter stator core (1.875 in. compared with 3.3 in. for the Prius) and shorter stator winding compensate for their total cost. The low-current (5 A, maximum) control of the field excitation cost is minimal because of the low-current components required. This motor design enables better motor performance with system cost savings. Additionally, if used in a vehicle architecture requiring a boost converter, this motor can produce 250-kW output at 16,000 rpm. This significantly widens the possible applications for this type of motor.

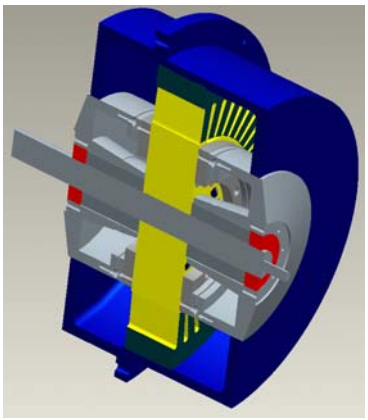

Figure 1. Assembly of ORNL 16,000-rpm motor design.

Table 1. Comparison of dimensions of the ORNL 16,000-rpm motor and the Toyota/Prius motor

	Prius	ORNL
Speed_	6000 rpm	16,000 rpm
Stator Lam. OD_	10.6”	same
Rotor OD_	6.375”	same
Core length_	3.3”	1.88”
Bearing to Bearing outer face_	7.75”	7.45”
Magnet Weight lbs_	2.75	2.57
Estimated field adj. ratio_	none	2.5
Rating_	33/50 kW	same
Boost converter_	yes	No
High speed core loss_	high	low

Technical Discussion

The design for the 16,000-rpm motor not only optimizes torque capability but also incorporates the ability to weaken the air gap flux density by having no excitation coil current. The need for low core losses across a wide range of speeds was also addressed in this design. The design maximizes the thickness of

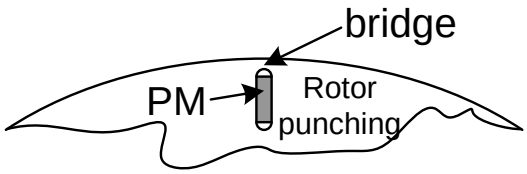

Figure 2. Location of bridge in a rotor punching.

the rotor punching bridges (material between the magnet slots in the rotor) (Figure 2) to satisfy the mechanical stress requirements at the high speeds required of this machine. More leakage flux produced by the PMs can go through these bridges, so the air-gap flux density produced by the PMs will be lower than in other, similar IPM machines such as the lower-speed Prius motor.

The 16,000-rpm motor with brushless field excitation provides flexibility for a drive system design to meet field strength requirements that vary at different loads and speeds. In general, the brushless field excitation approach can provide field enhancement and weakening for strong or weak PMs, as shown in Figure 3.

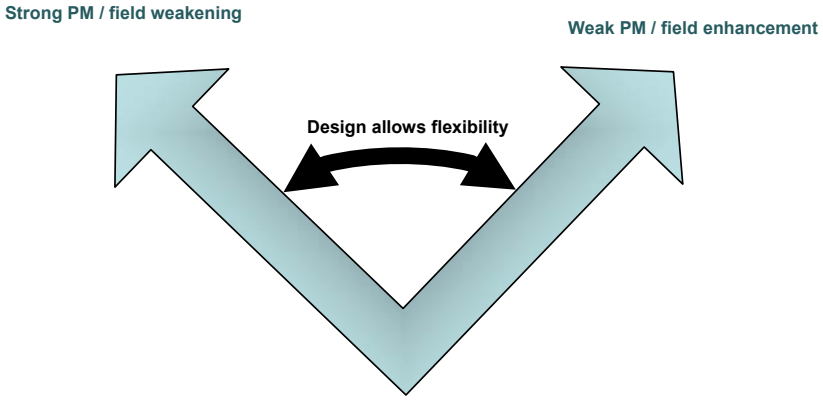

Figure 3. Flexibility provided by adjustable field excitation.

This motor is intentionally designed for low air-gap flux density at high speeds with no field excitation current applied This solves the problem of high core loss seen in existing high-PM-flux-density, high-speed motors of the type used in Prius and Highlander automobiles, which are plagued with both high core and high d-axis current losses necessary for field weakening. Figure 4 shows the rotor punching, the locations of PMs, and the completed rotor.

Figure 5 shows the air-gap flux density distributions at various excitation ampereturns (ATs). The excitation coil has 865 turns. The excitation current is the ATs, divided by the turns (865). The air-gap flux density of this motor can be adjusted with the external excitation coils to tailor the torque output. When high torque is required, the air-gap flux density is enhanced. When low torque and high efficiency are required, the excitation current is reduced to zero.

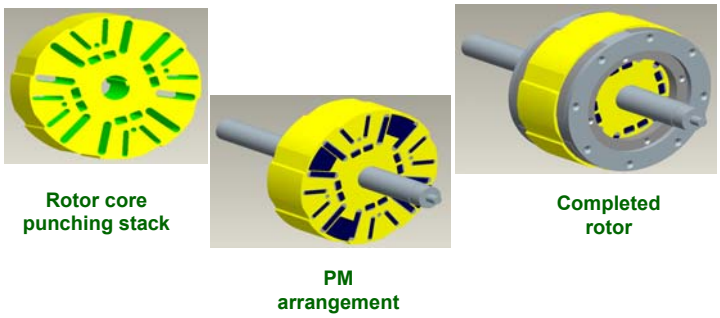

Figure 4. Rotor of ORNL's 16,000-rpm motor.

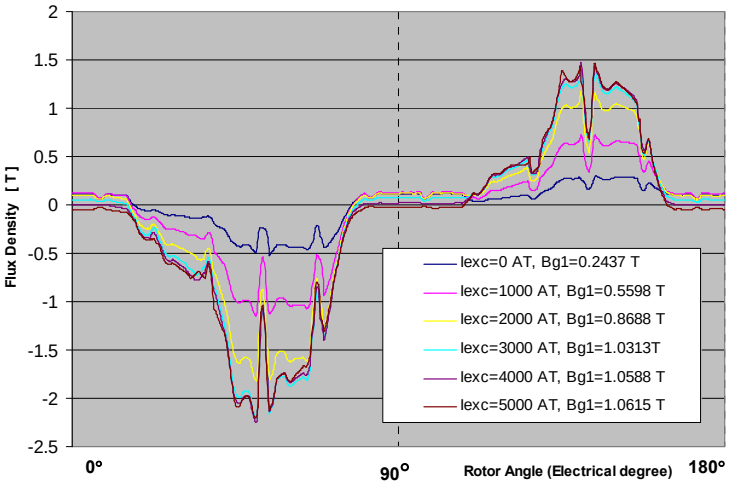

Figure 5. Air-gap flux density distributions with various excitation ampereturns (AT).

Figure 6 shows test results for three-phase, line-to-neutral back-electromotive force (emf) at 5000 rpm with 5-A and 0-A excitation currents, respectively. The asymmetry of the air-gap flux density distribution shown in Figure 5 does not affect the symmetry of the induced back-emf waveform. The expected output torque at 141 A_{RMS} (i.e., 200-A magnitude value) is shown in Figure 7. It clearly shows that the stronger field excitation can enhance the output torque.

The vibration analysis obtained from testing is shown in Figure 8. Vibration analysis will be conducted at each subsequent speed tested.

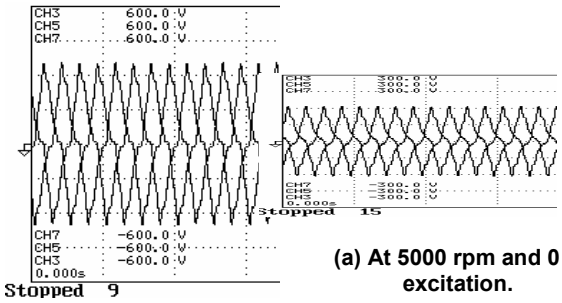

(a) At 5000 rpm and 0 A excitation.

(b) At 5000 rpm and +5 A excitation.

Figure 6. Three-phase line-to-neutral back-emfs at 5000 rpm with and without field excitation.

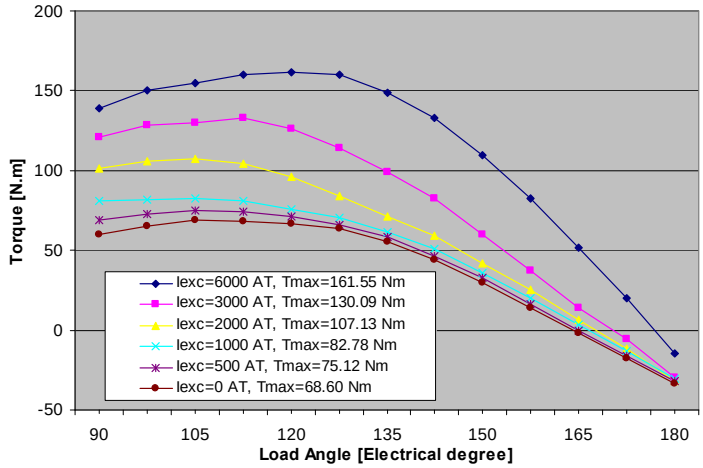

Figure 7. Stronger field excitation that can enhance output torque.

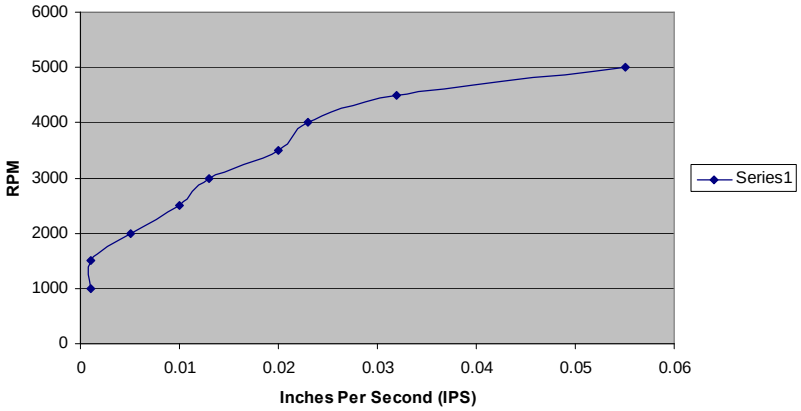

Figure 8. Vibration analysis obtained from test.

Figure 9 shows that the back-emf can be controlled effectively through the external field excitation current with a range of current from 0 to 5 A, thus negating the necessity of using a boost converter to overcome high back-emf. The initial tests show that the air-gap flux density can change up to 2.5 times at a given speed. This enables the motor to have all the advantages of both the existing strong PM reluctance motors (i.e., high power density, high back-emf at high speed, high core loss) and the weak PM reluctance motors (i.e., low power density, low back-emf, lower core loss) without their disadvantages. The additional circuitry necessary to supply the excitation current to the coils should cost less than $10 in production quantities.

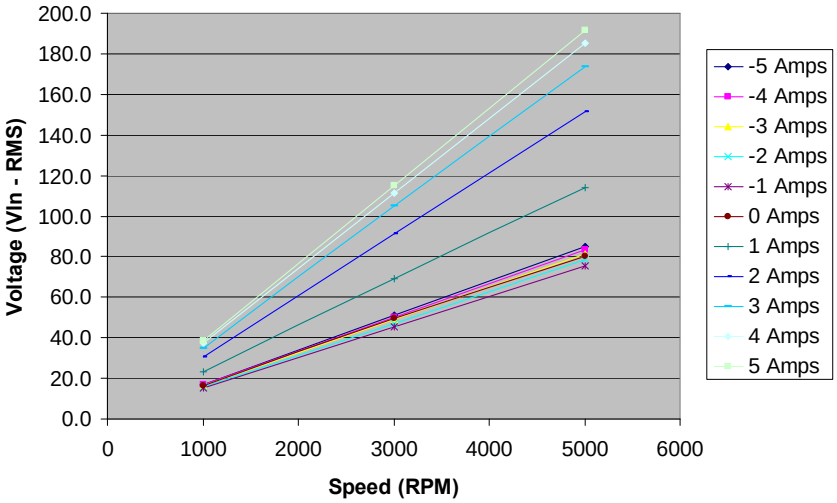

Figure 9. Line-to-neutral back-emf voltage vs speed.

The core and friction loss tests conducted show the benefits of lower air-gap flux density (Figure 10). For example, at 5000 rpm, the core and friction loss is 200 W with zero field excitation, compared with 600 W at high field excitation for a high air-gap flux density. This inherently low air-gap flux density motor design enables significantly lower core losses at high speeds (Figure 11). Yet at low speeds, when high torque is needed, the ability to enhance the field can dramatically boost the torque. The excitation coils coupled with this low air-gap flux design enable the motor to be controlled or "fine tuned" to operate in its highest-efficiency areas across the torque/speed curve.

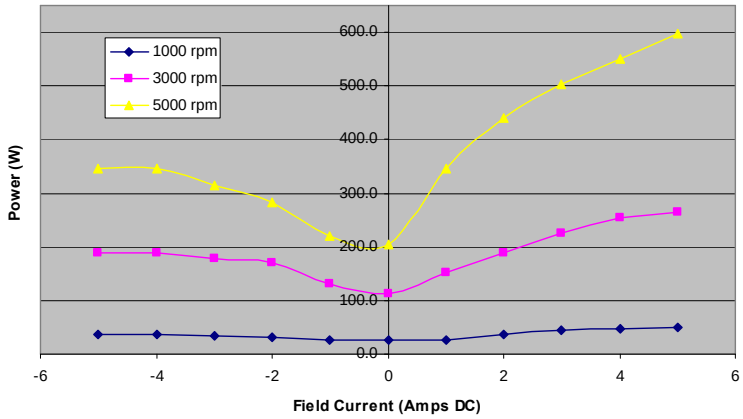

Figure 10. No-load core and friction losses vs field current for each speed.

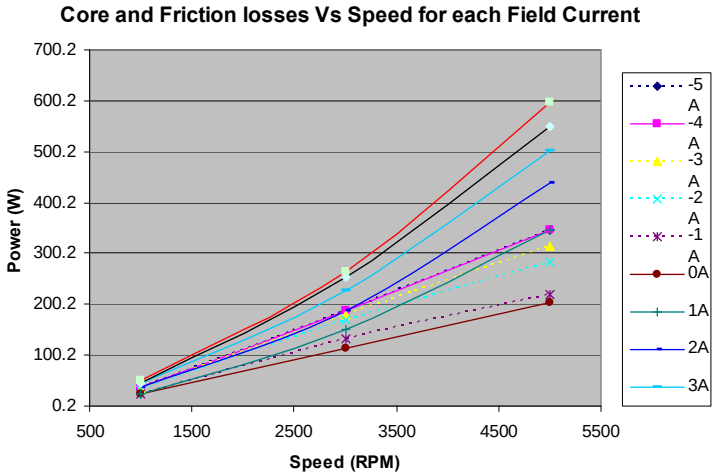

Figure 11. No-load core and friction losses vs speed for each field current.

Mechanical Analyses of 16,000-rpm Rotor

Extensive effort was expended on the high-speed, 16,000-rpm critical speed and three-dimensional (3-D) mechanical stress analyses. A transfer matrix approach was used to estimate the critical speed. The 3-D softwares used for stress analyses were ALGOR, ANSYS, and Pro/E. The analytical results are as follows.

- Estimated critical speed of 16,000-rpm rotors: 24,960 rpm (safety factor = 1.56).
- Stress analyses of rotor:
  - — Figure 12(a) shows the solid models with only a quarter of the PMs having properly defined contact surfaces (i.e., the upper right quarter that shows the gaps between PM and rotor punching).
  - — Figure 12(b) shows that when contact surfaces are bonded to the lamination, the stresses become unrealistically low. This demonstrates the importance of having the contact surfaces properly defined.

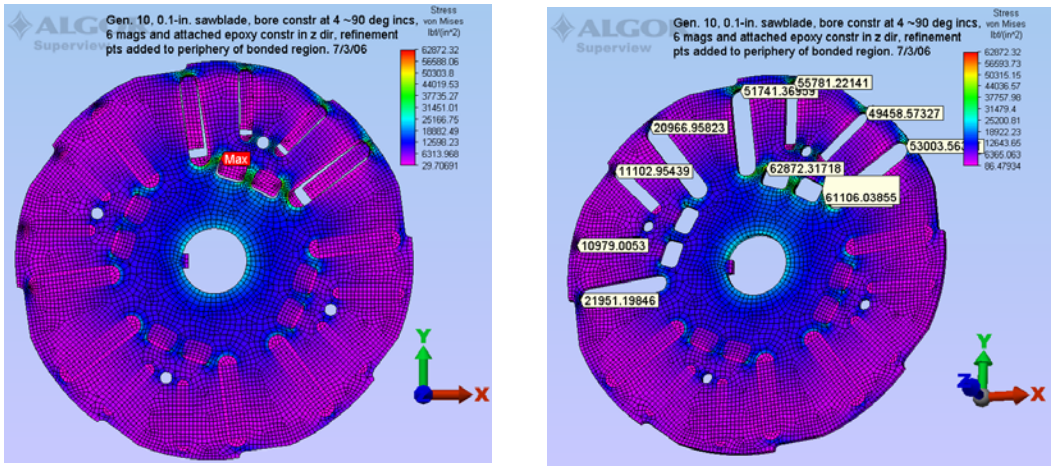

Figure 12. Finite-element stress analysis of 16,000-rpm rotor.

Figure 13 shows that, from the simulation, the radial displacement at the rim of a 0.018-in.-thick 16,000-rpm laminate rotor ranges from 0.00066 to 0.00124 in., which is less than the air gap of 0.029 in. Figure 14 shows that, although acceptable, the shear stresses at the support columns of a 0.018-in.-thick 16,000-rpm laminate rotor are slightly larger because the side of the small magnet nearest to the radial magnet is not along a radius.

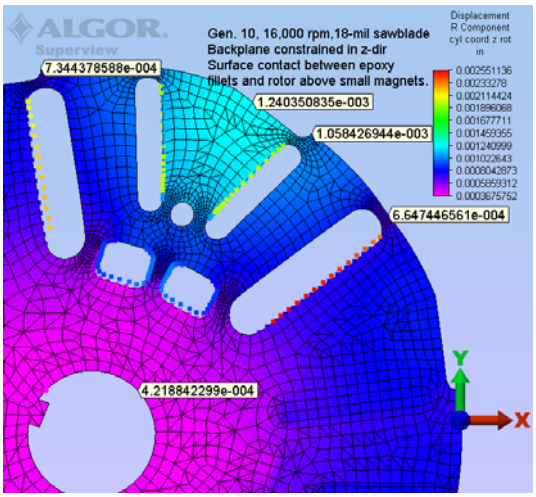

Figure 13. Radial displacement analysis of 16,000-rpm rotor.

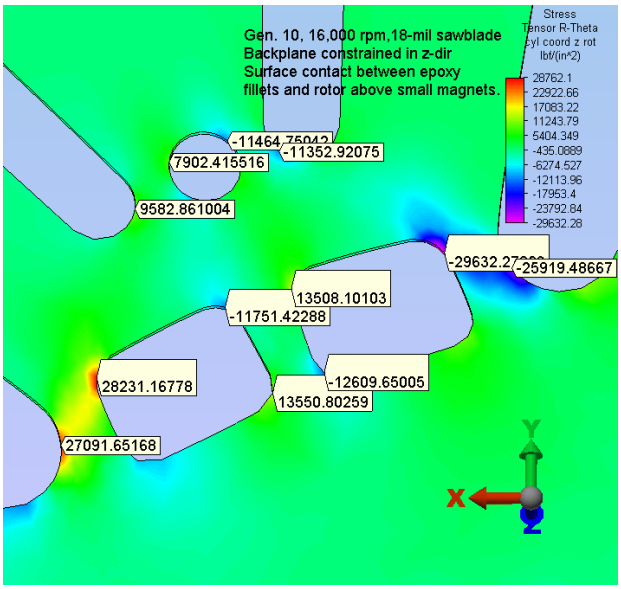

Figure 14. Shear stresses at the support columns of an 0.018-in. thick 16,000-rpm laminate rotor.

Parts fabricated

Figures 15 through 20 show the parts that have been fabricated for the prototype motor.

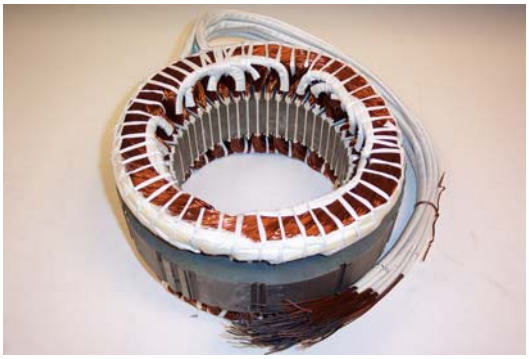

Figure 15. Wound stator core.

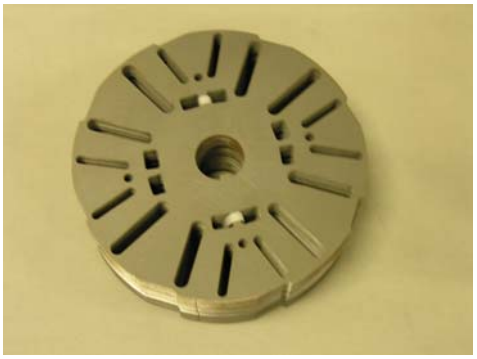

Figure 16. Rotor punching.

Figure 17. Rotor core stack and shaft.

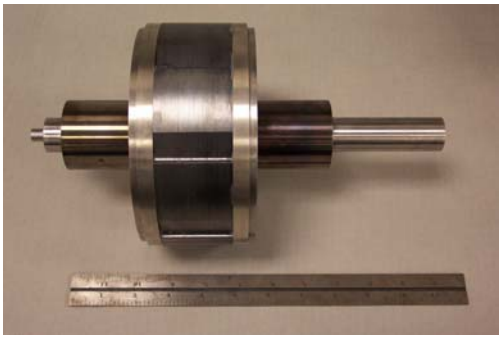

Figure 18. Completed rotor.

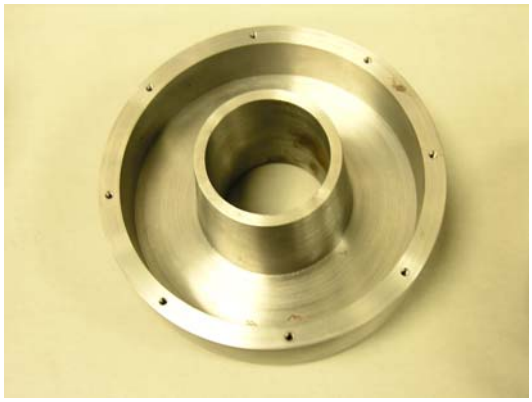

Figure 19. Excitation coil housing.

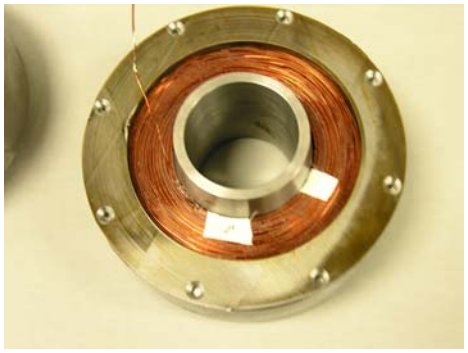

Figure 20. Excitation coil inside the coil housing.

Based on the experience of building the prototype at ORNL, it is anticipated that the motor will not present any complicated manufacturing issues. This is certainly a concern with any design undertaken at ORNL. No issues with added gearbox complexity are expected. We do not foresee a more complex gearbox than the planetary gearbox that is currently used by some automotive manufacturers.

The prototype motor can be further reduced in mass and volume by redesigning the interface between the excitation coils and the motor housing. This improvement will reduce the cost to manufacture the motor by eliminating some machining steps as well as raw materials.

Conclusion

The design of the 16,000-rpm motor not only optimizes torque capability but also incorporates the ability to weaken the air-gap flux density. It also addresses the need for low core losses across a wide range of speeds.

This design maximizes the thickness of the rotor punching bridges (material between the magnet slots in the rotor) to satisfy the mechanical stress requirements at the high speeds required of this machine. More leakage flux produced by the PMs can go through these bridges, so the air-gap flux density produced by the PMs will be lower than in other, similar IPM machines such as the lower-speed Prius motor.

Our motor is intentionally designed for low air-gap flux density at high speeds with no field excitation current applied. This solves the problem of high core losses seen in existing high-PM-flux-density, high-speed motors of the type used in the Prius and Highlander automobiles, which are plagued with both high core and high d-axis current losses necessary for field weakening.

This motor is still in the development stage. Validation data will be available after initial testing is completed this year. Initial test results show the following:

- The back-emf can be controlled effectively through the external field excitation current with a range of current from 0 to 5 A, thus negating the necessity of using a boost converter to overcome high back-emf. The air-gap flux density can change up to 2.5 times at a given speed. This enables the motor to have all the advantages of both existing strong PM reluctance motors (i.e., high power density, high back-emf at high speed, high core loss) and weak PM reluctance motors (i.e., low power density, low back-emf, lower core loss) without their disadvantages. The additional circuitry necessary to supply the excitation current to the coils should cost less than $10 in production quantities.
- The core and friction loss tests conducted show the benefits of lower air-gap flux density. For example, at 5000 rpm, the core and friction loss is 200 W with zero field excitation, compared with 600 W at high field excitation for a high air-gap flux density.

This inherently low air-gap flux density motor design enables significantly lower core losses at high speeds. Yet at low speeds, when high torque is needed, the ability to enhance the field can dramatically boost the torque. The excitation coils, coupled with this low air-gap flux design, enable the motor to be controlled or fine tuned to operate in its highest-efficiency areas across the torque/speed curve.

It is not anticipated that the motor will present any complicated manufacturing issues. Redesigning the interface between the excitation coils and the motor housing will further reduce the mass and volume of the prototype motor, reducing the manufacturing cost.

In addition to the low loss performance improvement, this motor design eliminates the requirement for a boost converter, simplifying the power electronics and enabling cost savings in the total drive system. Comparing mass and size provides a basis for a cost comparison with the Prius motor. The extra excitation coils and cores of the 16,000-rpm motor are made of copper wires and mild steel. The savings realized by a shorter stator core (1.875 in. compared with the 3.3 in. of Prius) and shorter stator winding compensate for their total cost. The low-current (5-A, maximum) control circuit for the field excitation coils cost is minimal because of the low-current components required. This motor design enables better performance with system cost savings. Additionally, if used in a vehicle architecture requiring a boost

converter, this motor can produce 250-kW output at 16,000 rpm, significantly widening possible applications.

Future Direction

In FY 2007 the research goal is to produce a motor with significantly reduced size, weight, and volume from that of current technology. The higher power density and lower system cost will provide industry with a greater cost vs performance ratio. A dramatic system cost savings will be realized by eliminating the dc/dc boost converter as well. Through reductions in core losses at high speeds by using the field weakening capability improvements in vehicle fuel efficiency will also be realized.

In FY 2007 performance testing will be completed. Performance calculations for the 3-D RIPM-BFE motors will be verified and adjustments made in the models depending on testing results. These tests will include the back-emf data with no field excitation as well as with enhancement and weakening of the field. Locked rotor testing will be completed with the same conditions as the back-emf tests (no field excitation and enhancement/weakening of the field). Performance and efficiency mapping will also be completed during FY 2007. Testing will take place at various voltage increments, and speed and torque ranges, similar to the benchmarking tests performed on the Prius motor at ORNL. This motor will be driven by a dynamometer system to facilitate data measurements. Revisions to the motor, due to unforeseen issues, will be resolved, and the motor will be retested as necessary.

Patents

J. S. Hsu et al., "Rotor Apparatus for High Strength Undiffused Brushless Electric Machine," U.S. Patent 6,989,619, January 24, 2006.

J. S. Hsu et al., "Hybrid-Secondary Uncluttered Permanent Magnet Machine and Method," U.S. Patent 6,977,454, December 20, 2005.

J. S. Hsu et al., "Permanent Magnet Machine and Method with Reluctance Poles for High Strength Undiffused Brushless Operation," U.S. Patent 6,972,504, December 6, 2005.

J. S. Hsu et al., "Simplified Hybrid-Secondary Uncluttered Machine and Method," U.S. Patent 6,891,301, May 10, 2005.

J. S. Hsu et al., "High Strength Undiffused Brushless (HSUB) Machine," U.S. Patent 6,573,634, June 3, 2003.

J. S. Hsu et al., "Hybrid Secondary Uncluttered Induction Machine," U.S. Patent 6,310,417, October 30, 2001.

J. S. Hsu et al., "Permanent Magnet Energy Conversion Machine," U.S. Patent 5,952,756, September 14, 1999.

References

1. M. Kamiya, "Development of Traction Drive Motors for the Toyota Hybrid System," Toyota Motor Corporation, 1, Toyota-cho, Toyota, Aichi, Japan.
2. M. Okamura, E. Sato, and S. Sasaki, "Development of Hybrid Electric Drive System Using a Boost Converter," Toyota Motor Corporation, 1, Toyota-cho, Toyota, Aichi, Japan.

3.2.2 High-Power-Density Reluctance Interior Permanent Magnet Machines—6,000 rpm

Principal Investigator: John Hsu
Oak Ridge National Laboratory
National Transportation Research Center
2360 Cherahala Boulevard
Knoxville, TN 37932
Voice: 865-946-1325; Fax: 865-946-1210; E-mail: hsujs@ornl.gov

DOE Technology Development Manager: Susan A. Rogers
Voice: 202-586-8997; Fax: 202-586-1600; E-mail: Susan.Rogers@ee.doe.gov

ORNL Program Manager: Mitch Olszewski
Voice: 865-946-1350; Fax: 865-946-1262; E-mail: olszewskim@ornl.gov

---

Objective

- The objective is development of a high-power-density motor technology for reluctance interior permanent magnet (RIPM) motors, using side magnets located at the motor's end turns.

Approach

- To improve the power density of existing RIPM motors, the rotor of this new design was modified to have additional side magnets. Because this new motor does not use any additional external field excitation, it is more in line with conventional motor structures than other recent Oak Ridge National Laboratory (ORNL) motor projects. This project involved the development of a 6000-rpm motor. However, the new technology resulting from this project can be used for either higher- or lower-speed motors. A dc/dc boost converter and/or a strong direct-axis current for field weakening might be needed for this motor at high speeds because of the high back–electromotive force (emf) produced by the strong permanent magnet (PM) air-gap flux density.
- The unique design of this motor necessitated highly intensive, time-consuming computational modeling. Traditional two-dimensional finite element analyses could not be used effectively in the simulations, so three-dimensional simulations had to be performed.

Major Accomplishments

- The new technology derived from this project shows that the air-gap flux density produced by the new PM arrangement can be doubled compared with that of the Toyota Prius motor. The PM torque component is proportional to the product of the PM fundamental air-gap flux density and the current of the motor. Therefore, higher PM fundamental air-gap flux density produces higher toque at a given current and hence a higher power density of the motor.

Future Direction

This project was completed in FY 2006.

Technical Discussion

The power input of an RIPM motor is shown in Equation (1). The output power of the motor is the input power minus the losses of the motor. If the losses that include the copper loss, core loss, stray loss, and mechanical loss of the motor are neglected for simplification, the output power is represented by the input power.

$$P_{in} = \frac{3}{2}\left[\frac{EV}{X_d}\sin\delta - \frac{V^2}{2}\left(\frac{1}{X_q} - \frac{1}{X_d}\right)\sin 2\delta\right] \quad (1)$$

In Equation (1), E is the back-emf that is proportional to the no-load air-gap flux density. V is the phase voltage, δ is the load angle, and X_d and X_q are the direct and quadrature inductances, respectively. Based on this equation, power can be increased by raising the E value.

Because E is produced by the PMs without excitation from the stator currents, the higher the air-gap flux density is at no load, the higher the E value is. The target for this investigation is to find practical ways to increase the air-gap flux density produced by the PMs. Various novel PM arrangements are compared with the arrangement of the Toyota Prius PM rotor, which is shown in Figure 1. The PMs are situated inside the V-shaped grooves [1–2]. There is an air gap between the rotor and the stator. The air-gap flux density of this motor is used as the base value for the normalized comparison for various novel PM arrangements.

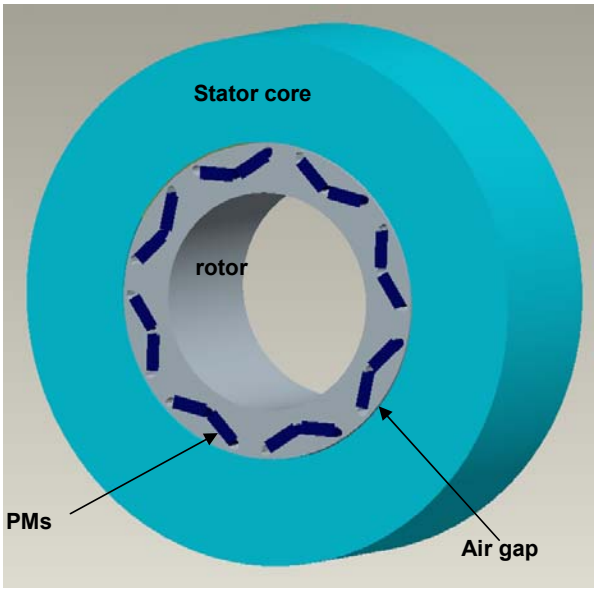

Figure 1. PM arrangement of Toyota Prius rotor.

Figure 2 shows various PM arrangements of an RIPM motor that has no additional field excitation. Figure 2(a) shows the U-shaped PMs that are symmetrically arranged for the north and south poles of the rotor. There is no side PM for this arrangement. Figure 2(b) shows that in addition to the U-shaped PMs, there can be either partial side PMs (represented by the blue magnets) or full side PMs (represented by both the blue and brown magnets). For the partial side-PM arrangement, the side PM and side pole piece are alternately located at the ends of the rotor poles. For the full side-PM arrangement, PMs are located at the ends of the rotor poles. A soft magnetic end ring (not shown) is attached to the ends of the side PMs to provide a flux return path for the side PMs.

Figure 3 shows the locations of the side poles and side PMs of a partial side-PM prototype motor. The magnetic end rings are not shown in this figure. For a full side-PMs arrangement, the side poles are replaced by side PMs. The prototype uses an aluminum non-magnetic spacer to mechanically secure the side poles and side PMs.

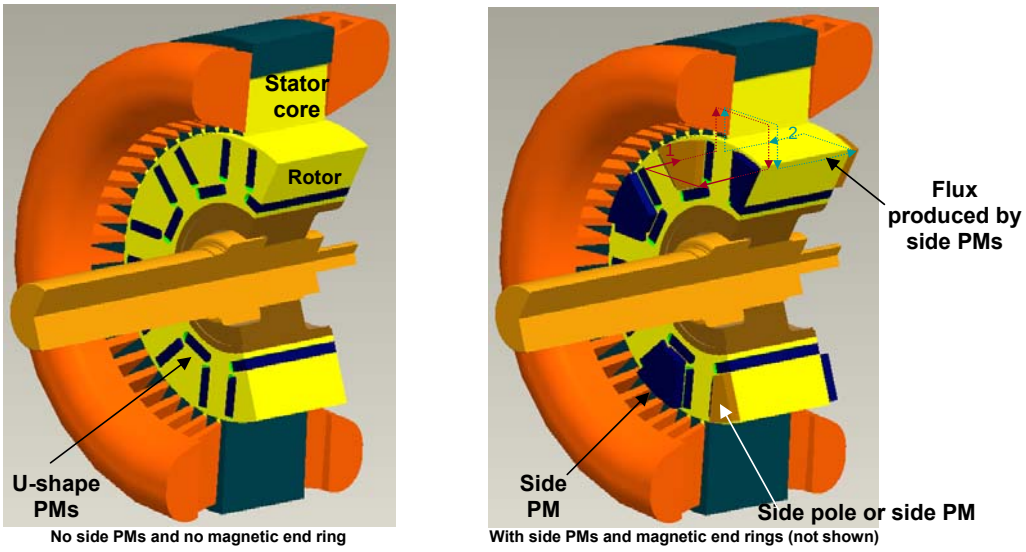

Figure 2. Various PM arrangements for increasing air-gap flux density.

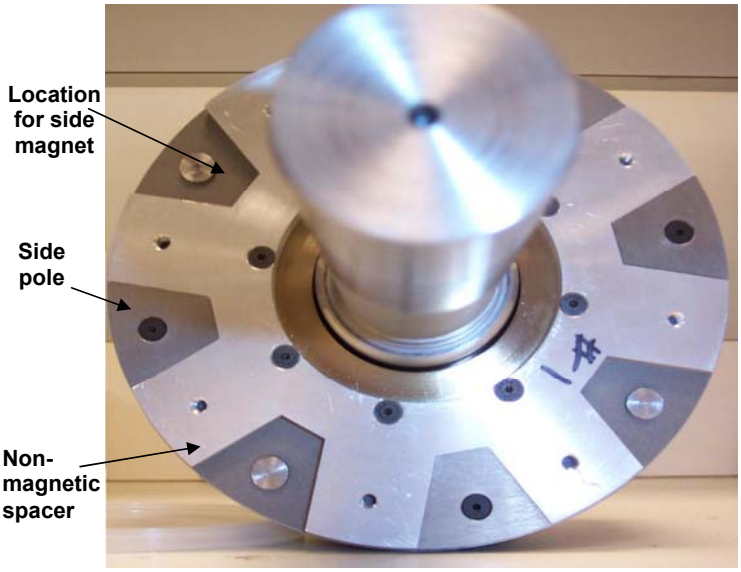

Figure 3. Prototype motor showing locations of side poles and side magnets.

Figure 4 shows the 3-dimensional finite element simulation results for the rotor flux density distributions produced by PMs only for the Toyota Prius; it shows no side-PM, partial side-PM, and full side-PM arrangements. Note that the very high flux density of the rotor is located in the narrow punching bridges on top of the PM grooves. The bridges magnetically short-circuit the PMs and become very saturated. These magnetically saturated bridges limit the flux that leaks from a rotor pole to its adjacent

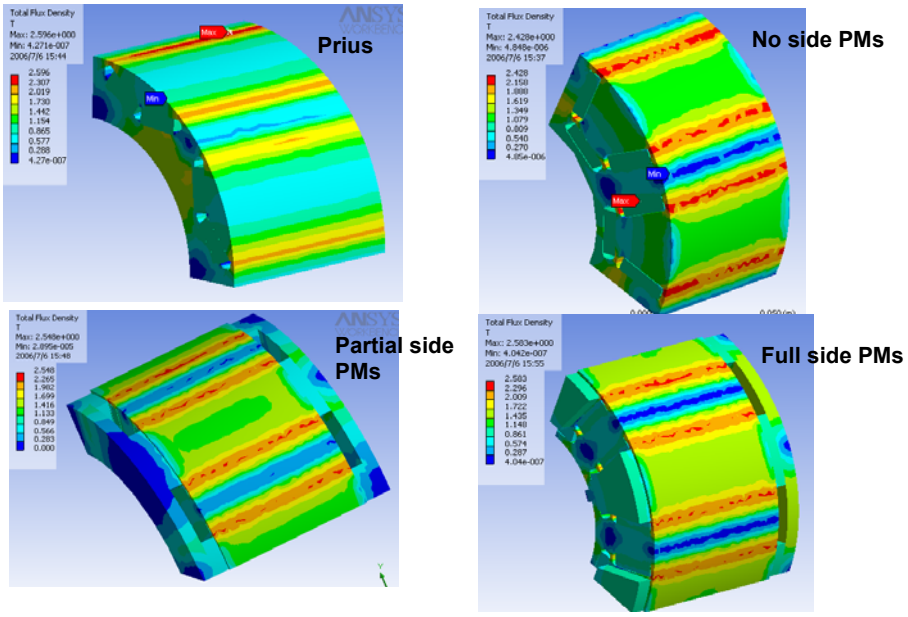

Figure 4. Three-dimensional simulation results for rotor flux density distributions.

pole. Because the bridge flux inside the bridge is mainly in the rotor peripheral direction, the radial air-gap fluxes at the bridge locations are relatively lower.

Figure 5 shows the radial air-gap flux distributions produced by the PMs for the four cases shown in Figure 4. The air-gap no-load flux density for the case of the U-shaped magnets plus full side PMs can reach double the value of the Prius air-gap no-load flux density.

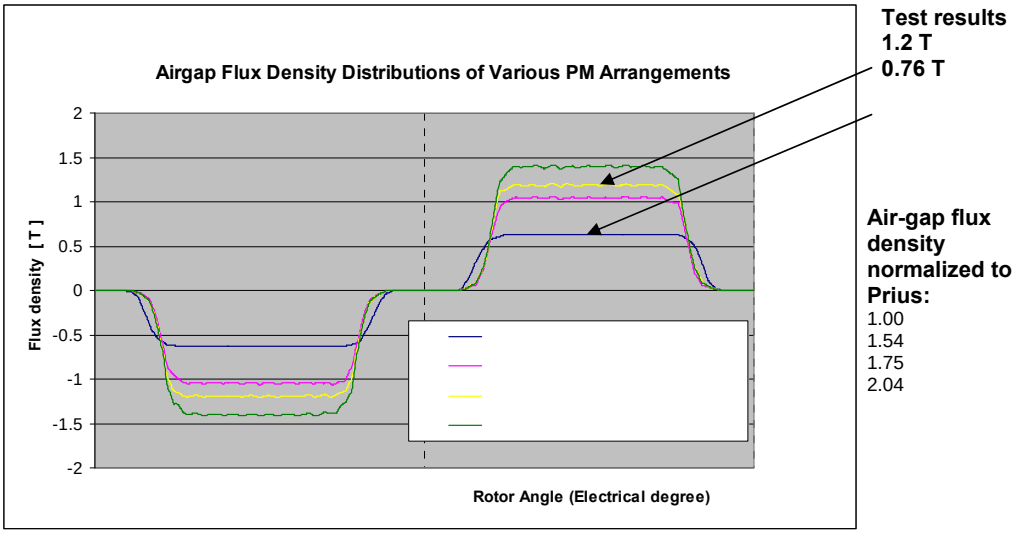

Figure 5. Comparison between simulation and test results of air-gap flux densities produced by PMs for various PM arrangements.

Conclusion

To improve the power density of existing RIPM motors, the rotor of an existing traditional machine was modified to contain additional side magnets. Because the motor being studied in this project does not use any additional external field excitation, it is more in line with conventional motor structures. The new technology resulting from this project can be used for either high- or low-speed motors. A dc/dc boost converter and/or a strong direct-axis current for field weakening might be needed for this motor at high speeds because of the high back-emf produced by the strong PM air-gap flux density.

The new technology derived from this project shows that the air-gap flux density produced by the PMs can be doubled compared with that of the Toyota Prius motor. Because the PM torque component is proportional to the product of the PM fundamental air-gap flux density and the current of the motor, higher PM fundamental air-gap flux density produces higher toque at a given current, yielding a higher-power-density motor.

This project was completed in FY 2006.

Future Direction

Beyond FY 2006, assistance to original equipment manufacturers for commercial prototypes will be provided as needed.

Patents

John Hsu, "Rotor Apparatus for High Strength Undiffused Brushless Electric Machine," U.S. Patent 6,989,619, January 24, 2006.

References

1. Munehiro Kamiya, "Development of Traction Drive Motors for the Toyota Hybrid System," Toyota Motor Corporation, 1, Toyota-cho, Toyota, Aichi, 471-8571, Japan.
2. Masaki Okamura, Eiji Sato, and Shoichi Sasaki, "Development of Hybrid Electric Drive System Using a Boost Converter," Toyota Motor Corporation, 1, Toyota-cho, Toyota, Aichi, 471-8572, Japan.

3.3 Control of Fractional-Slot Surface Mounted Permanent Magnet Motors with Concentrated Windings

Principal Investigator: John W. McKeever
Oak Ridge National Laboratory
National Transportation Research Center
2360 Cherahala Boulevard
Knoxville, TN 37932
Voice: 865-946-1316; Fax: 865-946-1262; E-mail: mckeeverjw@ornl.gov

DOE Technology Development Manager: Susan A. Rogers
Voice: 202-586-8997; Fax: 202-586-1600; E-mail: Susan.Rogers@ee.doe.gov

ORNL Program Manager: Mitch Olszewski
Voice: 865-946-1350; Fax: 865-946-1262; E-mail: olszewskim@ornl.gov

Objectives

The overall objective of this project is to develop techniques to analyze, design, and control fractional-slot concentrated-winding (FSCW) surface permanent magnet (SPM) synchronous machines; to investigate their possible use as a hybrid electric vehicle (HEV) traction motor; and if appropriate, to bring them into competition with internal permanent magnet motors. FSCW motors have potential for fault tolerant, wide constant power speed range (CPSR) operation because of their high inductance. They also have features that can reduce copper costs through improved slot utilization and elimination of copper end turns and reduce fabrication costs through simplified assembly methods.

A second objective, which is a subset of analysis and design, is to improve the model for calculating iron losses in the stator teeth and yoke, in the rotor, and in the magnets. Until more accurate estimates of these losses are available, reliable evaluation of the impact of minimizing them requires laboratory measurements.

Approach

The approach was to use closed-form analytical tools and commercial software to investigate and propose a design for a 55-kW FSCW motor. Originally, the plan was to build the 55-kW traction motor for testing. That approach was changed as it was felt that enough research had been completed on the FSCW motor that original equipment manufacturers could make the transition to market if they thought it had sufficient merit. Consequently, the product at the end of the year was a proposed 55-kW FSCW design whose analysis indicated that it could meet near term FreedomCAR targets.

We also developed a motor/inverter simulator to evaluate control schemes developed to improve efficiency of the FSCW-SPM motor. The approach was to test control schemes using the 6-kW FSCW prototype motor developed and tested at the University of Wisconsin, Madison (UWM), in FY 2005, mounted in a new frame that allowed liquid to cool the stator.

ORNL collaborated with UWM to test the control schemes developed. ORNL has a low cost scheme that controls at rated current or rated power to achieve maximum torque per amp below base speed and maximum power per amp above base speed. It is low cost because it eliminates current sensors. UWM has a modified vector control scheme to maximize motor efficiency at partial load. It determines the machine excitation that will provide the most favorable trade-off between copper losses and iron losses to achieve the highest possible efficiency under light-load conditions.

In FY 2006 the iron loss and magnet loss models were modified to extend the loss calculations to higher frequencies where skin effects alter the results. Plans call for this iron loss model to be

incorporated into the UWM FSCW-SPM machine design program. Point-by-point finite-element analysis (FEA) is being used to verify the iron loss predictions of the closed-form model whenever experimental test results are not available to provide this verification.

Major Accomplishments

1. Incorporated FreedomCAR targets to design and propose two 55-kW SPM motors with FSCWs for study in FY 2006. *SPM2* was selected for an analytical model comparison study. *SPM1* was selected for developing an analytical model to accurately predict the stator tooth and yoke iron losses in FSCW-SPM machines.
2. Modeled the *SPM2* motor with SPEED software and collaborated with UWM to compare design parameters calculated using SPEED's PC-BDC (brushless direct current) module with those calculated by UWM.
3. Created a rapid motor/inverter simulator using MatLab and checked its verity with time domain calculations using PSPICE software to show that the algorithms in the simulator are fast enough to use in a control circuit.
4. Successfully developed a closed-form analytical model that can accurately predict the stator tooth and yoke iron losses in FSCW-SPM machines during open-circuit operation. The status of this work will be included in this report.
5. Completed a detailed point-by-point FEA of FSCW-SPM machines that are proving very helpful in identifying the relative contributions of hysteresis and eddy-current losses in different parts of the machine as a function of rotor speed.
6. Developed three control schemes.
   a. The UWM scheme controls to ensure maximum motor efficiency. It shows how motor losses under load may be sufficiently reduced by field weakening, which increases total current, to offset the additional I^2R losses and thereby improve motor efficiency. This work is described in this report.
   b. The first ORNL scheme is a low-cost scheme because it eliminates current sensors. The ORNL simulator assumes losses that increase with the square of the speed.
   c. The second ORNL scheme uses a set of antiparallel silicon-controlled rectifiers (SCRs) in each phase to ensure that any load is accommodated with minimum current, which ensures that it is a maximum overall efficiency scheme.
7. Performed a successful FEA-based verification of a significant efficiency improvement (>5% at some speeds) that can be achieved in FSCW-SPM machines by using the modified vector control algorithm during partial-load operating conditions.
8. Evaluated the first ORNL control scheme with the simulator for two constraints, first so that rated current is not exceeded and second so that rated power is not exceeded. The limiting current constraint allows considerably more power to be delivered over a large part of the power speed curve.

Technical Discussion

Benefit and Use of Concentrated Windings

Introduction

Until John Hsu began research on motors with flux generated by an external coil and then directed into the rotor to modulate or even replace conventional magnet flux,[1] most of ORNL's PM motor research centered on axial- and radial-gap PM motors with distributed windings with one slot per pole per phase. To operate these motors above base speed, where the back-electromotive force (back-emf) equals the source voltage, making it difficult to deliver power from the source, a technique know as phase advance[2] had to be used. This technique had limitations that could be overcome by adding antiparallel SCRs in each of the three phases thereby increasing the maximum speed but also slightly increasing the cost because of the additional components. This new control technique, called dual mode inverter control,[3] was simulated using a "per-phase" model to show that the SCRs could be represented by a variable

inductance.[4] For PM motors, it has been recognized that one way to increase the maximum speed at which rated power is reached is to increase their inductance. A brute force way to do this was to add an inductor in each line, but a much better way would be to design the inductance into the motor itself. Designing the required inductance into the motor with distributed windings has been difficult as will be discussed later in this report.

In May 2004 an interim report prepared by UWM discussed significant benefits when a distributed winding is replaced by a concentrated winding.[5] The primary benefit is that the inductance necessary to allow high speed operation may be easily designed into the motor. Other benefits included improved fault tolerance, improved slot utilization because stator segments can be bobbin wound to achieve a higher fill factor, easier assembly because the segments can be assembled after winding, and a large reduction in the volume of copper used in end windings.

In FY 2005 ORNL's Power Electronics and Electric Machinery Research Center, in collaboration with UWM's Prof. Tom Jahns and his student, Dr. Ayman M. El-Rafaie, investigated applications of concentrated windings for use in HEV and fuel cell permanent magnet (PM) traction drives. During FY 2005 a 6-kW motor was designed and tested up to 4000 rpm[6] to validate the design procedure developed at UWM.[7] ORNL, a member of the SPEED Consortium at the University of Glasgow in Scotland, modeled the 6-kW design using SPEED software, a detailed motor development tool. The results generally agreed well. In FY 2006 UWM designed a 55-kW traction drive which met the 2010 FreedomCAR targets.[8] ORNL modeled the 55-kW motor, again getting good agreement except for the high speed magnet losses. During e-mail exchanges with the University of Glasgow we found that the algorithm used by SPEED does not consider skin effect, which would lead to increased resistance as the speed increases, and does not consider the effects of circumferential or axial magnet segmentation. The next release will use a 2-D finite-element program linked to a transient solver that produces files read by SPEED to calculate iron and magnet losses to solve the problem.

Distributed windings and concentrated windings

Technology for distributed stator windings has been around for 100 years and is well understood; consequently, it has long been the winding of choice for motor development. The amount of fundamental magnet flux linked by the stator winding coils determines the torque and power produced and is therefore the most important parameter of a PM motor. The reference winding that passes maximum flux is a distributed winding like the one shown in Figure 1(a). For each phase, full pitch coils bypass two slots for the other two phases. Two coils from adjacent poles are overlapped in one slot. This pattern is repeated for each pole and the coils are connected in series to complete the phase. The number of slots per pole per phase is 1. The back-emf is the algebraic rather than vector sum of each coil in a phase. An example of a concentrated winding similar to the one being investigated for use as an HEV traction motor is shown in Figure 1(b). Each coil winding is concentrated in two adjacent slots. After the first coil is wound in one direction, 4 slots are skipped, two for each of the other two phases, before the next concentrated coil is wound in the opposite direction to complete the stator pole pair. The 6-kW FSCW motor built and tested in FY 2005 and the 55-kW FSCW motor designed in FY 2006 have 36 slots and 30 pole pairs.

Winding function

The winding function is a representation of idealized stator coils. It is estimated from a process for counting conductors (personal communication between Professor Tom Jahns, UMW, and John McKeever, ORNL). First, Ampere's law is applied along closed curves to determine $H_g(\theta)$ referenced to $H(0)$. Then Gauss' law is applied to determine $H(0)$. All the wires are assumed to be at the center of the slot for convenience in analysis.

Both laws come from Maxwell's equations:

$$\nabla \times H = J \text{ and } \nabla \bullet B = 0 \quad . \tag{1}$$

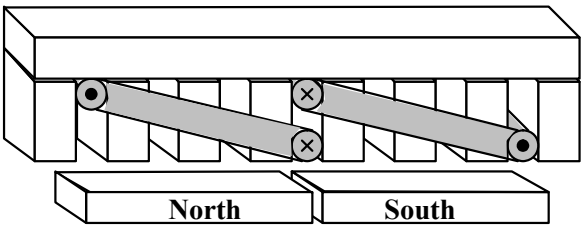

(a) Distributed winding (full pitch).

30 alternating N and S poles (15 pole pairs)

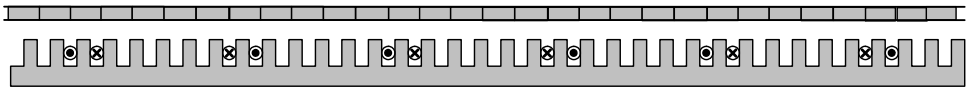

One phase consisting of 6 concentrated stator coils each occupying 2 slots.

(b) Concentrated winding for 36-slot, 30-pole configuration with N_{spp}=2/5.

Figure 1. Distributed and concentrated windings.

Stokes' theorem is applied to the surface integral of the left equality in Equation (1), producing a line integral on the left and the product of the number of turns inside the surface times the current in the turns, which is expressed as

$$\oint H(\theta) \bullet dl = n(\theta) i \quad . \tag{2}$$

The divergence theorem is applied to the volume integral on the right equality in Equation (1), which transforms the divergence of *B* over a volume to the integral of *B* over the surface of the volume, which says that the total flux crossing the surface sums to zero. This is expressed as

$$\int_{Surface} B \bullet dA = \int_{Surface} \mu_o H(\theta) L_{stack} r_{gap} d\theta = 0 \quad , \tag{3}$$

where

r_{gap} is the radius of the gap,
L_{stack} is the axial dimension of the rotor.

This technique is applied to a simple example shown in Figure 2.

The line integral of Equation (2) follows the contour abcd in the counterclockwise direction. Evaluation of the line integral in the stator or rotor is negligible because the value of μ, the magnetic permeability, is very large. Evaluation of the line integral in the gap where the value of μ is μ_o provides the primary contribution. Every line integral passes through H_{ref}, which is a constant whose value will be determined so that the total flux through the gap is zero. The direction of H_{ref} is arbitrarily chosen to be radial inward. The actual flux, which is proportional to $H(\theta)$, is radial inward and outward. The number of wires with current, *i*, encircled by the contour is expressed by $n(\theta)$. Wires with current into (minus) and out (plus) of the page are represented by the symbols "x" and "•," respectively. Contour integral evaluation is

$$H_{ref} g + H(\theta)\, g = n(\theta)\, i \quad , \tag{4}$$

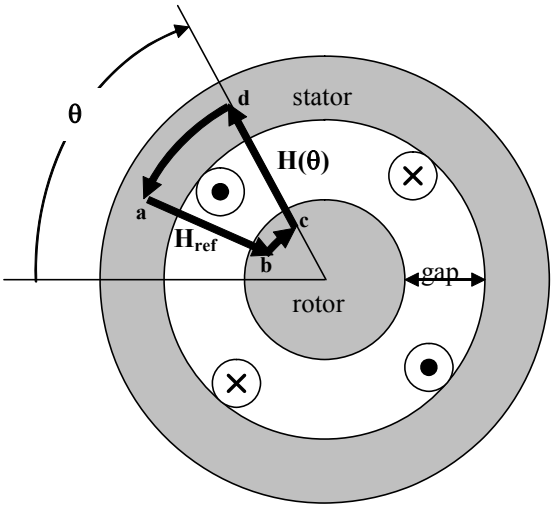

Figure 2. Calculation of the winding function for an idealized motor with a uniform gap.

where g is the gap between the rotor and stator.

This leads to

$$H(\theta) = \frac{n(\theta) i}{g} - H_{ref} \quad . \tag{5}$$

From Equation (3) it follows that

$$\int_{Surface} B \bullet dA = \mu_o r_{gap} L_{stack} \int_0^{2\pi} H(\theta) d\theta = 0 \quad . \tag{6}$$

Substituting the values from Equation (5) into Equation (6) leads to the value:

$$\int_0^{2\pi} \left[\frac{n(\theta) i}{g} - H_{ref} \right] d\theta = 0 \quad , \tag{7}$$

from which we get

$$H_{ref} = \frac{i}{g} \frac{1}{2\pi} \int_0^{2\pi} n(\theta) d\theta = \frac{i}{g} \overline{n(\theta)} \quad . \tag{8}$$

The bar over $n(\theta)$ denotes an average value. If we now substitute Equation (8) into Equation (5), we find that

$$H(\theta) = \frac{i}{g} \left[n(\theta) - \overline{n(\theta)} \right] = \frac{i}{g} N(\theta) \quad . \tag{9}$$

The term in brackets defines the winding function $N(\theta)$. From Equation (4), recall that $n(\theta)$ is the number of wires enclosed by the contour, counting wires into the page as minus and wires out of the page as plus. For the example shown in Figure 2, Figure 3(a) shows a plot of $n(\theta)$, the conductor count versus angle, and Figure 3(b) shows a plot of $N(\theta)$, the winding function.

The winding function indicates the regions in which flux would be produced by current in the conductors and the direction of the flux. None of the preceding discussion has mentioned the magnet pole pairs, which would be attached on the surface of the rotor to interact with the stator conductors. When p pole pairs are introduced, $N(\theta)$ determines the stator regions that link the magnets' flux. The motor's torque is determined by the flux linkages, which will be discussed shortly.

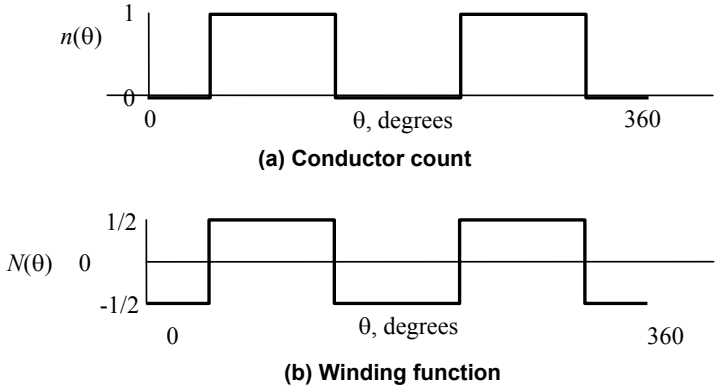

Figure 3. Relation between conductor count and winding function.

Winding factor

The winding function discussed in the previous section is related only to the number of slots and assumes that all of the conductors are placed at the midpoint of each slot to produce a square wave like the one shown in Figure 3(b). The winding factor, which is the subject of this section, is the ratio of actual flux links, ψ_{actual}, to the ideal flux links, ψ_{ideal}, across the gap. The flux links are proportional to the integral from 0 to 2π of the product of the winding function with the magnetic field. In this explanation the magnetic field is approximated by $B = B_{max}\cos(p\theta)$, where p is the number of magnet pole pairs. The actual and ideal winding functions are both expressed as Fourier series.

Recall that the form of the Fourier expansion is

$$N(\theta) = \sum_{n=1}^{\infty} a_n \cos(n\theta) + \sum_{n=1}^{\infty} b_n \sin(n\theta) \quad , \tag{10}$$

where

$$a_n = \frac{\int_0^{2\pi} N(\theta)\cos(n\theta)d\theta}{\pi} \text{ and}$$

$$b_n = \frac{\int_0^{2\pi} N(\theta)\sin(n\theta)d\theta}{\pi} \ .$$

Figure 4 shows the actual winding function, which is a square wave positioned symmetrically so that only the coefficients of the cosine terms survive. The expansion of the actual concentrated winding function is

$$N_{actual}(\theta) = \sum_{n=1,3,5..}^{\infty} a_n \cos(n\theta) \quad . \tag{11}$$

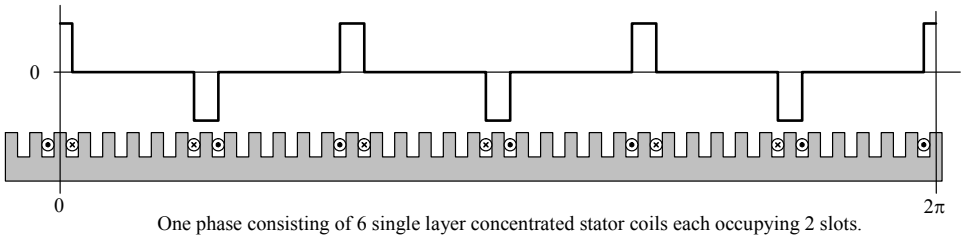

Figure 4. Winding function for the 36-slot, 30-pole concentrated winding being studied for possible use as a hybrid electric vehicle traction motor.

As an illustration, Fourier coefficients of the winding function for the concentrated winding in Figure 4 with $N(\theta) = \pm 1$ inside the coils and 0 elsewhere are shown in Table 1.

Table 1. Fourier coefficients of winding function for a stator with 36 slots

n	a_n	b_n	n	a_n	b_n	n	a_n	b_n
1	0	0	7	0	0	13	0	0
2	0	0	8	0	0	14	0	0
3	0.32954	0	9	0.30011	0	15	0.24597	0
4	0	0	10	0	0	16	0	0
5	0	0	11	0	0	17	0	0
6	0	0	12	0	0	18	0	0

The quantity, N_{spp}, which is the number of slots per pole per phase, is a useful design parameter. It provides the following useful relations for a three-phase winding with p equal to the number of magnet pole pairs and the $N_{slots/coil}$ equal to the number of slots per coil:

$$N_{coils/phase} = \frac{N_{spp}(2p)}{N_{slots/coil}} \quad ,$$

$$N_{slots} = N_{spp}\,3(2p) \quad ,$$

$$N_{slots/phase} = N_{spp}(2p) \quad ,$$

and

$$N_{slots/pole} = N_{spp}\,3 \quad .$$

Because an equivalent distributed winding with $N_{spp} = 1$ produces maximum flux links, it is used to estimate the ideal flux links used in the denominator of the winding factor. The six concentrated winding coils, N_{conc}, shown in Figure 4, are reconfigured with no change in coil dimension over one pole pair in the form of a distributed winding ($N_{spp} = 1$) as shown in Figure 5(a). N_{spp} is the number of slots per pole

per phase. When the magnetic field is symmetrically positioned within the coils, this is the configuration that has the maximum flux linkages as shown in Figure 5(b).

Equation (12) gives the ideal number of flux links for one pole pair and Equation (13) the actual number of flux links for the concentrated winding.

$$\psi_{ideal} = L_{stack} \frac{N_{coils/phase}^{conc}}{2} 2 \int_0^{\pi/p} B_{\max} \sin(p\theta) r_{gap} d\theta = \left[r_{gap} L_{stack} B_{\max} \right] \frac{N_{coils/phase}^{conc}}{2} \frac{4}{p} \quad . \tag{12}$$

$$\psi_{actual} = L_{stack} \int_0^{2\pi} \sum_{n=1,3,5..}^{\infty} a_n \cos(n\theta) B_{\max} \cos(p\theta) r_{gap} d\theta = \left[r_{gap} L_{stack} B_{\max} \right] a_p \pi \quad . \tag{13}$$

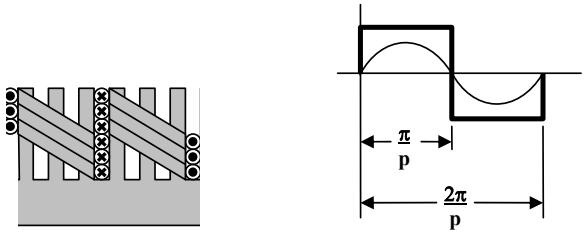

(a) One pole pair.

(b) Distributed winding function and magnetic field for one pole pair.

Figure 5. Redistribution of the coils from the concentrated winding shown in Figure 4 into an ideal distributed winding for a rotor with p pole pairs.

Noting that the Fourier coefficient, a_p, is a function of the number of slots, we find that the expression for the winding factor is

$$k_w(N_{slots}, p) = \frac{\psi_{actual}}{\psi_{ideal}} = \frac{a_p \pi}{2 N_{spp}} \quad . \tag{14}$$

The winding factor for the concentrated winding with 36 slots and 15 pole pairs is

$$k_w(36,15) = \frac{0.24597 x \pi}{2\frac{2}{5}} = 0.9659 \ ,$$

which indicates that this configuration, whose N_{spp} = 2/5, yields flux links close to the ideal value.

Concentrated winding (fluxmate) equivalent of a motor with distributed windings

The purpose of this section is to relate a distributed winding for which N_{spp} = 1 to a corresponding single layer concentrated winding and to quantify the amount by which the inductance of the concentrated winding is increased. N_{spp} = 2/5 for the corresponding concentrated winding being examined for use as an HEV traction motor. Another configuration that has the same winding factor has N_{spp} = 2/7. Equations will be used to illustrate how the concentrated winding may be used to design increased inductance into

an SPM motor. As $N_{spp} = 1$ for distributed windings, the quantity N_{spp} in the following equations will refer to the fractional value for the concentrated windings.

For the first step we start with a distributed winding with p magnetic pole pairs and $6p$ slots and determine the number of slots for the concentrated winding specified by its N_{spp}. The corresponding concentrated winding has $N_{slots}^{conc} = N_{spp}(6p)$ slots. For a distributed winding with $6p$ slots and 15 magnetic pole pairs, the corresponding concentrated winding with $N_{spp} = 2/5$ has 36 slots.

Next we ensure that the flux linking the coil for each phase is the same for the two configurations. For the distributed winding, the flux links in one phase are

$$\psi^{dist} = \int_0^{2\pi} \frac{N_{turns}^{dist}}{2} B_{\max} \left|\cos(p\theta)\right| L_{stack} r_{gap} d\theta \quad . \tag{15}$$

The magnet flux is symmetrically positioned in the winding function so that the product of their signs results in the absolute value of the cos term. This may be evaluated with the integral

$$\psi^{dist} = 4p \int_0^{\frac{2\pi}{p}\frac{1}{4}} \frac{N_{turns}^{dist}}{2} B_{\max} L_{stack} r_{gap} \cos(p\theta) \frac{d(p\theta)}{p} = 2N_{turns}^{dist} B_{\max} L_{stack} r_{gap} \quad . \tag{16}$$

For the concentrated winding, the flux links in one phase are

$$\psi^{conc} = \int_0^{2\pi} N_{turns}^{conc} \sum_{n=1,3..}^{\infty} a_n \cos(n\theta) B_{\max} \cos(p\theta) L_{stack} r_{gap} d\theta = N_{turns}^{conc} B_{\max} L_{stack} r_{gap} \pi a_p \quad . \tag{17}$$

When Equation (16) is equal to Equation (17), the ratio of turns for the concentrated winding to the distributed winding is

$$\frac{N_{turns}^{conc}}{N_{turns}^{dist}} = \frac{2}{\pi a_p} \quad . \tag{18}$$

Equation (14) relates the value of a_p to the value of the winding factor. Also in Equation (14) the number of coils/phase for the concentrated winding, which is a single layer winding with $N_{slots/coil}^{conc} = 2$, is $N_{coils/phase}^{conc} = N_{spp} p$. From these relations, Equation (18) may be expressed as

$$\frac{N_{turns}^{conc}}{N_{turns}^{dist}} = \frac{1}{N_{spp} k_w} \quad . \tag{19}$$

For our study example, $N_{spp} = 2/5$ and $k_w = 0.9659$ yielding a ratio of 2.588. This value is also obtained from Equation (18) by using the value of a_{15} from Table 1.

Next we discuss inductance andthe relation between the inductance of distributed windings and that of concentrated windings. Inductance is the proportionality constant between the current flowing in one set of coils and the flux that it produces, which may link the coil producing the flux (self-inductance) or another coil (mutual inductance). The mutual inductance between phases for distributed windings is 1/3 the self-inductance because only 1/3 of any pair of coils from different phases overlap; however, the mutual inductance between phases of concentrated windings is zero because the concentrated winding

coils have no overlap. This may be seen by inspection of Figure 4 and with the addition of the other phase coils. No rectangle in one phase intersects a rectangle in another phase.

We shall consider the two main types of inductance in a PM motor, self-inductance and slot-leakage inductance. Self-inductance is related to flux that crosses the gap and interacts with the magnet. Slot-leakage inductance links wires in each slot but does not contribute to torque production. Both inductances are additive, producing the reactive impedance that must be overcome in the electrical circuit. End turn leakage inductance makes a much smaller contribution to the total inductance and is not included in this discussion. The following equations show the relationship between self-inductance and leakage inductance for the distributed and concentrated windings.

Self-inductance

Self-inductance over one phase is

$$L_{self} = c \int_0^{2\pi} \left(N_{self}(\theta) \right)^2 d\theta^2 \quad , \tag{20}$$

where c = $\mu_o \; r_{gap} \, L_{stack}/g$ and g is the gap between the magnets and the stator teeth. For the distributed winding function the value in parentheses in Equation (20) contributes a constant value, $\left(\frac{N_{turns}^{dist}}{2} \right)^2$, over an angular distance, $2\pi/p$, a total of p times, which by inspection is

$$L_{self}^{dist} = c \left(\frac{N_{turns}^{dist}}{2} \right)^2 \left[\frac{2\pi}{p} \right] \text{rad per pole} \left[p \right] poles = c \left(N_{turns}^{dist} \right)^2 \frac{\pi}{2} \quad . \tag{21}$$

For a concentrated winding, the value in brackets for Equation (20) contributes a constant value, $\left(N_{self}^{conc} \right)^2$, over 1/3 of the stator so that

$$L_{self}^{conc} = c \left(N_{turns}^{conc} \right)^2 \left[\frac{\pi}{3} \right] \quad . \tag{22}$$

The ratio of the inductance of the concentrated winding to that of the distributed winding is

$$\frac{L_{self}^{conc}}{L_{self}^{dist}} = \frac{2}{3} \frac{1}{\left[N_{spp} k_w \right]^2} \quad . \tag{23}$$

For the concentrated winding of interest this ratio is 4.47.

Slot-leakage inductance

Slot-leakage inductance over one phase is

$$L_{slot\_leakage} = \mu_o L_{stack} N_{spp} (2p) \left[N_{turns} \right]^2 \left[\frac{h_s^2}{3A_s} + \frac{d_2}{(b_o + w_s)/2} + \frac{d_1}{b_o} \right] \quad , \tag{24}$$

where the dimensions of the slot are shown in Figure 6. A_s is the area of the slot and r_s is the outer radius of the slot.

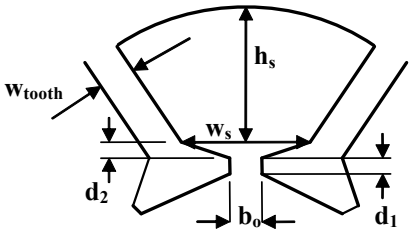

Figure 6. Definition of slot dimensions for inductance calculations.

The area of the slot is

$$A_s = \frac{\pi(r_s^2 - (r_s - h_s)^2)}{N_{spp} 3(2p)} - h_{tooth} w_{tooth} \quad . \tag{25}$$

Flux is carried by all teeth adjacent to a pole and is channeled in both directions in the back iron. The tooth width is chosen to be wide enough to prevent saturation. Its width is given by

$$w_{tooth} = \frac{2 w_{back\_iron}}{3 N_{spp}} \quad , \tag{26}$$

where $3N_{spp}$ is the number of slots per magnet pole to carry the flux. The fact that the back iron handles half the flux is described by the equation

$$w_{back\_iron} = \frac{\phi_g}{2 B_{\max} L_{stack}} \quad . \tag{27}$$

The final equation for the width of the tooth is

$$w_{tooth} = \frac{\phi_g}{3 N_{spp} B_{\max} L_{stack}} \quad , \tag{28}$$

which leads to the ratio for the width of a tooth in a concentrated winding to the width of a tooth in a distributed winding:

$$\frac{w_{tooth}^{conc}}{w_{tooth}^{dist}} = \frac{1}{N_{spp}} \quad . \tag{29}$$

Using Equation (29) with Equation (25) and a similar procedure for the slot's arc radius, we find that both the ratio of the slot area in a concentrated winding to the slot area in a distributed winding and the ratio of the slot arc width in a concentrated winding to the arc width in a distributed winding are the same:

$$\frac{A_s^{conc}}{A_s^{dist}} = \frac{1}{N_{spp}} = \frac{w_{slot}^{conc}}{w_{slot}^{dist}} \quad . \tag{30}$$

When these relations are substituted into Equation (24) for the slot leakage of the concentrated winding and for the distributed winding, the ratio of the two inductances is

$$\frac{L_{slot\_leak}^{conc}}{L_{slot\_leak}^{dist}} = \left[\frac{1}{k_w}\right]^2 \frac{\left[\frac{h_s^2}{3A_s^{dist}} + \frac{d_2 2}{(N_{spp}b_o + w_s^{dist})} + \frac{d_1}{N_{spp}b_o}\right]}{\left[\frac{h_s^2}{3A_s^{dist}} + \frac{d_2 2}{(b_o + w_s^{dist})} + \frac{d_1}{b_o}\right]} \quad . \tag{31}$$

The value of $1/(k_w)2$ is 1.07. The ratio of the terms in brackets shows that the $N_{spp}b_o$ term has the effect of reducing the effective slot width. Using the parameters $h_s = 25.4$ cm, $A_s^{dist} = 125$ mm, $w_s^{dist} =$ 4 mm, $d_2 = 3$ mm, $d_1 = 3$ mm, and $b_o = 2$ mm, which represent the slot of the 55-kW motor with concentrated windings being studied, we find that the three terms in the upper right bracket of Equation (31) are 1.72 + 1.25 + 3.75, and the three terms in the lower right bracket are 1.72 + 1.0 + 1.5. The ratio is 1.59, caused by the impact that N_{spp} has on the effective slot opening, b_o. The ratio of the bracketed terms cannot be ignored. The contribution of the slot opening to the slot-leakage inductance is large. For the example under study, the ratio of concentrated to distributed slot-leakage inductances is

$$\frac{L_{slot\_leak}^{conc}}{L_{slot\_leak}^{dist}} = 1.07 \times 1.59 = 1.70 \quad . \tag{32}$$

The total inductance is the sum of the self-inductance and slot-leakage inductance. From Equations (23) and (31), the total inductance is

$$L_{total} = \frac{2}{3}\left[\frac{1}{N_{spp}k_w}\right]^2 L_{self}^{dist} + \frac{1}{k_w^2} L_{slot\_leak}^{dist} \quad , \tag{33}$$

which for the case of interest is $L_{total} = 4.47L_{self}^{dist} + 1.70L_{slot\_leak}^{dist}$, clearly showing the increase in inductance from the concentrated windings—mainly in the self-inductance, but also in the slot-leakage inductance.

Finally, we examine the larger slot area of the concentrated winding, which has a fill factor of 0.7 compared to 0.5 for a distributed winding, to see whether it can accommodate the larger number of turns. First recognize that the useable area of the slot for the distributed winding is $A_{useable}^{dist} = 0.5A_s^{dist}$ and that the useable area of the slot for the concentrated winding is $A_{useable}^{conc} = 0.7A_s^{conc} = 0.7\frac{A_s^{dist}}{N_{spp}}$. The ratio of useable areas is

$$\frac{A_{useable}^{conc}}{A_{useable}^{dist}} = \frac{1.4}{N_{spp}} \quad , \tag{34}$$

which for the case of interest is 3.5, meaning that the slot in the concentrated winding can handle 3.5 times the number of turns in the slot of the distributed winding. This will work because the number of distributed turns from Equation (19) must be multiplied by 2.588 to have the same flux links. In fact, only a small improvement in fill factor from 0.5 to 0.5176 will allow the desired 2.588 useable area ratio.

Analysis and Design of Motors with Fractional-Slot Concentrated Windings

Design of an FSCW HEV traction drive motor

A summary of the FreedomCAR targets shown in Table 2 was incorporated by UWM and ORNL to scale the design of a 6-kW FSCW motor built and tested in FY 2005[6] to 55-kW for use as an HEV traction drive motor.[8] The design is a 36 slot-30 pole configuration built from six repeating units, each having six slots and five poles, which can be wound separately and then assembled into the final stator for ease of manufacturing (Figure 7). At the same time, the fractional-slot concentrated winding develops sufficient inductance to allow the required CPSR of 5 from base speed of 2000 rpm to top speed of 10,000 rpm.

Table 2. FreedomCAR traction motor targets

Requirement	Target specification
Minimum top speed [rpm]	10,000
Peak power at 20% of max speed for 18 s and nominal voltage [kW]	55
Continuous power at 20 to 100% of maximum speed and nominal voltage [kW]	30
Battery operating voltage [V_{dc}]	*Nominal:* 325 *Range:* 200 to 450
Maximum current at motor [A_{rms}]	400
Characteristic current [A_{rms}]	< Max current
Efficiency at 10 to 100% of max speed rated power	>93%
Efficiency at 10 to 100% of max speed for 20% of rated torque	>93%
Torque pulsations—not to exceed at any speed [% of peak torque]	<5
Peak power to weight ratio for active materials [kW/Kg]	>2.75
Peak power to volume ratio for active materials [kW/liter]	>12.5

UWM has developed its own software design methodology[7] while ORNL has used the SPEED software from Motorsoft. The design parameters have been developed using the UWM software and verified using SPEED software. The motor as sketched by the SPEED software in Figure 8 consists of six of the segments shown in Figure 7. There are some differences, including the following.

1. SPEED has 30 turns per phase of AWG #19 wire with each turn consisting of 47 conductors and a fill factor of 70%, whereas UWM fills each slot with copper at the same fill factor.
2. SPEED uses ARNON 7 for the laminations, while UWM uses a general lamination model.[9]
3. The present version of SPEED does not consider skin effects nor does it allow segmentation in the circumferential direction, while UWM segments each magnet circumferentially into five pieces.[8]

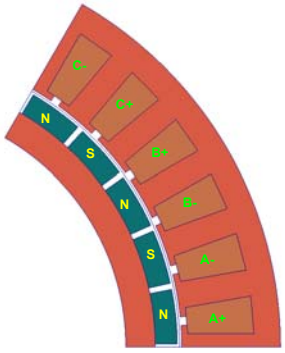

Figure 7. Cross-section of the basic repeating unit of the 55-kW (peak), 36-slot 30-pole (2/5 s/p/ph) *SPM2* machine design.

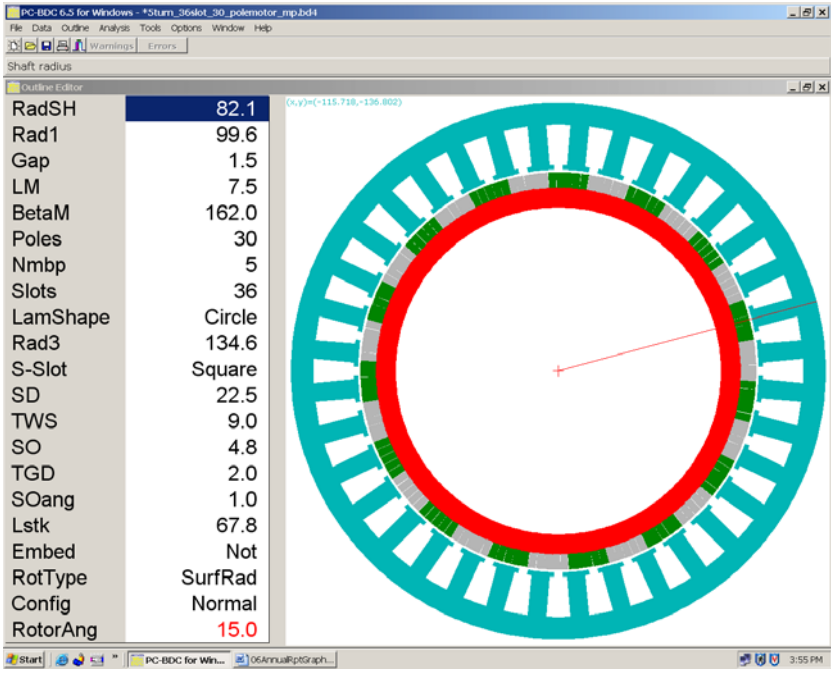

Figure 8. SPEED rendition of the 36-slot, 30-pole *SPM2* with concentrated windings.

A comparison of the results of the two programs is shown in Table. 3.

Table 3. Comparison of UWM and ORNL design parameters for the proposed 55 kW (PEAK) SPM

Design parameter	UWM	ORNL	Remarks
Inductance, [μh]			
Self	**25.5**	**29**	
Slot	41	40	
End	–	4	
Total	66.5	73	
Phase resistance, [mohms]	4.9	4.15	
Fundamental magnet flux linkages [mWebers]	17.5	18.42	
Characteristic current [A_{rms}]	264	252	
Line-to-line back-emf [V_{rms}]	120	124	@ 2000 rpm
Rated current [A_{rms}]	230	181	
Current density [A_{rms}/mm^2]	6.7	5.9	
Base speed efficiency [%]	93	97	@ 2000 rpm
Top speed efficiency [%]	92	87.7	@ 10,000 rpm
Core loss [W]	1676	206	@ 2000 rpm
Armature loss [W]	780	309	@ 2000 rpm
Magnet loss [W]	1288	882	@10000 rpm
Mass [kg]			
Iron	10.3	11.1	
Copper	8.8	4.6	
Magnet	2.2	2.1	
Total	17.3	17.8	

The most significant difference between the two design calculations is the losses. The two methods are explained in the next section.

Core loss calculations

Core loss data from steel suppliers is almost always sinusoidal data and may be characterized by the Steinmetz equation with separate terms for hysteresis and eddy current losses:

$$P = C_h f B_{pk}^n + C_e f^2 B_{pk}^2 \quad , \tag{35}$$

where

P is the power per unit mass, W/kg,
B_{pk} is the peak flux density, T,
f is the frequency, Hz,
C_h is the hysteresis loss coefficient,
C_e is the eddy current loss coefficient.

The exponent, n, is often assumed to be 1.6 to 1.8 but varies some with B_{pk}, and SPEED allows a linear variation in the form $n = a + bB_{pk}$, in which both a and b should be positive.

The flux density in motor laminations may be far from sinusoidal. SPEED uses a modified Steinmetz equation

$$P = C_h f B_{pk}^{a+bB_{pk}} + C_{el} \left| \frac{dB}{dt} \right|^2 \quad . \tag{36}$$

The hysteresis loss component is unchanged, but the eddy-current component is taken to be proportional to the mean squared value of dB/dt over one cycle of the fundamental frequency. SPEED programs apply Equation (36) in the respective sections of the magnetic circuits after calculating the relevant flux-density waveforms.

The eddy current loss coefficient, C_{el}, in the modified form can be derived from the sine wave coefficient, C_e, if we assume that Equation (36) is true when $B = B_{pk} \sin(2\pi f t)$. If so, then $\left| \frac{dB}{dt} \right|^2 = 4(\pi f B_{pk})^2 \cos^2(2\pi f t)$ whose mean value is $\left| \frac{dB}{dt} \right|^2 = 2(\pi f B_{pk})^2$. For the sine wave flux density, Equations (35) and (36) give the same result if $C_{el} = \frac{C_e}{2\pi^2}$. The loss coefficients in the SPEED program have names related to the quantities in Equation (36) as shown in Table 4. The core losses versus speed for ARNON 7 laminated steel are shown in Table 5.

Table 4. Speed software loss equation coefficient definitions

Name in design program	Name in Equation (36)
CfC_h	C_h
Cfa	a
Cfb	b
CfC_e	C_{el}

Table 5. Core losses for ARNON 7 laminations in the 55-kW FSCW-SPM motor

RPM	Loss, W
2000	206
4000	577
6000	1113
8000	1814
10,000	2681

The UWM core loss method follows that of Mi, Slemon, and Bonert.[9] UWM uses a revised approximate model for tooth eddy-current loss. For an m-phase PM motor with *q* slots per pole per phase, there are mq slots per pole. The time, Δt, required for the magnet to pass one tooth is

$$\Delta t = T \frac{1}{m2q} \quad , \tag{37}$$

where

T is the time for a pole pair to pass a slot pitch, which is $2\pi/\omega_{elect}$,
m is the number of phases,
$2q$ is the number of slots per pole pair,
ω_{elect} is the electrical rotational speed of the rotor, rad/s.

Under linear trapezoidal assumptions of the waveforms, the time rate of tooth flux change is

$$\frac{dB}{dt} = \frac{B_{tooth}}{\Delta t} \quad . \tag{38}$$

The change of tooth flux density occurs four times per time period, T. The average eddy current loss density in the teeth can now be expressed as

$$p_{eddy\_current} = 2k_e \overline{\left(\frac{dB_{tooth}}{dt}\right)^2} = 2k_e \left(\frac{B_{tooth}}{\Delta t}\right)^2 \left(\frac{4\Delta t}{T}\right) = 16k_e mq \left(\frac{B_{tooth}}{T}\right)^2 \quad . \tag{39}$$

Multiplying by the number of phases and expressing T in terms of the electrical frequency we obtain the expression,

$$p_{eddy\_current} = 12k_e q \left(\frac{\omega_{elect} B_{tooth}}{\pi}\right)^2 \quad . \tag{40}$$

From Equation (39) it can be seen that the eddy current loss is proportional to the number of slots per pole.

The equation for the eddy current losses in the teeth used by UWM[7] is

$$p_{et} = \frac{4m}{\pi^2} q k_q k_l k_e \left(\omega_e B_{tooth}\right)^2 \quad , \tag{41}$$

where

k_q is the motor geometry correction factor,
k_l is a correction factor to account for the contribution of the circumferential component,[9]
k_e is the eddy current constant that depends on the lamination material.

The value of flux density in the tooth is estimated by the equation

$$B_{th} = \frac{w_t + w_s}{w_t} B_{gap}^{pk} \quad , \tag{42}$$

where B_{gap}^{pk} is the peak air gap magnetic flux density. Its value is estimated by

$$B_{gap}^{pk} = \frac{V_{ag}^{rms} p}{\sqrt{2} R_s L_{stack} k_{w1} \omega_e} \quad , \tag{43}$$

where

w_t is the tooth width,
w_s is the slot width,
V_{ag}^{rms} is the rms air gap voltage supply,
k_{w1} is the fundamental winding factor,
ω_e is the electrical frequency in rad/s.

The corresponding equation for the eddy current losses in the yoke is

$$p_{ey} = \frac{1}{\alpha} \frac{8}{\pi^2} k_e k_r \left(\omega_e B_y\right)^2 \quad , \tag{44}$$

where α is the ratio of the magnet span to the pole pitch, B_y is the peak magnetic flux in the stator yoke, and

$$k_r = 1 + \frac{8 k_q d_y^2}{27 \alpha q \lambda_2^2} \quad , \tag{45}$$

where d_y is the stator yoke thickness and λ_2 is the projected slot pitch at the middle of the yoke.

Tooth hysteresis loss and yoke hysteresis loss can be expressed as a function of the maximum flux density in each area. In the teeth the hysteresis loss density is

$$p_{ht} = k_h \omega_{elect} B_{th}^{\beta} \quad . \tag{46}$$

In the yoke the hysteresis loss density is

$$p_y = k_h \omega_{elect} B_{yk}^{\beta} \quad . \tag{47}$$

These are the forms used by UWM.

Magnet loss calculations

The magnet loss algorithm in the SPEED software does not account for the effect of skin depth on magnet loss. A finite-element transient solver has been added to the SPEED software package for its next release. Output from the new package has been provided for ORNL's 55-kW FSCW motor by SPEED's technical support at the University of Glasgow in Scotland. That output is shown in Figures 9 through 13.

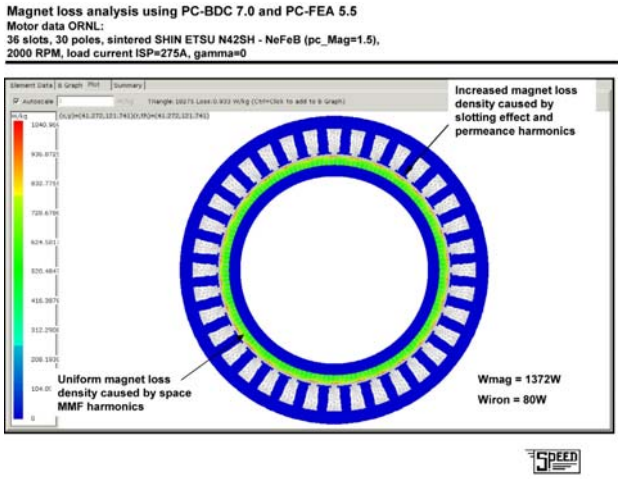

Figure 9. Magnetic loss at 2,000 rpm. (The motor is drawing 275 A ISP under load. Losses are the result of space harmonics, slotting, and permeance. At 2000 rpm the electrical frequency is 500 Hz.)

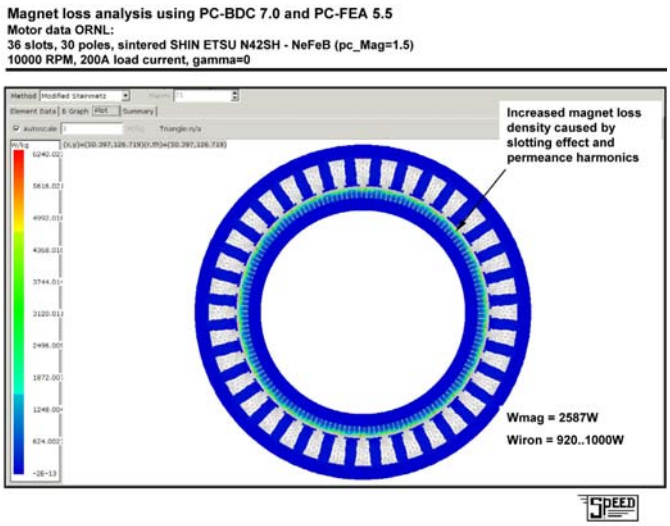

Figure 10. Magnet loss at 10,000 rpm.

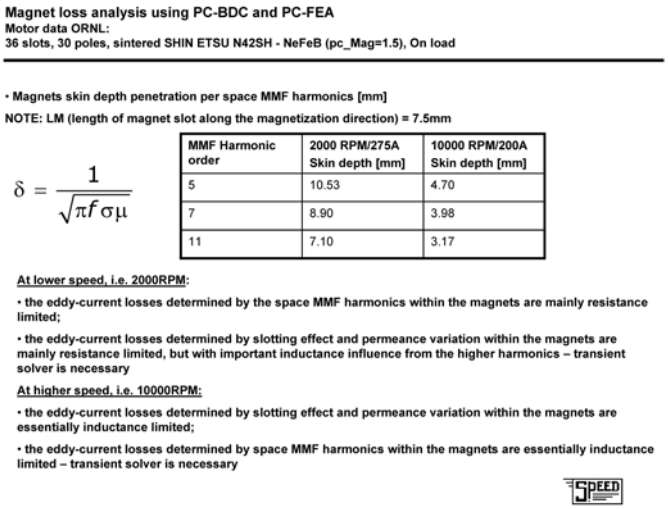

Figure 11. Effect of speed on skin depth penetration.

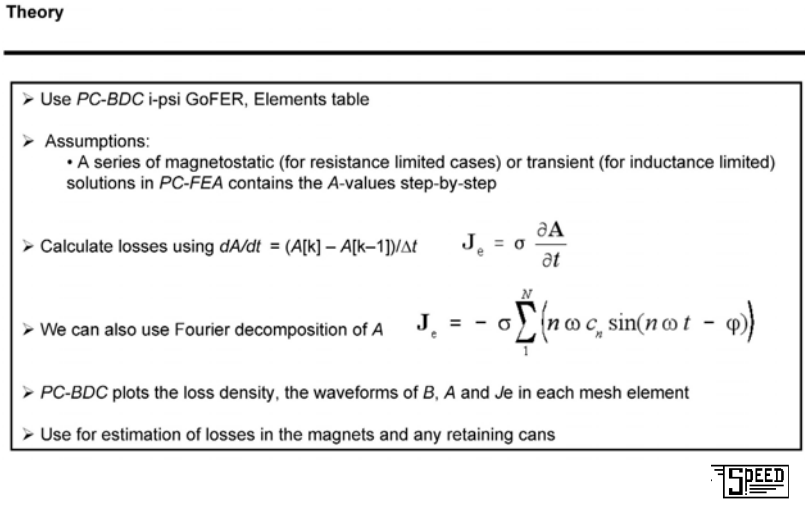

Figure 12. Approach taken by SPEED to determine skin depth penetration.

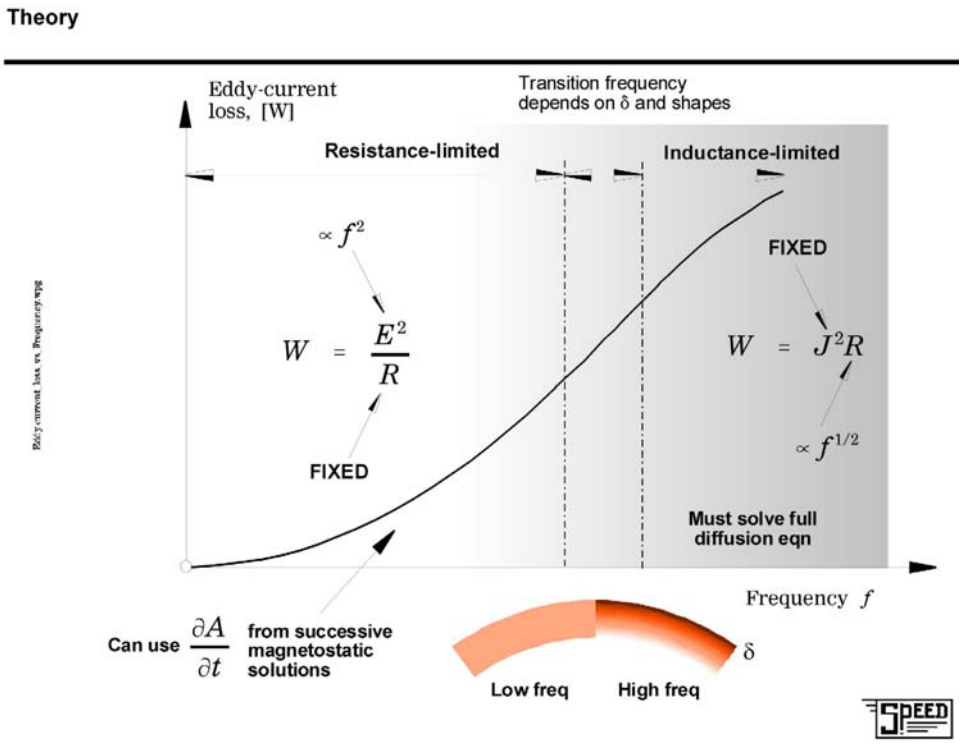

Figure 13. The effect of frequency on magnetic losses.

While the speed has increased fivefold, the loss has increased by a factor of about 2. This is because of the skin effect, shown in Figure 11.

UWM has almost the same procedure as shown in Figures 12 and 13 except for the addition of skin depth penetration. Figure 13 shows that skin effect lowers the magnet loss at high frequencies. This explains why the UWM magnet loss at 10,000 rpm in Table 6 is higher that the value obtained by SPEED.

The procedure used by UWM[10] characterizes the stator winding as a current sheet in the rotor reference. The time dependent expression for current density in the sheet in terms of the angle, θ_r, in the rotor is

$$J_s(\theta_r,t) = \frac{q}{2}\sum_n J_n \cos\left(np_s\theta_r + (np_s - mp_r)\Omega t\right) \text{ for } n = qk+m \ ,$$

$$J_s(\theta_r,t) = \frac{q}{2}\sum_n J_n \cos\left(np_s\theta_r + (np_s + m * p_r)\Omega t\right) \text{ for } n = qk - m \ ,$$

$$J_s(\theta_r,t) = 0 \text{ for n} \neq \text{qk} \pm \text{m} \ , \qquad (48)$$

where

q is the number of phases,
m = -1 when N_{spp}=2/5 and +1 when N_{spp}=2/7,
k = 0, 1, 2, 3, 4, 5…….,
p_s is the number of stator pole pairs,

p_r is the number of rotor pole pairs,
n is the summation index, which is not even for a cosine expansion like the one in Equation (9),
Ω is the rotational speed of the rotor, radians/second.

The value of J_n is

$$J_n = \frac{2N_s I_{pk}}{\pi R_s} k_{wm} \quad , \tag{49}$$

where

N_s is the number of turns in series per phase,
I_{pk} is the peak phase current,
R_s is the radius of the current sheet,
k_{wn} is the n^{th} winding factor.

The expression for the n^{th} winding factor is

$$k_{wn} = \frac{\left| 1 - \exp^{j\frac{2\pi n}{Nsphase}} \right|}{2} \quad , \tag{50}$$

where N_{sphase} is the number of slots per phase.

Table 6 presents the magnet losses calculated by the MatLab program listed in Table 7. Table 8 is a presentation of output from the SPEED calculation for the 36-slot, 30-pole motor delivering 30 kW at 2000 rpm. Table 9 is a presentation of output from the SPEED calculation for the same motor delivering 55 kW at 10,000 rpm.

Summary of Design Analysis

In summary, the 55-kW design has been compared for two design methodologies and all differences have been resolved leading to a viable design for an HEV traction drive motor. The 55-kW motor was designed with 30 poles according to the developed design process. With this knowledge, there is mounting evidence that FSCW motors with low pole and slot count can be feasible in some cases and are worthy of further investigation.

Table 6. Magnet losses for a 36-slot, 30-pole 55-kw FSCW-SPM motor

Angular speed, rpm	Loss from Atallah equations[10] used by UWM, W	Loss calculated by Popescu at SPEED Consortium scaled by current ratio, W
2000	256	898
1018	1018	
2291	2291	
4073	4073	
6364	6364	1693

Table 7. MatLab program to calculate magnet losses

```
%Calculating Magnet Losses in case of SPM machines equipped with concentrated windings
clear all
close all
clc
m=-1; %m=1 in case of 2/7 S/P/Ph  %m=-1 in case of 2/5 S/P/Ph
q=3;  %Number of phases
Ps=3; %Number of stator pole pairs
Pr=15;      %Number of rotor pole pairs
Mu_0=4*pi*10^(-7);
Rho_mg=1.5*10^(-6);    %Resistivity of the magnet material sintered magnets, Ω-m
%Rho_mg=20*10^(-6);    %Resistivity of the magnet material bonded magnets, Ω-m
Alpha_p=0.95; %Ratio of magnet span to pole pitch
N_segments=1; %Number of magnet segments/pole
Alpha=2*pi*Alpha_p/(2*Pr*N_segments);
% Rs=0.1031;  %Stator outer radius
% Rr=0.0993;  %Rotor outer radius
% Rm=0.1025;  %Magnet outer radius
Rs=0.1346;  %Stator outer radius
Rr=0.0921;  %Rotor outer radius
Rm=0.0996;  %Magnet outer radius
n=1;   %Space harmonic order
Ns=30;  %Number of series turns per phase
Irms=180;
Im=Irms*sqrt(2);  %Peak phase current
Kwn=abs(1-1*exp(sqrt(-1)*150*(n/5)*pi/180))/2;
Jn=(2*Ns*Im/(1*pi*Rs))*Kwn;
speed=2*pi*10000/60; %Rotor speeed in rad/sec
leff=0.0678; % Machine active length [m]
if n*Ps==1
    Fn=log(Rm/Rr);
else
    Fn=((Rm/Rr)^(-2*n*Ps+2)-1)/(-2*n*Ps+2);
end
Pcn=((q^2*Mu_0^2*Alpha/(8*Rho_mg))*(Jn^2/(n^2*Ps^2))*(n*Ps-m*Pr)^2*speed^2*...
    ((Rm/Rs)^(2*n*Ps)*((Rs^2*Rm^2)/(2*n*Ps+2))*(1-(Rr/Rm)^(2*n*Ps+2))...
    +((Rr/Rs)^(2*n*Ps))*Rs^2*Rr^2*Fn+((Rr/Rs)^(2*n*Ps))*Rs^2*(Rm^2-Rr^2)))...
    /(1-((Rr/Rs)^(2*n*Ps)))^2;
if n*Ps==2
    Gn=log(Rm/Rr);
else
    Gn=((Rm/Rr)^(-1*n*Ps+2)-1)/(-1*n*Ps+2);
end
Pan=(-q^2*Mu_0^2/(Alpha*Rho_mg))*(Jn^2/(n^4*Ps^4))*(n*Ps+m*Pr)^2*speed^2*...
    (((Rm/Rs)^(n*Ps))*(Rs*Rm^2/(n*Ps+2))*(1-((Rr/Rm)^(n*Ps+2)))...
    +((Rr/Rs)^(n*Ps))*Rs*Rr^2*Gn)^2 ...
    *(sin(n*Ps*Alpha/2))^2/((Rm^2-Rr^2)*(1-(Rr/Rs)^(2*n*Ps))^2);
P=(Pcn+Pan)*leff
P_magnet=P*N_segments*2*Pr
```

Table 8. SPEED design sheets for FSCW-SPM motor delivering 30 kW at 2000 rpm

```
PC-BDC 6.5 for Windows (6.5.2.8) 9/15/2006 3:58:41 PM
c:\program files\speed\magnet dbm\5turn_36slot_30_polemotor_mp.bd4
UT-Battelle LLC
PC-BDC main title
PC-BDC sub-title

1 Dimensions:-------------------------------------------------------------

RotType    SurfRad         Embed          Not         Poles          30
Stator..
StatorOD   269.200 mm      LamShape    Circle         Slots          36
SYoke       11.000 mm      ASD         22.500 mm      SP           1.200
Rad3       134.600 mm      Rad2       123.600 mm      S-Slot      Square
TWS          9.000 mm      SD          22.500 mm      SO           4.800 mm
TGD          2.000 mm      SOang        1.000 mDeg    Stf          0.970
Rotor..
MOH          0.000 mm      Nmbp            5          Skew         0.000
RotorOD    199.200 mm      Rad1        99.600 mm      Gap          1.500 mm
LM           7.500 mm      BetaM      162.000 eDeg    pupa         0.900
RYoke       10.000 mm                                 RadSH       82.100 mm
DHub       184.200 mm      wNeck        0.386 mm
MEdge        7.500 mm      LM_min       7.500 mm
wMag         3.755 mm
Lstk        67.800 mm      Lrotor      67.800 mm      Lstator     76.800 mm

2 Magnet Data:------------------------------------------------------------

Magnet   SHIN-ETSU N42SH-nd-fe-Br Magnet
Br           1.000 T       Hc         955.000 kA/m    MuRec        1.050
CBr         -0.100 %/DegC  CHc         -0.540 %/DegC  DMag      7600.000 kg/m3
BrT          1.004 T       HcT        975.628 kA/m
Nuisance     0.000 mm      BrTnu        1.004 T       MuRecnu      1.050

3 Control Data:-----------------------------------------------------------

RPM       2000.000 rpm     Vs         292.500 V       Drive         Sine
ISP        255.500 A       gamma        0.000 deg     Sw_Ctl      ISP_HB
HBA_act    ISP/300         HB%          0.333         HBtype    Constant
FixfChop        No         fChop        0.000 kHz     fChopAct   598.000 kHz
EMFCalc        BLV         dq0          false
Vq           0.000 V       Rq           0.000 ohm     Vd           0.600 V
t_q          0.000 us                                 Freq1      500.000 Hz
ISP_Act    255.500 A       Tol_Act     ISP/20         ISLA_Act     1/128

4 Winding Data:-----------------------------------------------------------

Connex         Wye
WdgType     Custom
Offset            8        CPP          0.200
Tph          30.000         PPATHS           1         SPP          0.400
Layers        1.000         CSidesPh        12         Z          180.000
MLT         187.393 mm      LgthOEnd    84.286 mm      Ext          0.000 mm
EndFill       0.500         LaxPack     87.399 mm      Liner        0.200 mm
WireSpec  AWGTable          Gauge           19
NSH              47         WireDia      0.912 mm      InsThick     0.000 mm
SFg           0.695         SFn          1.093         MaxSFn       1.093
Aslot       220.890 mm^2    ASlotLL    208.410 mm^2    ACond       30.693 mm^2
```

Table 8. SPEED design sheets for FSCW-SPM motor delivering 30 kW at 2000 rpm (continued)

GPAslot	230.490	mm^2	ATstick	0.253	mm^2	TopStick	false	
TwjWid	2.000	mm	TwjLeg	3.500	mm	TwjThk	0.000	mm
PhsWid	2.000	mm	PhsLeg	3.500	mm	PhsThk	0.000	mm
ATwj	0.000	mm^2	APhs	0.000	mm^2			
XET	1.000		ETCalc	BDC 6.0		Rext	0.000	ohm
Nse	36.896		X_R	1.000		Ax1	15.000	mDeg
T_Wdg	100.000	DegC	Rph0	4.150E-03	ohm	R_LL	8.301E-03	ohm
T_c	20.000	DegC	Rph	3.158E-03	ohm/ph	TFRho	1.000	
Inductances...								
Lph	0.073	mH	Mph	0.000	mH	XL	1.000	
Lg	0.029	mH	LSlot	0.040	mH	Lendt	4.449E-03	mH
Mg	0.000	mH	MSlot	0.000	mH	LDiff	0.024	mH
Lsigma	0.068	mH	Msigma	2.639E-03	mH	XLdiff	1.000	
Lgg	0.133	mH	Mgg	0.000	mH	PCSlot	1.551	
LL_d	0.147	mH	LL_q	0.147	mH	L_LL	0.147	mH
Lg_0	5.279E-03	mH	Lg_2	2.059E-05	mH	Laa_d	0.073	mH
Ld	0.073	mH	Lq	0.073	mH	Laa_q	0.073	mH
Xd	0.230	ohm/ph	Xq	0.230	ohm/ph	Xsigma	0.205	
ohm/ph								
XCd	1.000		XCq	1.000		Lext	0.000	mH
Gd	0.177		Gq	0.176		XLendt	1.000	
kw1	0.966		Xm0	0.141	ohm/ph			
ks1	1.000		kp1	1.000		kd1	1.000	
ksg	0.182		fz	1.133		PSSlot	S-Closed	
Saliency	Auto		CalcLdLq	Auto		muPlug	1.000	
i1_Ang	2.023	A	i2_Ang	-222.394	A	i3_Ang	220.371	A

5 Magnetic Circuit Design:----------

T_Mag	100.000	DegC	T_r	16.000	DegC	XBrT	1.000	
BrT	1.004	T	BgOC	0.898	T	Hca	760.912	kA/m
BgAvOC	0.676	T	PhiG	0.964	mWb	BgA/BgOC	0.753	
Bg1OC	0.964	T	PhiM1	0.874	mWb	Bg1/BgOC	1.073	
BmOC	0.828	T	Bm/BrT	0.825		XBtpk	1.000	
HmOC	-133.421	kA/m	Hm/HcT	-0.137		PC	4.938	
Bst	1.474	T	Bsy	0.666	T	Bry	0.711	T
XTw	0.000		XSYoke	0.000		XRYoke	0.000	
kT	0.570	Nm/A	kE	0.641	Vs/Rad	krpmNL	4.679	krpm
kSat	1.000		XSatn	1.000		CalcSatn	Fixed	
SatnTol	0.000							
Xks	0.000		ks	0.000		XTTarc	1.000	
EffWst	9.000	mm	EffLst	20.410	mm	ukCL	0.000	
XBgap	1.000		X_EMF	1.000		k_rpf	1.000	
Btpk_OC	1.508	T	Btpk_Ld	1.541	T	Btpk_LdS	1.541	T
Bypk_OC	0.661	T	Bypk_Ld	0.961	T	Bypk_LdS	0.961	T
eLLpk	134.285	V	eTmax	2.277	V	Bslot	4.879E-03	T
IBk	2853.421	A	Bk	0.000	T	Hk	-760.912	kA/m
ILR	46315.717	A	BmLR	-15.255	T	HmLR	-1.23E+04	kA/m
IC180	67578.987	A	BmC180	-22.718	T	HmC180	-1.80E+04	kA/m
BHmag	110.467	kJ/m3	Carter	1.027		Xrm	0.500	
Amhp	612.481	mm^2	Aghp	641.236	mm^2	Rghp	1.912E+06	At/Wb
Pm0	0.108	uWb/At	Xrl	1.000		prl	0.256	
apEnd	1.000		Pend	0.000		Lme	7.500	mm
u_LKG	0.000		f_Lkg	0.950		if_Lkg	1.053	
Fringing	ON		XFringe	1.000		XBetaM	1.000	
SlotMod	No		XSlotMod	1.000				

Table 8. SPEED design sheets for FSCW-SPM motor delivering 30 kW at 2000 rpm (continued)

```
7 Dynamic design (time-stepping simulation):---------------------------------

OpMode     Motoring          Vs          292.500 V       RPM        2000.000 rpm
Tshaft      143.249 Nm       Pshaft    30001.993 W       Eff          97.384 %
WCu         309.103 W        WFe         256.306 W       WWF           0.000 W
WCan          0.000 W        WMagnet     240.576 W       WShaft        0.000 W
WTotal      805.984 W        TempRise      0.000 DegC    Jrms          5.885
A/mm^2
IWpk        255.948 A        IWav        162.624 A       IWrms       180.637 A
ILpk        255.948 A        ILav        162.623 A       ILrms       180.637 A
IQchpk      255.951 A        IQchav       58.267 A       IQchrm      108.823 A
IQcmpk      255.951 A        IQcmav       58.267 A       IQcmrm      108.823 A
IDchpk      255.927 A        IDchav       23.050 A       IDchrm       66.884 A
IDcmpk      255.927 A        IDcmav       23.050 A       IDcmrm       66.884 A
IDC_W       105.652 A        WConv        82.979 W       EffDCSh      97.122 %
IDC_P       105.610 A        WSwitch       0.000 W       Pelec     30807.978 W
Tgap        145.621 Nm       Tei         145.622 Nm      Trel          -0.001 Nm
Tloop       145.617 Nm       WFeCalc          OC         CalcVwfm       None
V1rms         0.000 V        I1rms       180.635 A       phi_1        -0.739 deg
phV1         90.000 deg      phI1         90.739 deg     phEq1        90.247 deg
V1d           0.000 V        I1d          -2.329 A
V1q           0.000 V        I1q         180.651 A

8 Steady-State Thermal Model:-----------------------------------------------

TempCalc      DegCW          FixTMag       IterX         Ambient      20.000 DegC
DegCW         0.000 degC/W   HTCcyl        0.000 W/m2/C  HTCend        0.000
W/m2/C
TempRise      0.000 DegC     T_c          20.000 DegC    T_r          16.000 DegC
T_f          20.000 DegC     T_y          20.000 DegC    HeatFlux      3.980
kW/m^2
SlotPeri     57.597 mm       Liner         0.200 mm      ct_Liner      0.200 W/mC
SSArea     3905.110 mm^2     C_motor      17.751 kJ/C    ThRSlot   7.113E-03 C/W
FSArea    2.025E+05 mm^2     ThermTC       0.000 min     R_fa          0.000 C/W

9 Miscellaneous:------------------------------------------------------------

Weights...
wt_Cu         4.602 kg       wt_Fe        11.154 kg      wt_Mag        2.095 kg
wt_Tot       17.851 kg       wt_Shaft     13.310 kg      wt_Frame      2.880 kg
wt_FeS        8.313 kg       wt_FeR        2.841 kg      wt_RSS       18.496 kg
Inertia components...
RotJ          0.086 kg-m2    RotJSS        0.088 kg-m2   RotJSh        0.045 kg-m2
RotJFe        0.022 kg-m2    RotJMag       0.019 kg-m2   LShaft       80.000 mm
sigma         4.997 psi
Wf0           0.000 W        RPM0       1000.000 rpm     NWFT          1.000
Fringing         ON          XFringe       1.000         NHx             21
CanStyle       None
Ecc           0.000          UMPavg    -6.11E-15 kg      UMPmax    -4.31E-15 kg
TRFrms       21.667 kg       TRFavg       17.038 kg      TRFmax       37.738 kg
CForce       29.935 kg                                   LamThk        0.500 mm
NLams          132           pcLam         3.000 %       RFei      1.000E+06

10 Core loss analysis:------------------------------------------------------
-

WFeCalc          OC          LossFE         Mech          XFe           1.000
```

Table 8. SPEED design sheets for FSCW-SPM motor delivering 30 kW at 2000 rpm (continued)

```
DFekgS    7656.829 kg/m^3  St.Steel Arnon 7  3.25% Si
DFekgR    7656.829 kg/m^3  Ro.Steel Arnon 7  3.25% Si
DFekgSh   7857.007 kg/m^3  Sh.Steel Low Carbon Steel 26g
wt_Teeth     3.820 kg      wt_Yoke      4.493 kg      wt_Troot     0.897 kg
Specific core losses...
cFe_E50      0.192 W/kg    cFe_H50      3.176 W/kg    cFe_50       3.368 W/kg
cFe_E_F     19.182 W/kg    cFe_H_F     31.758 W/kg    cFe_F       50.941 W/kg
cFe_T_E     17.299 W/kg    cFe_T_H     29.856 W/kg    cFe_T       47.155 W/kg
cFe_Y_E      3.405 W/kg    cFe_Y_H      4.134 W/kg    cFe_Y        7.539 W/kg
Core loss analysis...
WFe_T_E     81.600 W       WFe_T_H    140.832 W       WFe_T      222.432 W
WFe_Y_E     15.299 W       WFe_Y_H     18.574 W       WFe_Y       33.873 W


End of Design sheet-------------------------------------------------------
-
```

Table 9. SPEED design sheets for FSCW-SPM motor delivering 55 kW at 10,000 rpm

```
PC-BDC 6.5 for Windows (6.5.2.8) 9/29/2006 10:41:46 AM
c:\program files\speed\magnet dbm\5turn_36slot_30_polemotor_mp.bd4
UT-Battelle LLC
PC-BDC main title
PC-BDC sub-title

1 Dimensions:-------------------------------------------------------------
RotType    SurfRad         Embed          Not         Poles          30
Stator..
StatorOD   269.200 mm      LamShape    Circle         Slots          36
SYoke       11.000 mm      ASD         22.500 mm      SP           1.200
Rad3       134.600 mm      Rad2       123.600 mm      S-Slot      Square
TWS          9.000 mm      SD          22.500 mm      SO           4.800 mm
TGD          2.000 mm      SOang        1.000 mDeg    Stf          0.970
Rotor..
MOH          0.000 mm      Nmbp            5          Skew         0.000
RotorOD    199.200 mm      Rad1        99.600 mm      Gap          1.500 mm
LM           7.500 mm      BetaM      162.000 eDeg    pupa         0.900
RYoke       10.000 mm                                 RadSH       82.100 mm
DHub       184.200 mm      wNeck        0.386 mm
MEdge        7.500 mm      LM_min       7.500 mm
wMag         3.755 mm
Lstk        67.800 mm      Lrotor      67.800 mm      Lstator     76.800 mm

2 Magnet Data:------------------------------------------------------------
Magnet   SHIN-ETSU N42SH-nd-fe-Br Magnet
Br           1.000 T       Hc         955.000 kA/m    MuRec        1.050
CBr         -0.100 %/DegC  CHc         -0.540 %/DegC  DMag      7600.000 kg/m3
BrT          0.920 T       HcT        542.440 kA/m
Nuisance     0.000 mm      BrTnu        0.920 T       MuRecnu      1.050

3 Control Data:-----------------------------------------------------------

RPM      10000.000 rpm     Vs         292.500 V       Drive         Sine
ISP        325.000 A       gamma       77.500 deg     Sw_Ctl      ISP_HB
HBA_act    ISP/300         HB%          0.333         HBtype    Constant
FixfChop       No          fChop        0.000 kHz     fChopAct     0.000 kHz
EMFCalc        BLV         dq0          false
```

Table 9. SPEED design sheets for FSCW-SPM motor delivering 55 kW at 10,000 rpm (continued)

Vq	0.000	V	Rq	0.000	ohm	Vd	0.600	V	
t_q	0.000	us				Freq1	2500.000	Hz	
ISP_Act	325.000	A	Tol_Act	ISP/20		ISLA_Act	1/128		
4 Winding Data:----------									
Connex	Wye								
WdgType	Custom								
Offset	8		CPP	0.200					
Tph	30.000		PPATHS	1		SPP	0.400		
Layers	1.000		CSidesPh	12		Z	180.000		
MLT	187.393	mm	LgthOEnd	84.286	mm	Ext	0.000	mm	
EndFill	0.500		LaxPack	87.399	mm	Liner	0.200	mm	
WireSpec	AWGTable		Gauge	19					
NSH	47		WireDia	0.912	mm	InsThick	0.000	mm	
SFg	0.695		SFn	1.093		MaxSFn	1.093		
Aslot	220.890	mm^2	ASlotLL	208.410	mm^2	ACond	30.693	mm^2	
GPAslot	230.490	mm^2	ATstick	0.253	mm^2	TopStick	false		
TwjWid	2.000	mm	TwjLeg	3.500	mm	TwjThk	0.000	mm	
PhsWid	2.000	mm	PhsLeg	3.500	mm	PhsThk	0.000	mm	
ATwj	0.000	mm^2	APhs	0.000	mm^2				
XET	1.000		ETCalc	BDC 6.0		Rext	0.000	ohm	
Nse	36.896		X_R	1.000		Ax1	15.000	mDeg	
T_Wdg	100.000	DegC	Rph0	4.150E-03	ohm	R_LL	8.301E-03	ohm	
T_c	100.000	DegC	Rph	4.150E-03	ohm/ph	TFRho	1.314		
Inductances...									
Lph	0.073	mH	Mph	0.000	mH	XL	1.000		
Lg	0.029	mH	LSlot	0.040	mH	Lendt	4.449E-03	mH	
Mg	0.000	mH	MSlot	0.000	mH	LDiff	0.024	mH	
Lsigma	0.068	mH	Msigma	2.639E-03	mH	XLdiff	1.000		
Lgg	0.133	mH	Mgg	0.000	mH	PCSlot	1.551		
LL_d	0.147	mH	LL_q	0.147	mH	L_LL	0.147	mH	
Lg_0	5.279E-03	mH	Lg_2	2.059E-05	mH	Laa_d	0.073	mH	
Ld	0.073	mH	Lq	0.073	mH	Laa_q	0.073	mH	
Xd	1.152	ohm/ph	Xq	1.151	ohm/ph	Xsigma	1.027	ohm/ph	
XCd	1.000		XCq	1.000		Lext	0.000	mH	
Gd	0.177		Gq	0.176		XLendt	1.000		
kw1	0.966		Xm0	0.704	ohm/ph				
ks1	1.000		kp1	1.000		kd1	1.000		
ksg	0.182		fz	1.133		PSSlot	S-Closed		
Saliency	Auto		CalcLdLq	Auto		muPlug	1.000		
i1_Ang	-174.622	A	i2_Ang	324.691	A	i3_Ang	-150.068	A	
5 Magnetic Circuit Design:----------									
T_Mag	100.000	DegC	T_r	100.000	DegC	XBrT	1.000		
BrT	0.920	T	BgOC	0.829	T	Hca	697.250	kA/m	
BgAvOC	0.624	T	PhiG	0.889	mWb	BgA/BgOC	0.753		
Bg1OC	0.890	T	PhiM1	0.807	mWb	Bg1/BgOC	1.073		
BmOC	0.764	T	Bm/BrT	0.831		XBtpk	1.000		
HmOC	-117.999	kA/m	Hm/HcT	-0.218		PC	5.154		
Bst	1.361	T	Bsy	0.615	T	Bry	0.656	T	
XTw	0.000		XSYoke	0.000		XRYoke	0.000		
kT	0.526	Nm/A	kE	0.592	Vs/Rad	krpmNL	5.069	krpm	
kSat	1.000		XSatn	1.000		CalcSatn	Fixed		
Xks	0.000		ks	0.000		XTTarc	1.000		
EffWst	9.000	mm	EffLst	20.410	mm	ukCL	0.000		
XBgap	1.000		X_EMF	1.000		k_rpf	1.000		
eLLpk	619.807	V	eTmax	10.508	V	Bslot	2.052E-03	T	

Table 9. SPEED design sheets for FSCW-SPM motor delivering 55 kW at 10,000 rpm (continued)

IBk	2614.688	A	Bk	0.000	T	Hk	-697.250	kA/m
ILR	35237.155	A	BmLR	-11.450	T	HmLR	-9375.134	kA/m
IC180	1.099E+05	A	BmC180	-37.658	T	HmC180	-2.92E+04	kA/m
BHmag	90.187	kJ/m3	Carter	1.027		Xrm	0.500	
Amhp	612.481	mm^2	Aghp	641.236	mm^2	Rghp	1.912E+06	At/Wb
Pm0	0.108	uWb/At	Xrl	1.000		prl	0.256	
apEnd	1.000		Pend	0.000		Lme	7.500	mm
u_LKG	0.000		f_Lkg	0.950		if_Lkg	1.053	
Fringing	ON		XFringe	1.000		XBetaM	1.000	

6 Sine-wave static design [phasor diagram]:----------

OpMode	Motoring		Vs	292.500	V	RPM	10000.000	rpm
Tshaft	28.683	Nm	Pshaft	30036.330	W	Eff	76.255	%
WCu	657.587	W	WFe	2681.160	W	WWF	0.000	W
WCan	0.000	W	WMagnet	6014.394	W			
WTotal	9353.141	W	TempRise	80.000	DegC	Jrms	7.487	A/mm^2
IWpk	325.000	A	IWav	206.900	A	IWrms	229.810	A
ILpk	325.000	A	ILav	206.900	A	ILrms	229.810	A
IDC_P	134.665	A	WFeCalc	OC		Pelec	39389.470	W
Eq1	259.780	V	Vph1	58.190	V	VLL1	100.788	V
Iq1	49.740	A	Id1	-224.362	A	gamma	77.500	deg
Vq1	1.589	V	Vd1	-58.168	V	delta	88.435	eDeg
Bg1Load	0.794	T	phi	10.935	eDeg	PF	0.982	
Bqad	0.000	T	Phida1	-0.087	mWb	Phiqa1	0.019	mWb
BmLoad	0.679	T	Bma	-0.085	T	Fda1	-585.342	At/gap
Tgap_PS	36.986	Nm	TEI_PS	37.017		Trel_PS	-0.031	Nm
Tgap	36.986	Nm	Tei	37.017	Nm	Trel	-0.031	Nm
Tloop	36.986	Nm						
Available voltage...								
Vs120	197.507	Vrms	Vs1	228.061	Vrms	Vs1Lin	179.119	Vrms

8 Steady-State Thermal Model:----------

TempCalc	DegCW		FixTMag	IterX		Ambient	20.000	DegC
DegCW	0.000	degC/W	HTCcyl	0.000	W/m2/C	HTCend	0.000	W/m2/C
TempRise	80.000	DegC	T_c	100.000	DegC	T_r	100.000	DegC
T_f	100.000	DegC	T_y	100.000	DegC	HeatFlux	0.000	kW/m^2
SlotPeri	57.597	mm	Liner	0.200	mm	ct_Liner	0.200	W/mC
SSArea	3905.110	mm^2	C_motor	17.751	kJ/C	ThRSlot	7.113E-03	C/W
FSArea	2.025E+05	mm^2						

9 Miscellaneous:----------

Weights...								
wt_Cu	4.602	kg	wt_Fe	11.154	kg	wt_Mag	2.095	kg
wt_Tot	17.851	kg	wt_Shaft	13.310	kg	wt_Frame	2.880	kg
wt_FeS	8.313	kg	wt_FeR	2.841	kg	wt_RSS	18.496	kg
Inertia components...								
RotJ	0.086	kg-m2	RotJSS	0.088	kg-m2	RotJSh	0.045	kg-m2
RotJFe	0.022	kg-m2	RotJMag	0.019	kg-m2	LShaft	80.000	mm
sigma	1.269	psi						
Wf0	0.000	W	RPM0	1000.000	rpm	NWFT	1.000	
Fringing	ON		XFringe	1.000		NHx	21	
CanStyle	None							
Ecc	0.000		UMPavg	-9.64E-16	kg	UMPmax	1.166E-14	kg
TRFrms	18.464	kg	TRFavg	14.519	kg	TRFmax	32.158	kg
CForce	748.387	kg				LamThk	0.500	mm
NLams	132		pcLam	3.000	%	RFei	1.000E+06	

Table 9. SPEED design sheets for FSCW-SPM motor delivering 55 kW at 10,000 rpm (continued)

```
10 Core loss analysis:-----------------------------------------------------------
WFeCalc         OC          LossFE         Mech          XFe          1.000
DFekgS    7656.829 kg/m^3  St.Steel Arnon 7  3.25% Si
DFekgR    7656.829 kg/m^3  Ro.Steel Arnon 7  3.25% Si
DFekgSh   7857.007 kg/m^3  Sh.Steel Low Carbon Steel 26g
wt_Teeth     3.820 kg      wt_Yoke      4.493 kg      wt_Troot     0.897 kg
Specific core losses...
cFe_E50      0.192 W/kg    cFe_H50      3.176 W/kg    cFe_50       3.368 W/kg
cFe_E_F    479.560 W/kg    cFe_H_F    158.791 W/kg    cFe_F      638.350 W/kg
cFe_T_E    368.532 W/kg    cFe_T_H    113.605 W/kg    cFe_T      482.137 W/kg
cFe_Y_E     72.541 W/kg    cFe_Y_H     18.015 W/kg    cFe_Y       90.556 W/kg
Core loss analysis...
WFe_T_E   1738.393 W       WFe_T_H    535.885 W       WFe_T     2274.278 W
WFe_Y_E    325.937 W       WFe_Y_H     80.945 W       WFe_Y      406.882 W

End of Design sheet--------------------------------------------------------------
```

Differences between the results of UWM and SPEED have been resolved. Such differences, which concern magnet losses, are because of the skin effect at higher speeds and are essentially inductance limited at higher speeds. These results emphasize the necessity of circumferentially segmenting the magnets and do not detract from the results of El Refaie, Jahns, and McKeever.[8]

Speed Control of Fractional-Slot Concentrated Winding PM Motors

A wide and theoretically infinite CPSR can be achieved with a PM synchronous motor if the winding inductance is sufficiently large.[11–13] Recent work at UWM[6] has shown that winding inductance of FSCW-SPM machines can easily be made sufficiently large to achieve satisfactory CPSR performance. Electric/hybrid electric vehicles require not only wide CPSR operation but also high efficiency. While CPSR performance can be resolved through proper machine design using FSCW technology, the efficiency of traction drives can depend on how they are controlled. Of particular concern is the efficiency of the traction drive when operating at fractional load conditions. In the present work the effect of control on the efficiency of the overall drive system and on the efficiency of the motor alone is considered.

Introduction

At ORNL investigators have analyzed the requirements of a speed control scheme whose objective is to minimize the motor current magnitude at all operating conditions.[13] Below base speed, in the constant torque operating mode, a traction drive with this type of control maximizes the motor shaft torque (Nm) produced per amp of motor current. Above base speed in the constant power operating mode, this type of control maximizes the power (watts) per amp of motor current. During FY 2006 the ORNL team developed a closed-loop speed control for an FSCW machine which implements motor current magnitude minimization. A 6-kW, 30-pole, FSCW motor developed by UWM, FSCW-1, is to be tested using the closed-loop speed control system developed by ORNL and drive/motor efficiency will be determined experimentally. Details of the speed control and test setup and procedures are described below.

In companion work, investigators at UWM have shown that minimum motor current control does not necessarily ensure maximum motor efficiency.[14] Their work showed that, for a specific FSCW design, a blend of maximum torque per amp and maximum torque per volt control may improve overall motor efficiency by reducing motor core losses.[14] In the light load condition cited in the reference, the motor current magnitude for maximum motor efficiency was approximately three times larger than for the maximum torque per amp control at the same condition. The overall reduction in core losses was sufficient to overcome a ninefold increase in motor copper losses. Because loss mechanisms in the inverter are approximately linear in motor current magnitude, it is not clear whether the maximum motor

efficiency condition will also result in maximum overall system efficiency. The testing of the 6-kW FSCW prototype may be extended to study whether the minimum motor current control or minimum motor loss control has the best overall system efficiency. Further details of the UW maximum motor efficiency control concept are contained in the section entitled "Enhanced Partial Load Efficiency Control Algorithm."

Parameters of the 6-kW prototype FSCW motor

The 6-kW FSCW prototype was laboratory tested by ORNL to determine the values of key machine parameters and to characterize speed dependent zero current losses. The winding resistance, inductance, and fundamental back-emf constant are

$$\begin{aligned} R &= 0.075\,\Omega \text{ per phase} \\ \mathrm{L} &= 1.2 \text{ mH per phase} \\ \mathrm{K_v} &= 0.05494 \text{ volts per rpm} \\ &\quad (49.45 \text{ V rms at } 900 \text{ rpm}) \end{aligned} \tag{51}$$

The zero current speed sensitive losses are shown in Figure 14. The figure shows data points taken from dynamometer measurements and a least squares fit to the experimental data. Dynamometer measurements were taken only up to 4000 rpm, which is the highest speed at which the 6-kW prototype has been driven, but the least squares fit predicts losses of 1867 W at 6000 rpm. The ORNL model of motor losses includes only speed sensitive effects.

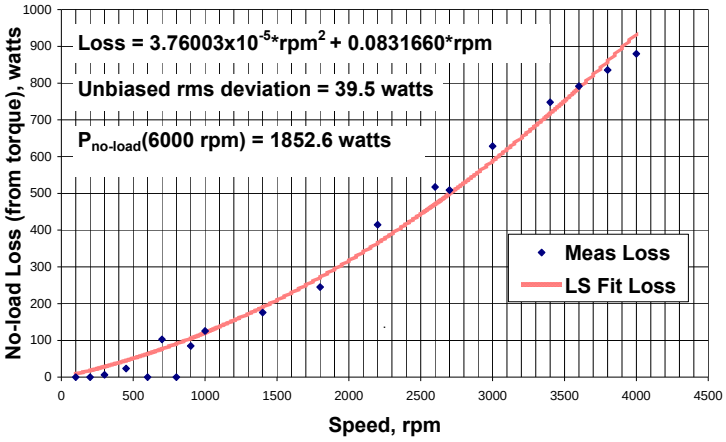

Figure 14. Zero current losses of the FSCW-1 prototype.

The prototype machine has 30 poles, a base speed of 900 rpm, and a rated output power of 6 kW. Let "subscript b," $_b$, denote "at base speed" and let n denote speed relative to base speed. Then the reactance of the winding inductance and magnitude of the back-emf at base speed and at any relative speed, n, are given by the following:

p = 30 poles,
N_b = 900 rpm,

N = speed in rpm,

$n = \dfrac{N}{N_b} =$ normalized speed,

Ω_b = 1413.7 electrical radians/second,

Xb = $\Omega_b L$ = 1.6965 Ohms reactance at base speed,

$X = nX_b$ reactance at relative speed, n, and

$E = nE_b$back—emf magnitude at relative speed, n.

Let "subscript capital R," $_R$, denote "rated" values so that rated useful average output power and rated rms motor current are

$$P_R = 6{,}000 \text{ W}$$

and

$$I_R = \frac{P_R}{3E_b} = 40.44 \text{ A rms} \tag{52}$$

The minimum dc supply voltage necessary to support rated power at base speed for this motor is given by

$$V_{dc-\min} = \pi\sqrt{\frac{\left(E_b + RI_R\right)^2 + \left(X_b I_R\right)^2}{2}} = 192 \text{ V} \quad . \tag{53}$$

Simplified Per-Phase Model

ORNL has used simplified per phase models with considerable success to study the performance of PM machine drives with either trapezoidal or sinusoidal back-emf wave shapes. The per-phase model represents only the fundamental frequency component response of the machine; consequently, some factors such as torque ripple cannot be studied while using this simplification. In general the fundamental frequency component dominates the motor current response and accurately preserves power. The main advantage of the simplified fundamental frequency model is that it eliminates the need for simulating the pulse-width modulation (PWM) switching actions. Although the effects of switching are not explicit in this model, it was recently extended to predict all of the inverter loss mechanisms.[13] The model is shown in Figure 15. This model was used extensively in the development of the closed-loop control schemes described below.

Closed-loop speed control system for FSCW PM traction motors

An objective in the development of the closed-loop speed control was to have low complexity and minimum use of sensors. The control structure selected is a proportional speed control (Figure 16). The speed command, labeled as "spdcom" in the figure, is processed through a simple gain, Ks in the figure, and the actual speed is subtracted to form a speed error. The speed error is multiplied by a gain, Ke in the figure, and the output is a desired rms motor current, Id. The desired current is processed through a saturation function whose upper limit is the specified rms current rating of the motor, I_R, and whose lower limit is zero because a negative rms value makes no physical sense. The output of the saturation function is the commanded rms current, I_{com}. This commanded current and the measured instantaneous shaft speed and position are all that are required in this controller to generate inverter commands. It is presumed that sinusoidal PWM control will be used to generate inverter switching commands;

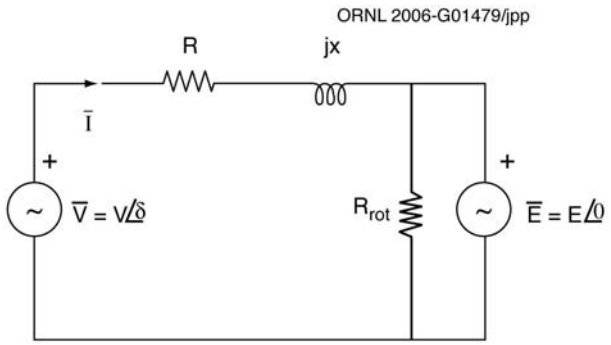

Figure 15. Fundamental frequency model of a permanent magnet motor driven by a pulse-width modulation controlled voltage source inverter.

consequently, the required control variables are the amplitude modulation index, denoted as M_a, and the inverter lead angle, δ . Values of M_a between 0 and 1 are referred to as the linear modulation region. In this region the rms value of the fundamental frequency component of the line-to-neutral voltage applied to the motor is given by

$$V_1 = \frac{M_a V_{dc}}{2\sqrt{2}} \text{ for } 0 \le M_a \le 1 \quad . \tag{54}$$

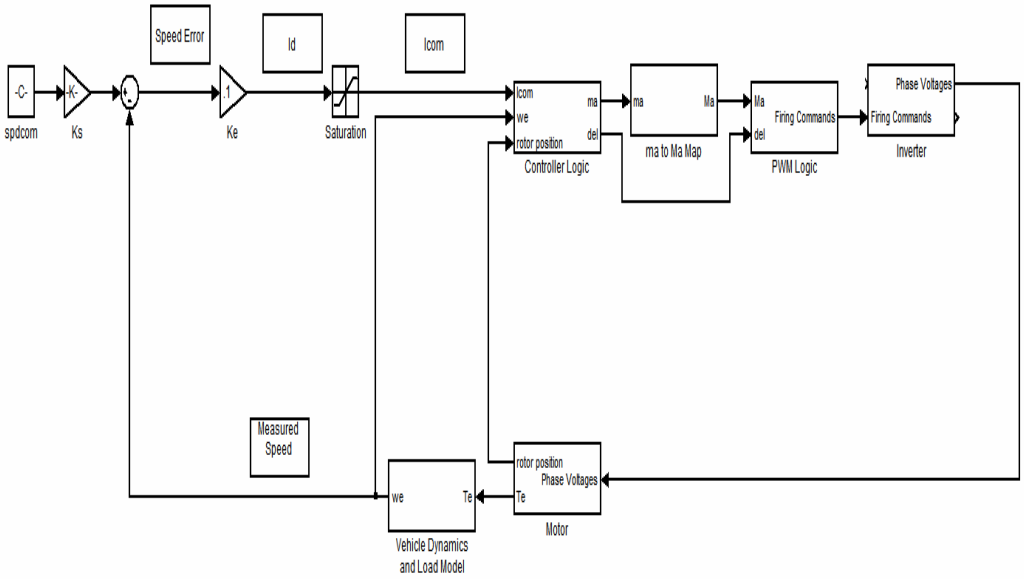

Figure 16. Closed-loop speed control block diagram.

Values of M_a greater than 1 are called the nonlinear modulation region, and in this region the high frequency switching of PWM degenerates towards six-step operation. The value of the rms fundamental

component increases with values of M_a greater than 1 but less than linearly, and in fact, once the PWM has degenerated to six-step switching, no further increase is observed in fundamental voltage. The fundamental voltage for a six-step waveform is the maximum possible value and is given by

$$V_{1-max} = \frac{\sqrt{2}V_{dc}}{\pi} \quad . \tag{55}$$

The controller logic block calculates a "pseudo amplitude modulation index," ma, which is the ratio of the rms fundamental voltage to the rms fundamental voltage at the end of linear modulation; that is

$$ma = \frac{V_1}{\frac{V_{dc}}{2\sqrt{2}}} = \frac{2\sqrt{2}V_1}{V_{dc}} \quad . \tag{56}$$

Values of ma lie between 0 and $\frac{4}{\pi}$. For a given ma, the value of the corresponding M_a is dependent on the frequency modulation index. The frequency modulation index is the ratio of the frequency of the triangular carrier wave of the PWM logic to fundamental frequency. Because the fundamental frequency of the motor increases with motor speed, the frequency modulation index is not constant unless the carrier frequency is varied in proportion to any change in motor speed. Generally the carrier frequency is not fixed but held constant at the highest switching frequency that can be tolerated by the inverter switches. A map of ma into M_a is shown in Figure 17 for a frequency modulation index of 39. The ma to M_a map in the control block diagram is implemented as a table lookup. If necessary, several maps can be stored for various values of frequency modulation index and interpolation can be used to account for changes in frequency modulation arising from changes in motor speed. Once amplitude modulation index, M_a, and lead angle, δ, are determined, the control function is complete, and the remaining components in the diagram would be the same as for any other PWM controlled drive and include the PWM switching logic to firing commands block, the inverter, the motor, and the vehicle and load dynamics blocks.

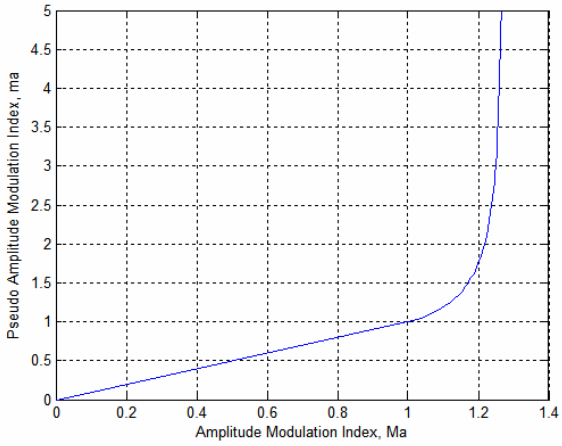

Figure 17. Amplitude modulation index versus pseudo amplitude modulation index for a frequency modulation index of 39.

Notice that current sensing is not used in this control. This does leave the performance of the controller vulnerable to variations in machine and drive parameters, especially the direct current supply voltage, the winding inductance, and the back-emf voltage constant. The direct current supply voltage is easily measured and consequently variation in V_{dc} is readily accounted for. Handling variations in the back-emf constant and winding inductance will be studied in the future. For the experiments at hand, the laboratory measurements of inductance and back-emf constant will suffice.

The core of the control strategy is contained in the Figure 16 block labeled "Controller Logic," which processes the current command, I_{com}; measured speed, we; and measured rotor position into the pseudo amplitude modulation index, ma, and the inverter lead angle, del, which appears as δ in the equations. Two variations of the controller logic block are discussed below.

Rated Current Limiting Controller Logic

The specified rms current rating of the motor, , is not to be exceeded at any operating condition. PM machines with low speed and core losses may be able to develop more power in the constant power zone than at base speed without exceeding the rms current rating. For such machines, the onboard direct current supply may have to provide power in excess of its rating if the motor is allowed to approach rated current during operation above base speed. The controller logic can be adapted to preclude exceeding rated power as discussed in the section entitled "Rated Current and Rated Power Limiting Controller Logic." In this section the constraint is to limit motor current to be no greater than the rated value.

Consider operating at relative speed, n, at pseudo amplitude modulation index, ma, and inverter lead angle,. The linear model of Figure 15 has rms current

$$I = \frac{\sqrt{V^2 - 2nVE_b \cos\delta + n^2 E_b^2}}{Z} \quad . \tag{57}$$

where

$$V = \frac{maV_{dc}}{2\sqrt{2}}$$

and

$$\mathrm{Z} = \sqrt{\mathrm{R}^2 + \left(nE_b\right)^2}$$

If the rms current is to be no greater than the rated value, I_R, then the inverter lead angle must be limited to a value no larger than

$$\delta_{\max} = \cos^{-1}\left[\frac{V^2 + n^2E_b^2 - Z^2I_R^2}{2nVE_b}\right] \quad . \tag{58}$$

Maximum power transfer between the inverter and the motor occurs when the inverter lead angle is equal to β where

$$\beta = \tan^{-1}\left(\frac{nX_b}{R}\right) \quad . \tag{59}$$

If the value of δ_{max} exceeds the value of β, then more power can be produced at a lower current than the rated current. It isn't reasonable to maintain rated current if more power can be developed at a lower current level. As the objective of the control is to meet the load condition at the minimum current, the best value of δ_{max} is

$$\delta_{\max} = \min\left(\beta, \cos^{-1}\left[\frac{V^2 + n^2E_b^2 - Z^2I_R^2}{2nVE_b}\right]\right) \quad . \tag{60}$$

Rated current and rated power limiting controller logic

Above base speed a PM motor may be capable of developing more power than the rated value while operating below rated current. If it is desired to restrict developed power to a value no greater than rated, then the inverter lead angle must be restricted to a lower value than required for current limitation. At relative speed *n* (greater than one), such that the pseudo amplitude modulation index is at the maximum value of $\frac{4}{\pi}$ and the applied rms motor voltage at fundamental frequency is likewise at its maximum,

$$V_1 = V_{1-\max} = \frac{\sqrt{2}V_{dc}}{\pi} \quad . \tag{61}$$

Then the total developed power per phase, including useful load power and speed sensitive losses, is given by

$$\frac{P}{3} = \frac{nE_bV_1}{Z}\cos(\beta - \delta) - \frac{n^2E_b^2}{Z}\cos\beta \quad , \tag{62}$$

where

$$\beta = \tan^{-1}\left(\frac{nX_b}{R}\right).$$

To limit this power to be no greater than rated power, P_R, requires that the inverter lead angle be limited to

$$\delta_{\max} = \beta - \cos^{-1}\left(\frac{ZP_R/3 + n^2E_b^2\cos\beta}{nV_1E_b}\right) \quad . \tag{63}$$

Under some conditions, particularly low supply voltage, it may be necessary to restrict δ to be no larger than the value of β. In such cases, the rated power cannot be developed and having δ = β allows maximum possible power.

To avoid having the motor enter regeneration mode during coasting operation, such as when the vehicle is in motion but the speed command is temporarily reduced to zero, the value of lead angle, δ, must be larger than

$$\delta_{\min} = \beta - \cos^{-1}\left(\frac{ZP_{rot}(n) + n^2E_b^2}{nV_1E_b}\right) \quad . \tag{64}$$

This limit should also be applied in the rated current magnitude limiting logic described in the previous section.

Simulation of the closed-loop speed control

The speed control system described in the preceding section was simulated using the fundamental frequency model developed in previous work.[13] This eliminates the need to include the PWM switching logic and greatly decreases the simulation time required to investigate vehicle response to speed commands. Even though the details of PWM switching are suppressed, the model is still able to capture the inverter losses described in Lawler.[13]

Only the step response to large speed commands is considered here. One simulation is shown for the current limiting control logic and the same simulation is shown for the power limiting control logic. The simulations are done for standing start conditions, zero initial vehicle speed, and a step command to one-half full speed (or 3000 rpm). It is assumed that the vehicle load is quadratic in speed with the full 6-kW rated power required for 6000 rpm. The equivalent rotational inertia was selected so that the vehicle driven by the 6-kW prototype weighed approximately 500 kg. Although this is a very heavy vehicle for the size of the motor, the use of a large rotational moment of inertia will decrease the speed of response to speed commands and make the comparison of the rated current limiting control and the rated power limiting control clearer.

Figure 18 displays the response of motor revolutions per minute, commanded and root-mean-square motor current, and developed power to the step command from 0 rpm to 3000 rpm for both the rated current limiting logicl [Figure 18(a), (c), and (e)] and the rated current and rated power limiting logic [Figure 18(b), (d), and (f)]. Notice that in steady state both cases have a steady state error because of the

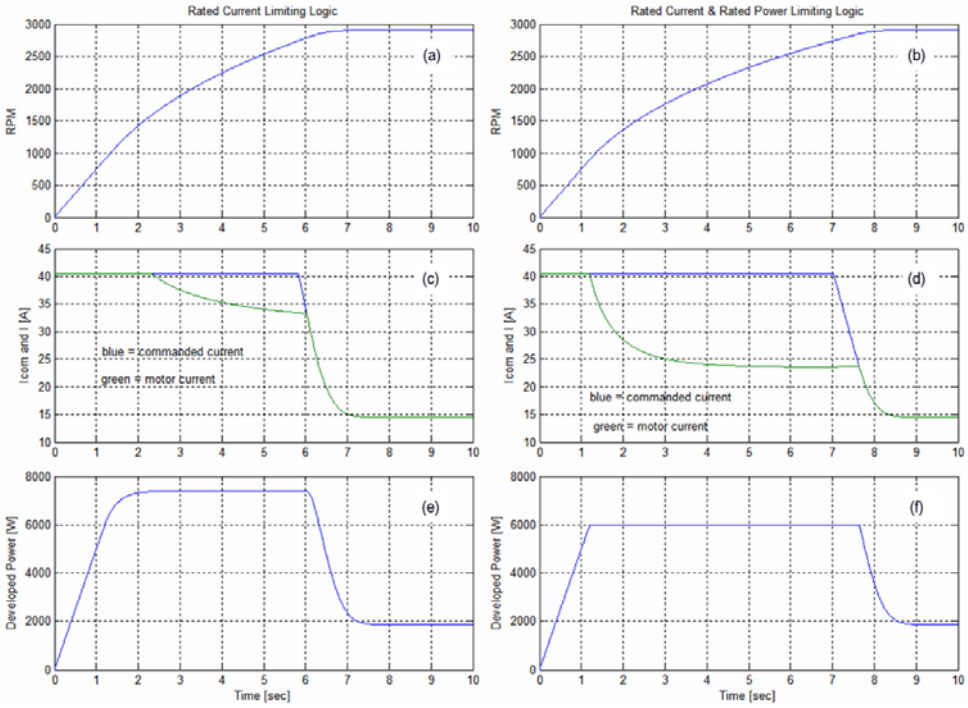

Figure 18. Rated current limiting control (left) and rated current plus rated power limiting control (right).

use of a simple proportional control. This error could be suppressed by increasing the proportional gain, Ks, of Figure 16 by adding an integrator to the controller or by the vehicle operator simply increasing the speed command slightly.

Notice that for the rated current limiting logic [Figure 18(a), (c), and (e)] the actual motor current begins decreasing at about 2.4 s despite the fact that the commanded current remains at the rated value. This is an instance where forcing the motor current to remain at rated power would result in less developed power. Figure 18(e) demonstrates that despite the reduction in current between 2.4 and 5.8 s, the developed power remains constant at 7400 W.

For the rated current and rated power limiting logic, the acceleration of the motor is slower than for the rated current limiting logic. This is because the developed power is limited to 6000 W, whereas, with only current limiting control, the developed power peaked at 7400 W. The current and power limited control took more than 8 s to reach steady state, whereas the current limiting control took less than 7 s. In the rated current and rated power limiting control, the motor current begins decreasing at 1.3 s and this decrease is associated with limiting the developed power to 6000 W.

The final steady state condition of the two cases is identical. The two methods will differ in response during transient conditions, but the steady states will be the same for any load condition that does not exceed rated power.

Conclusion

A simple proportional speed control has been developed for FSCW-SPM motors. Detailed simulation of the control shows that it can be effective in controlling motor speed while minimizing the motor current magnitude during operation above and below base speed. Laboratory testing of this method and the maximum motor efficiency control described below will allow comparisons to be made as to which method results in the greatest overall drive efficiency.

Iron Loss Model Development

As noted in the objectives, significant effort is being devoted to the development of closed-form analytical models of the iron losses in the FSCW-SPM machine. This section will summarize the nature of the analytical models and the progress that has been achieved towards verifying their accuracy.

Two FSCW-SPM machines designed to meet the FreedomCar advanced traction motor performance targets were proposed for use in analytical studies during FY 2006.[8] The first, named *SPM1*, exhibited a 900-V back-emf at top speed (10,000 rpm), which was above the 600-V target. *SPM1* has been used as the basis for comparisons between iron loss predictions of the closed-form analytical model and more detailed predictions from FEA. The second, named *SPM2*, exhibited a 600-V back-emf at top speed and had the best match between target values and performance estimates; consequently, it was chosen for the "Analysis and Design of Motors with Fractional-Slot Concentrated Windings" part of this study.

This 55-kW (peak) machine, *SPM1*, is used as an example for exploring the proposed analytical approach for calculating the iron losses. A cross-section of the basic repeating unit of this machine was shown in Figure 7, and some key machine dimensions and parameters are summarized in Table 10. More details about this machine can be found in El-Refaie, Jahns, and McKeever.[8]

The electromagnetic FEA programs MagNet2D (Infolytica) and JMag (JRI, Inc.) have been used to provide more accurate predictions of the magnetic fields and iron losses in the FSCW-SPM machine. In particular, the JMag program is capable of providing a point-by-point frequency spectrum calculation of the iron losses over the complete cross-section of the machine. Both hysteresis and eddy-current losses are calculated for *SPM1*, using iron loss characteristics provided by the lamination steel manufacturer. This approach provides the highest possible accuracy for predicting the iron losses in such a machine, but the calculations are very time-consuming.

Table 10. *SPM1* machine dimensions and parameters

Slots/pole/phase	2/5	Slots	36
Poles	30	Rotor outer radius [mm]	92.1
Stator OD [mm]	269	Active length [mm]	63.5
Total length [mm]	75.4	Magnet thickness [mm]	7.5
Air-gap thickness [mm]	1.5	Magnet remanent flux density [T]	1.0 @ 140°C
Copper mass [kg]	4.6	Magnet mass [kg]	2.0
Iron mass [kg]	9.7	Total mass [kg]	16.3

Open-Circuit Machine Model and Loss Predictions

SPM1, summarized in the preceding section, was analyzed to determine its magnetic flux density distribution and losses under open-circuit conditions. The major parts of the machine that contribute to the iron losses include

1. stator iron teeth and yoke,
2. rotor iron inner yoke, and
3. rotor magnets.

Under open-circuit conditions for which there is no stator excitation, the rotor losses are minimal[15] because the rotor back-iron that carries the magnet flux does not see much temporal change in flux density as the rotor moves.

Closed-form expressions for the magnetic flux density distribution under open-circuit conditions have been derived as a function of radius inside the air gap by solving the associated Laplace equations.[16,17] The accuracy of this technique depends on the assumption that magnetic saturation is not significant in the machine iron, an assumption that is typically quite reasonable for this type of machine. These equations determine the spatial harmonic components of the flux density distribution for a specified machine configuration. In particular, attention is paid to three different radii—the rotor iron outer radius (R_r+), the rotor magnet outer radius (R_m+), and stator inner radius (R_s-).

Figure 19(a) shows the predicted spatial distribution of the air-gap flux density at these three different radii inside the air gap for a slotted version of the *SPM1* machine. The harmonic spectrum for the flux density distribution at radius, R_s-, is shown in Figure 19(b). The effect of the slots is to introduce even harmonics into the distribution as well as lowering the amplitude of the fundamental component. More details about the analytical model including mathematical expressions have been included in a separate report.

The tooth flux density can be approximately calculated by assuming that the flux density[18] is uniform across the width of each tooth, *TW*, for all of its length, h_g, excluding the tooth tip. The resulting flux density in the tooth can then be approximately determined by integrating the flux density waveform over the tooth pitch and dividing by the tooth width, *TW*. Figure 20(a) shows the resulting tooth flux density distribution predicted using the approach described above as the rotor is rotated. Higher-order harmonic components are attenuated in the spatial flux density distribution so that the resulting waveform in Figure 20(a) is dominated by its fundamental component. The peak value of the tooth flux density, B_{th}, as the rotor rotates through a complete pole pitch is approximately 0.62 T for the *SPM1* machine.

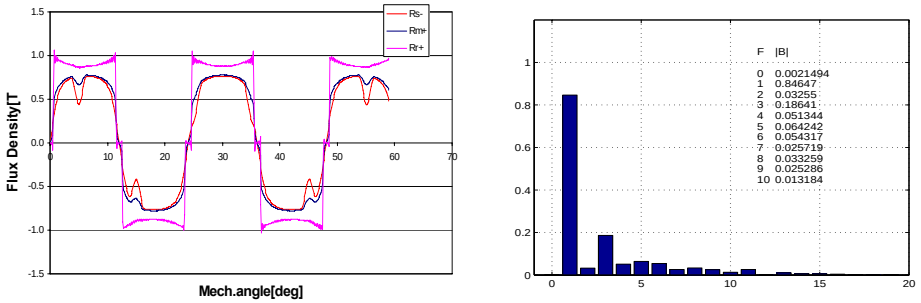

(a) Three different radii **(b) Harmonic spectrum at stator inner radius, R_s–**

Figure 19. Analytical predictions of the spatial air-gap flux density distribution for a slotted version of the *SPM1* machine for a rotor angular position of 5 mechanical degrees.

The same type of simplifying assumption made about the uniformity of the flux density across the tooth width can be extended to the stator yoke, for which it will be assumed that the flux density is the same everywhere in the cross-sectional area of the stator yoke behind each stator slot. Figure 20(b) shows the predicted yoke flux density distribution waveform as the rotor is rotated. As in the case of the tooth flux density waveform, the amplitudes of the harmonic components are significantly attenuated. The peak amplitude of the *SPM1* yoke flux density B_{ykn} as the rotor rotates through a complete pole pitch is determined to be approximately 1.32 T.

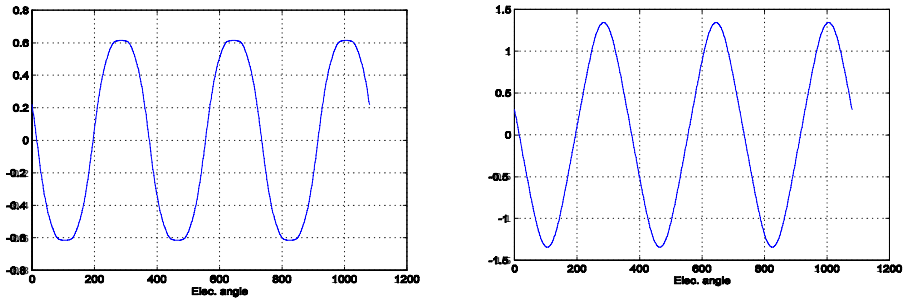

(a) Stator tooth **(b) Stator yoke**

Figure 20. Predicted flux density waveform in different parts of the stator based on the assumption of uniform tooth flux density.

Figure 21 provides a direct comparison of the predicted spatial flux density distributions at radius, R_s–, for the closed-form analytical model and FEA. The high-quality agreement between the two waveforms and their dominant frequency components indicates that the closed-form analytical approach can do an excellent job of predicting the air-gap flux density distributions for this type of SPM machine.

The stator iron core loss can be predicted using the stator tooth and yoke flux density waveforms that have been calculated using closed-form analysis based on the uniform flux density principle as described above. The analytical model for determining the stator core losses is based on summing the loss contributions of each of the dominant harmonic components in the frequency spectra for the tooth and yoke flux densities.

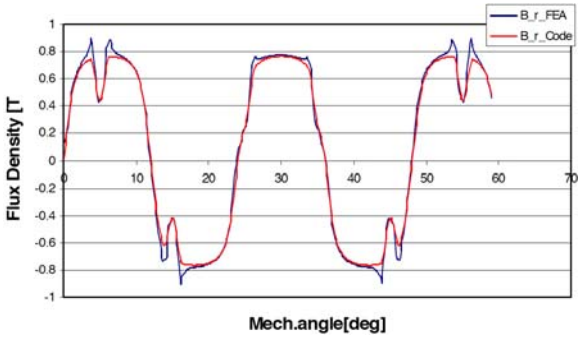

Figure 21. Comparison of predicted air gap magnetic flux density distribution at radius R_s– using closed-form (B_r_Code) and finite-element (B_r_FEA) analysis.

The familiar Steinmetz equation[9] for calculating the hysteresis loss associated with each of the frequency components in the flux density waveform is given by

$$P_{ht} = k_h B_{th}^{\beta} \omega_S \ [\mathrm{W/m^3}] \ . \tag{65}$$

The corresponding eddy current loss equation is given by

$$P_{et} = k_e B_{th}^{2} \omega_S^{2} \ [\mathrm{W/m^3}] \ . \tag{66}$$

Typical values have been adopted for the coefficients and exponents that appear in the above loss equations for grades of silicon iron laminations commonly used in small and medium induction motors. They are $k_h = 48$, $\beta = 2$, and $k_e = 0.055$.

Figure 22 provides a comparison of the predicted total iron losses in different parts of the machine using the closed-form analytical model and the more accurate point-by-point FEA technique described previously. There are several observations that can be made from this figure.

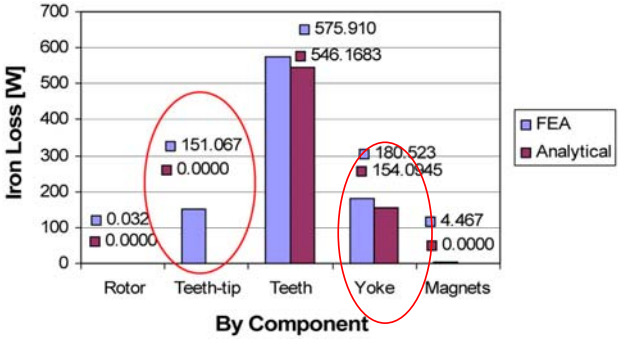

Figure 22. Comparison of predicted iron losses in different parts of the *SPM1* machine at 2000 rpm in an open-circuit condition using closed-form analysis and point-by-point finite-element analysis technique.

On the positive side, the agreement between the iron loss predictions, including both hysteresis and eddy current losses, for the closed-form analysis and point-by-point FEA is quite good, with the closed-form predictions approximately 5% and 14% below the FEA predictions for the teeth and yoke portions of the machine, respectively.

Figure 22 also highlights the fact that a technique for predicting the iron losses in the stator tooth tips along the inner stator bore has not yet been developed for the closed-form analysis, explaining why this bar is absent from the figure. The tooth tips are exposed to a richer harmonic mix of spatial flux density components than the rest of the teeth or yoke. These harmonics explain why the FEA predictions for the tooth-tip iron losses are nearly as high as for the yoke in the *SPM1* machine. As a result of these additional losses, which are not accounted for using the closed-form analysis, the total error between the predicted iron losses using the two techniques is approximately 23%. **This clearly identifies an area where further work is needed to improve the closed-form analytical model.**

Finally, the FEA-predicted iron loss results in Figure 22 confirm that the rotor magnet and iron yoke losses are very low in the *SPM1* machine for open-circuit conditions.

Armature Reaction Loss Predictions

The next major step in developing the iron loss model for the FSCW machine is to predict the iron losses associated with magnetic flux density components induced by the presence of current in the stator coils. This type of loss is called armature reaction loss. Progress has been made towards predicting these armature reaction iron losses using the point-by-point FEA technique.

Figure 23(a) shows the FEA-predicted iron losses in the *SPM1* machine, broken down by the major sections of the machine, when it is rotating at 2000 rpm with alternating current stator currents of 200 A.

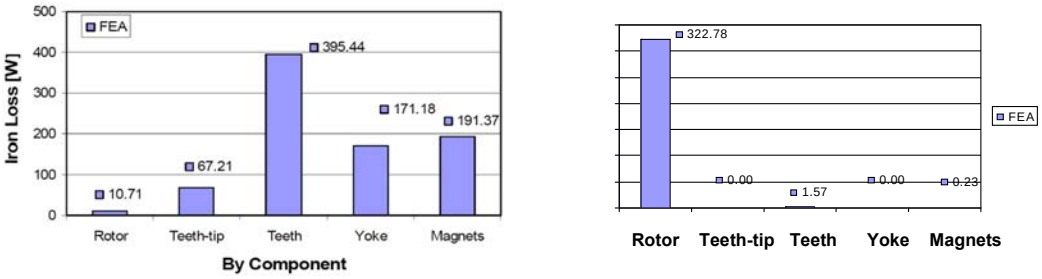

(a) Machine section breakdown **(b) Harmonic content in teeth**

Figure 23. Finite-element-analysis-predicted iron eddy current losses at 2000 rpm with a peak armature current of 200 A.

The magnets were physically present for this analysis, but they were assumed to be completely demagnetized for this analytical exercise to focus attention exclusively on the armature reaction effects. For this analysis, it has been assumed that each magnet pole piece is broken into five identical pieces along the circumferential direction. This was done on the basis of previous work,[19] which showed that the magnet losses can be reduced by more than 80% when this kind of segmented magnet structure is adopted.

Among all of the laminated steel components except for the magnets the predicted iron losses are highest in the stator teeth and lowest in the rotor yoke [Figure 23(a)], following trends similar to those observed in the preceding section for the open-circuit conditions. The major difference between the previous open-circuit and the armature reaction case studied here is that the eddy current losses in the magnets become a significant loss component in the machine when substantial stator currents are flowing.

These magnet losses would have been considerably higher if the magnet poles had not been broken into multiple pieces.

Figure 23(b) presents a different perspective on the FEA-predicted eddy current losses in the teeth caused by the stator currents, broken down in this part of the figure by harmonic component. It is clear from this breakdown that iron losses for the armature reaction operating condition are attributable almost completely to the fundamental component. Additional results not included here show that this is true for the stator yoke and tooth-tips as well. This is good news because it is likely to simplify the task of developing a closed-form analytical model that can predict these iron losses contributed by the stator currents with reasonable accuracy. Efforts to develop this feature of the iron loss prediction method using closed-form analysis are presently under way.

Enhanced Partial Load Efficiency Control Algorithm

High-performance torque control in SPM machines can be achieved using current-regulated vector control. According to this technique, the amplitudes of the instantaneous currents in the three stator phases are controlled so that their combined effect can be represented on a cross-section of the machine as a vector that has an amplitude and angle. A simple representation of this concept that illustrates a current vector, $\vec{i}_s$, for a two-phase alternating current machine is provided in Figure 24. Newcomers to this concept are referred elsewhere for more details.[20]

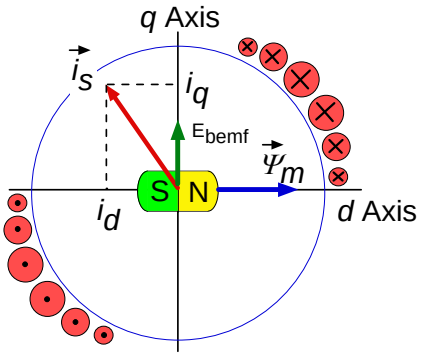

Figure 24. Cross section of two-pole machine illustrating a stator current vector and its decomposition into *d*- and *q*-axis components to achieve vector control of a surface permanent magnet machine.

According to the basic concept of vector control, the amount of torque that is produced by an SPM machine is determined by both the amplitude of the current vector and, very importantly, by its angle with respect to the orientation of the rotor magnets. In Figure 24 the rotor magnet orientation is represented by the magnet flux linkage vector, , aligned with the north pole of the rotor magnets. A two-axis plane can be uniquely defined that is locked to the rotor's instantaneous angular position at every time instant so that the orientation of is defined to be the direct or *d*-axis, and an orthogonal axis is defined as the quadrature or *q*-axis. As a result, any current vector such as in Figure 24 can be uniquely decomposed into an i_d component along with the *d*-axis and an i_q component aligned with the *q*-axis. The torque and the terminal voltage developed by the SPM machine are determined by the values of i_d and i_q, so controlling these two orthogonal current components provides the basis for controlling the torque production of the machine.

Conventional vector control algorithms for SPM machines are based on minimizing the stator copper losses by adjusting the stator current in the rotor-based *dq* frame to achieve maximum torque-per-amp

(*max T/A*) operation.[12, 21] Figure 25 shows the calculated current vector trajectory line for maximum torque/amp operation of the *SPM1* machine over a wide range of rotor speeds in the i_q-i_d plane when delivering 20% of rated torque. According to this algorithm, the value of i_q is essentially constant while i_d is gradually increased (with negative polarity) as the speed is increased beyond the corner point value to accomplish the necessary flux weakening. Flux weakening is required at elevated speeds to counteract the effect of the magnet flux linkage, , sufficiently so that the terminal voltage of the machine at each speed will remain within the maximum limit set by the available source voltage.

It is useful to identify an alternative version of this vector control algorithm to minimize the machine's terminal voltage under all operating conditions by using as much negative *d*-axis current as available to accomplish this objective. The current vector trajectory for this maximum-torque-per-volt strategy is shown in Figure 26 for the *SPM1* machine at 20% of rated torque, exhibiting very little motion over the full speed range. That is, the same current vector amplitude is applied at all speeds, adjusted so that its amplitude equals the rated continuous current value. This algorithm is referred to as maximum torque-per-volt (*max T/V*).

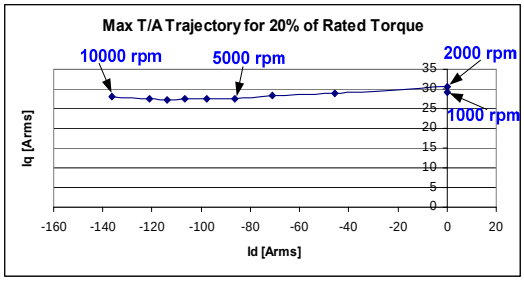

Figure 25. Maximum torque/amp current vector trajectory for *SPM1* machine at 20% of rated torque.

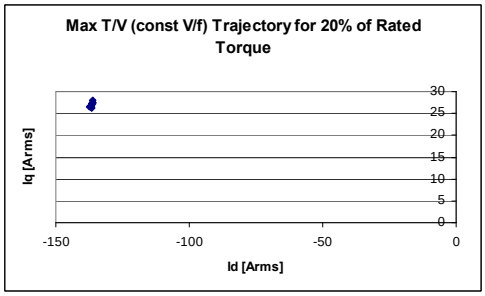

Figure 26. Maximum torque/volt current vector trajectory for *SPM1* machine at 20% of rated torque.

This *max T/V* algorithm is useful for illustration purposes in this discussion because it has the special feature of minimizing the stator core loss by minimizing the stator flux density at all speeds. However, its practical usefulness is very limited because this iron loss minimization is accomplished at the price of maximizing the copper loss.

Some valuable insights are also available by comparing the calculated loss components with each of these two vector control algorithms. Figure 27 confirms that the maximum torque-per-amp algorithm (*max T/A*) delivers lower copper losses at all speeds below maximum speed (10,000 rpm) compared to the *max T/V* algorithm. On the other hand Figure 28 shows that the roles reverse for iron core losses,[9] with the *max T/V* algorithm achieving significantly lower core losses than the *max T/A* algorithm at all speeds below 10K rpm.

An important observation from this exercise is that the *max T/V* algorithm tends to yield higher efficiency at speeds where the iron losses are dominant, while the *max T/A* algorithm tends to achieve higher efficiency at speeds where copper losses are dominant. Figure 29 confirms this observation by comparing the predicted efficiency of the *SPM1* machine at 20% of rated torque for the two algorithms over a wide speed range. More specifically, Figure 29 shows that the *max T/A* algorithm is significantly better for minimizing the total machine losses at low speeds where the iron losses tend to be the lowest, but the *max T/V* algorithm demonstrates its superiority at higher speeds above approx. 2000 rpm, where iron losses are much higher. Unfortunately, Figure 29 also shows that neither algorithm is capable of achieving the 93% efficiency target for the FreedomCAR traction motor, with the largest deficiencies appearing at low speeds.

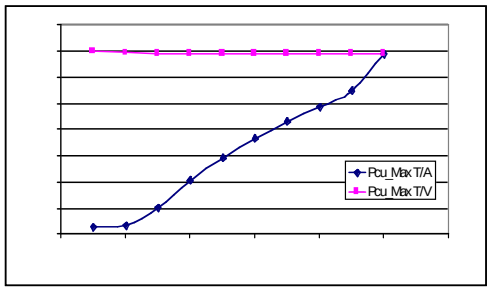

Figure 27. Comparison of predicted copper losses for 20% of rated torque with *max T/A* and *max T/V* algorithms.

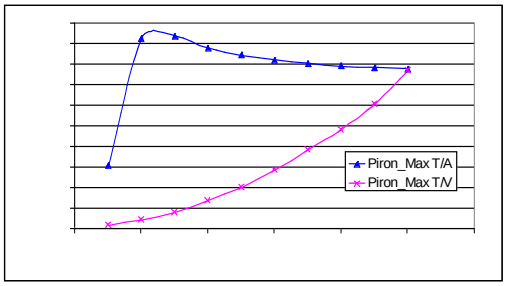

Figure 28. Comparison of predicted iron losses for 20% of rated torque with *max T/A* and *max T/V* algorithms.

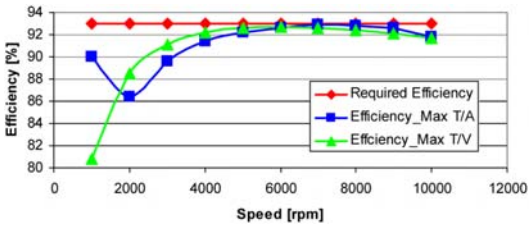

Figure 29. Predicted efficiency of *SPM1* machine at 20% of rated torque for *max T/A* and *max T/V* algorithms, plus specified minimum efficiency line.

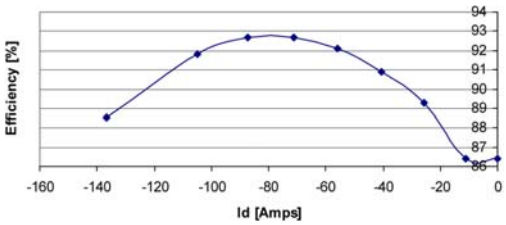

Figure 30. Variation of *SPM1* efficiency at 2000 rpm as a function of i_d with i_q adjusted to hold the torque constant at 20% of rated torque.

A critical observation at this stage is that the *max T/A* and *max T/V* algorithms represent two distinct extremes in the vector control spectrum. In between these two extremes are an infinite number of alternative formulations. Each candidate algorithm represents a different weighted blending of the two extreme algorithms, raising the possibility that a blended algorithm might perform better than either *max T/A* or *max T/V* alone.

An investigation was launched to determine whether there might be another combination of I_q, which determines the resulting torque, and I_d, which is used to adjust the flux level in the machine, that will lead to higher machine efficiency values than either the pure *max T/A* or *max T/V* algorithms.

The results of this investigation have been very promising, indicating that the appropriate blend of the two algorithms can yield significant improvements in the machine efficiency, particularly at those speeds that exhibit the largest deficiencies in Figure 29. As an example, Figure 30 shows the variation of predicted *SPM1* efficiency at 2000 rpm and 20% of rated torque as a function of I_d. The predicted efficiency is approx. 86.5% for the *max T/A* algorithm (when I_d is zero), while the efficiency is approx. 88.5% for the *max T/V* algorithm (I_d = -140 A_{rms}). In between these extremes, the partial-load machine efficiency peaks when I_d = -80 A_{rms} at a value very close to the specified value of 93%. This is a clear indication that choosing the optimum combination of I_d and I_q can have a very significant effect on maximizing the partial-load efficiency of the machine. These results will be discussed further based on the FEA results presented in the following section.

Figure 31 presents the calculated current vector trajectory for achieving the highest partial-load efficiency as the rotor speed is increased from 1000 to 10,000 rpm. By comparing this trajectory to the *max T/A* and *max T/V* current vector trajectories in Figures 25 and 26, it can be observed that the new trajectory adds a higher-level of negative *d*-axis current as a function of rotor speed compared to the *max T/A* trajectory in order to reduce the iron losses, but not as much I_d as the *max T/V* algorithm would require.

Figure 32 shows the new predicted efficiency curve for the *SPM1* machine at 20% of rated torque when the current vector trajectory in Figure 31 is applied as a function of rotor speed. The partial-load efficiency values are boosted at every speed compared to the values plotted in Figure 29 for the *max T/A* and *max T/V* trajectories. In fact, the results in Figure 32 predict that the *SPM1* machine will be able to meet the minimum efficiency requirements (93%) for 20% rated torque over the complete speed range.

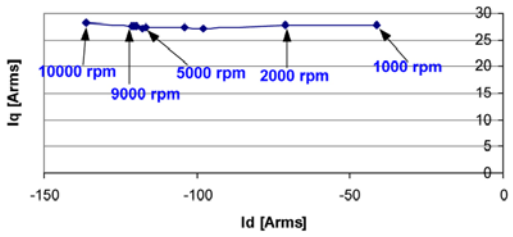

Figure 31. Current vector trajectory for *SPM1* machine to deliver maximum partial-load efficiency at 20% of rated torque.

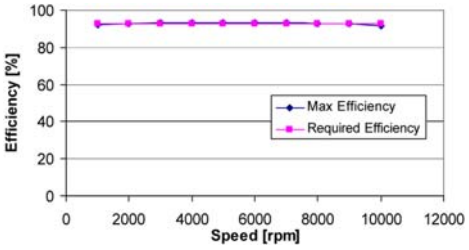

Figure 32. Predicted efficiency of *SPM1* machine at 20% of rated torque for maximum partial-load efficiency, plus specified minimum efficiency line.

Finite-Element Analysis Results

To verify the assumptions used in the analytical calculations of core losses and to gain more insights into the tradeoffs between the copper and core losses for maximizing the partial-load efficiency, FEA simulations using *MagNet 2D* (Infolytica) were carried out. Three operating points at 2000 rpm and 20% rated torque are considered. These points correspond to three distinct points on the partial-load efficiency curve shown in Figure 30, representing *max T/A* (far right), *max T/V* (far left), and *max efficiency* operation at the peak of the curve.

The FEA-predicted magnetic flux density time-domain waveforms in the stator teeth are shown in Figures 33 to 35 for the three highlighted operating points. The harmonic spectrum of the stator-tooth flux density waveform is presented in Figure 36.

The first key observation drawn from these figures is that the magnetic flux density waveforms in the stator teeth are almost purely sinusoidal, as confirmed by the harmonic spectrum in Figure 36. This result is striking because the fractional-slot concentrated windings produce many spatial harmonics in the air-gap flux density waveform.[22] The sinusoidal wave shapes in Figures 33 to 35 justify the sinusoidal approximation adopted for calculating the peak air gap magnetic flux density and, subsequently, for calculating the peak magnetic flux density in the stator teeth and yoke.

The second key observation, drawn from comparing Figures 33 and 34, is that there is an 80% reduction of the peak magnetic flux density in the stator tooth for the *max T/V* algorithm compared to the *max T/A* algorithm. This flux density reduction leads to a significant reduction of the predicted core losses in the stator teeth. This reduction in the stator core loss comes at the expense of an increase in the rms phase current from 30.6 to 139.3 A_{rms} and a corresponding increase in the copper losses, as discussed in the previous section. This result is consistent with the results shown earlier in Figures 27 and 28.

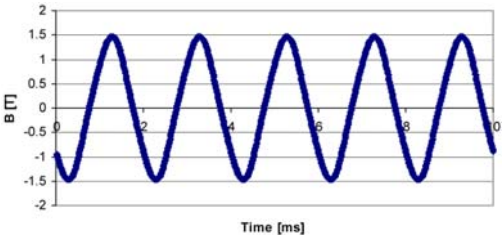

Figure 33. Predicted stator tooth magnetic flux density waveform at 2000 rpm and 20% rated output torque under *max T/A* operating conditions.

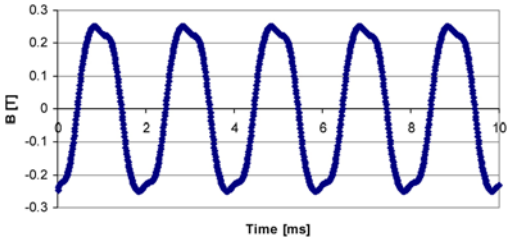

Figure 34. Predicted stator tooth magnetic flux density waveform at 2000 rpm and 20% rated output torque under *max T/V* operating conditions.

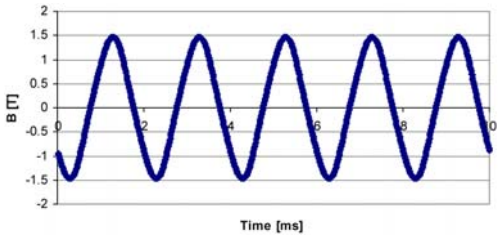

Figure 35. Predicted stator tooth magnetic flux density waveform at 2000 rpm and 20% rated output torque under *max efficiency* operating conditions.

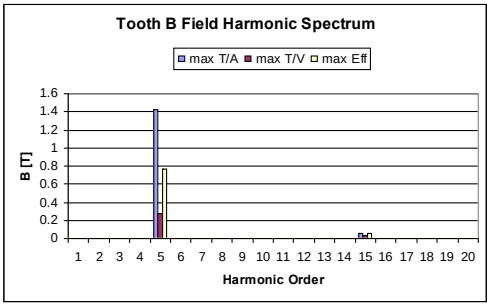

Figure 36. Predicted harmonic spectra for stator tooth magnetic flux density at 2000 rpm, 20% rated torque for the three operating conditions.

Figure 35 shows the predicted stator tooth magnetic flux density waveforms under the *max efficiency* operating conditions. It can be observed that there is almost a 50% reduction in the stator tooth peak magnetic flux density compared to the *max T/A* case. At the same time, there is an increase in the phase current from 30.6 to 76.4 A_{rms}. This blend of the *max T/A* and the *max T/V* algorithms yields the maximum partial-load efficiency for operation at 20% rated torque with a rotor speed of 2000 rpm.

Preparations to Test Control Schemes for the FSCW-SPM Motor

Upgraded hardware and software for use with OPAL-RT have been acquired during FY 2006 to conduct efficiency tests on the 6-kW FSCW-SPM motor for evaluating several control schemes developed by UWM and ORNL. An inverter and an interface card with dead time insertion capability, which communicates with the inverter's control unit while maintaining internal fault protection, allow a rapid prototype system such as OPAL-RT to control the semiconductor device gates while the motor is under actual load. Results of these tests will be used to compare and evaluate the control schemes. The new inverter is a Danfoss VLT 5252, which was purchased to deliver a range of powers up to the 55-kW target of an HEV traction drive system. The VLT 5252 has a typical shaft output power of 200 to 250 kW with normal 110% overload torque and 160 to 200 kW for high 160% overload torque. Figures 37 and 38 show the portable inverter and the internal arrangement of its control unit and power switching section.

Figure 37. Danfoss VLT 5252 inverter on mobile base.

Figure 38. Open door shows Danfoss control unit at top and power switching section at bottom.

Figure 39 shows the special interface card provided by Aalborg University in Denmark. It replaces a card in the Danfoss, which allows gate signals generated by the OPAL-RT system to control inverter switching. This is an effective way of bypassing an inverter's control unit to impress a new control scheme on a motor so that its effect on the motor/inverter system may be evaluated during actual operation.

Figure 39. Interface card with fiber optics and dead time insertion prepared at Aalborg University to allow control of a commercial inverter while maintaining its fault protection features.

ORNL's old OPAL-RT system encountered a problem generating stable PWM signals. It was necessary to upgrade the ORNL target computer and the OPAL-RT software to remedy this problem. The new target PC uses a QNX Version 6.2 operating system with a significantly faster bus speed. Field-programmable-gate-array-based I/O cards, which are expected to solve the unstable PWM problem, are part of the acquisition. Figure 40 shows the new target computer with its two white terminal buses mounted on the front, and Figure 41 shows one terminal bus replaced by a card used during the OPAL-RT pre-test check-out procedure to verify that all cards and software are working properly. Voltage, current, and speed sensor signals will enter the white terminal bus, and gate drive signals for the Aalborg

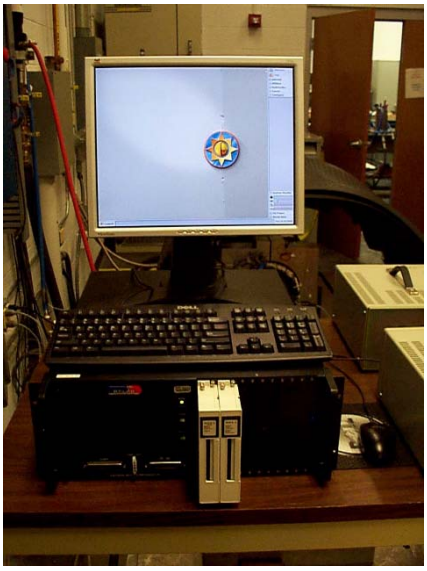

Figure 40. New OPAL RT target PC and connection box.

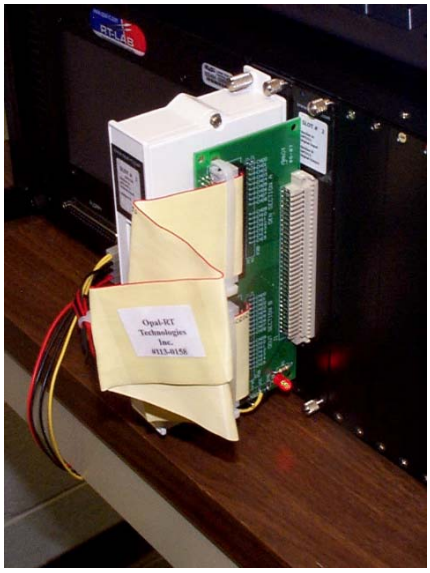

Figure 41. Pre-test diagnostic verification signal bypass card.

card will leave the bus. Current and voltage sensors are shown in Figure 42. The 6-kW motor in its new frame that allows water cooling of the stator is shown in Figure 43.

The checkout procedure for the inverter is in the approval cycle and the pre-test check-outs of the OPAL-RT target computer are in progress. Preparation of the final test plan for efficiency measurements as a function of speed for several partial loads will begin in FY 2007. This plan will be prepared in collaboration with UWM because it must be compatible with their control scheme so that a meaningful comparison of the two schemes may be made.

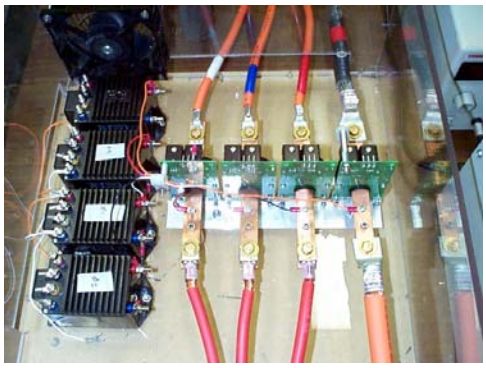

Figure 42. Voltage (black-left), motor current (red-middle) and direct current supply current (orange-right) sensors.

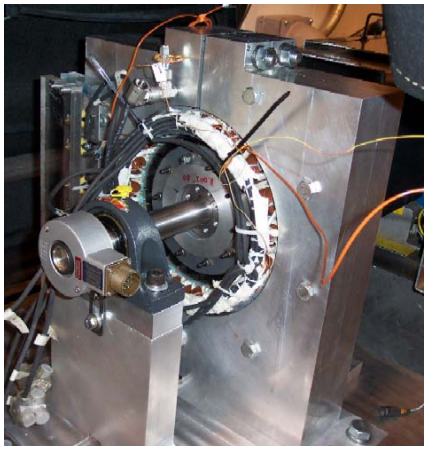

Figure 43. 6-kW fractional-slot SPM motor with concentrated windings.

Conclusions

Equations have been presented showing how a concentrated winding may be used to design increased inductance into an SPM motor with distributed windings. A distributed winding with $N_{spp} = 1$ has the maximum flux linkage with the stator; consequently, to produce comparable torque, a stator with concentrated windings must be able to produce a comparable number of flux links. A relation between the SPM motor with concentrated windings and its fluxmate with distributed windings emerges from the equations. Further, these equations show that there is always sufficient room in the slots of the concentrated windings to add the wire turns necessary to ensure that the flux across the gap for the concentrated windings is the same as that of its corresponding distributed winding, thus the name fluxmate.

The 55-kW design, *SPM2,* proposed by UWM has been evaluated using two design methodologies. The result is a viable design for an HEV traction drive motor. Two such motors, the other being *SPM1,* were designed according to the UWM methodology with a similar pole and slot count to UWM's 6-kW FSCW-SPM prototype now being used to evaluate control schemes at ORNL. With this knowledge, there is mounting evidence that FSCW motors with low pole and slot count are worthy of further investigation for traction applications.

Slight differences between the design results from UWM's application of its design methodology and ORNL's application of commercially available SPEED software have been identified and resolved. These differences relate to methods used to calculate magnet losses. At higher speeds these losses are reduced because more of the current flows at the surface of the conductor, thereby increasing its resistance. This effect is described by saying that the losses at high speeds are inductance limited. These results emphasize the importance of circumferentially stacking the magnets. The differences do not alter the conclusions or the designs proposed by UWM.

A simple proportional speed control has been developed at ORNL for FSCW-SPM motors. Detailed simulation of the control shows that it can effectively control motor speed while minimizing the motor current magnitude during operation above and below base speed. Laboratory testing of this control method and UWM's maximum motor efficiency control will allow comparison and determination of which method exhibits the greatest overall drive efficiency

Significant progress has been achieved during the past year in the development of advanced machine analysis/design and control techniques that will improve the operating efficiency of future FSCW-SPM machines. In particular, the work is contributing to a much-improved understanding of the sources and distribution of FSCW-SPM machine iron losses that play a major role in determining machine efficiency. This new knowledge is being put to use immediately in other programs to design more powerful FSCW-SPM machines for electric traction applications with improved efficiency characteristics.

Future Directions

Setup of the prototype 6-kW FSCW-SPM machine for dynamometer testing at ORNL is in progress. We will prepare a detailed plan to present the specifics for measuring the inverter and motor efficiencies so that the different control schemes may be compared. Each of the control schemes will be programmed in MatLab, compiled for use with OPAL RT, and used to drive the motor.

The detailed test plan will precede efficiency measurements of ORNL's low-cost control scheme to achieve maximum torque per amp below base speed and maximum power per amp above base speed at various speeds and partial loads. Similar test regimens will be used to test UWM's modified vector control algorithm under partial-load operating conditions so that the results may be used to compare control schemes.

During the first quarter of FY 2007 the prototype machine will be exercised under OPAL RT control to obtain the necessary comparative tests. Work is continuing at UWM to enhance the capabilities of the closed-form analytical model for accurately predicting iron losses in FSCW-SPM machines during operation over wide ranges of speed and load conditions. This improved iron loss model will be used to

develop an optimized design of a 55-kW (peak) FSCW-SPM machine to meet the demanding performance requirements for the FreedomCar.

Publications

A. M. EL-Refaie, T. M. Jahns, P. J. McCleer, and J. W. McKeever, "Experimental Verification of Optimal Flux Weakening in Surface PM Machines Using Concentrated Windings," in *Rec. of 2005 IEEE Ind. Appl. Soc. Ann. Mtg.*, Hong Kong, October 2005. *Accepted for publication in IEEE Trans. on Ind. Applications*.

A. M. EL-Refaie, T. M. Jahns, and J. W. McKeever, "Effect of Back-EMF Constraints on Fractional-Slot Surface PM Machines Designed for Wide Constant-Power Speed Range Operation," in *Proc. of 2006 Intl. Conf. on Electrical Machines*, Chania, Greece, September 2006.

A. M. EL-Refaie, T. M. Jahns, and J. W. McKeever, "Modified Vector Control Algorithm for Increasing Partial-Load Efficiency of Fractional-Slot Concentrated Winding Surface PM Machines," in *Rec. of 2006 IEEE Ind. Appl. Soc. Ann. Mtg.*, Tampa, October 2006.

References

1. J. S. Hsu, *Permanent Magnet Energy Conversion Machine,* U. S. Patent No. 5,952,756, September 14, 1999.
2. Cambier et al., *Brushless DC motor Using Phase Advance Timing Advancement*, U.S. Patent 5,677,605, October 14, 1997.
3. J. S. Lawler, J. M. Bailey, and J. W. McKeever, "Extended Constant Power Speed Range of the Brushless DC Motor Through Dual Mode Inverter Control," ORNL/TM-20000/130, July 2000.
4. J. S. Lawler, J. M. Bailey, and J. W. McKeever, "Minimum Current Magnitude Control of Surface PM Synchronous Machines during Constant Power Operation," *IEEE Power Electronics Letters* **3**(2) (June 2005).
5. T. M. Jahns, *Cost Reduction Opportunities for Permanent Magnet Synchronous Machines*, Interim Report prepared for ORNL Technical Project Manager, May 24, 2005.
6. A. M. EL-Refaie, T. M. Jahns, P. J. McCleer, and J. W. McKeever, "Experimental Verification of Optimal Flux Weakening in Surface PM Machines Using Concentrated Windings," *IEEE Ind. Appl. Soc. Annual Meeting*, Oct. 2–6, 2005, Hong Kong.
7. Ayman M. EL-Refaie, *High Speed Operation of Permanent Magnet Machines*, Electrical and Computer Engineering Ph.D. Thesis at the University of Wisconsin–Madison, 2005.
8. A. M. EL-Refaie, T. M. Jahns, and J. W. McKeever, "Effect of Back-EMF Constraints on Fractional-Slot Surface PM Machines Designed for Wide Constant-Power Speed Range Operation," *Int. Conf. on Electric Machines*, September 2006, Greece.
9. C. Mi, G. R. Slemon, and R. Bonert , "Modeling of Iron Losses of Permanent-Magnet Synchronous Motors," *IEEE Transactions on Industry Appl.* **39(**2) (May/June 2003).
10. K. Atallah, D. Howe, P. H. Mellor and D. A. Stone, *Rotor Loss in Permanent-Magnet Brushless AC Machines*, *IEEE Tran. on Ind. Appl*. **36**(6) (November/December 2000).
11. T. Sebastian and G. R. Slemon, "Operating Limit of Inverter Driven Permanent Magnet Motor Drives," *IEEE Trans. Ind. Appl*. **IA-23**(2) 327–333 (March 1987).
12. W. Soong and T. J. E. Miller, "Field Weakening Performance of Brushless Synchronous AC Motor Drives," *IEE Proc. Of the Electronics Power Applications* **141**(6), 331–340 (November 1994).
13. J. S. Lawler, "Control of Surface Mounted Permanent Magnet Motors with Special Application to Fractional-slot Motors with Concentrated Windings," ORNL/TM-2005-184, September 2005.
14. A. M. EL-Refaie, T. M. Jahns, J. W. McKeever, "Modified Vector Control Algorithm for Increasing Partial-Load Efficiency of Fractional-slot Concentrated Winding Surface PM Machines," *IEEE Ind. Appl. Soc, 41st Annual Mtg*., Marriott Waterside Hotel, Tampa, Fl, October 8–12, 2006.
15. V. Zivotic-Kukolj, W. L. Soong, N. Ertugrul, "Iron Loss Reduction in an Interior PM Automotive Alternator," pp. 1736–43 in *Rec. of 2005 IEEE Ind. Appl. Soc. Ann. Mtg*., Hong Kong, October 2005.

16. Z. Q. Zhu, D. Howe, C. C. Chan, "Improved Analytical Model for Predicting the Magnetic Field Distribution in Brushless Permanent-Magnet Machines," *IEEE Trans. Magnetics* **38**(1) (January 2002).
17. Z. Q. Zhu, and D. Howe, "Instantaneous Magnetic Field Distribution in Brushless Permanent Magnet dc Motors, Part I: Open-Circuit Field," *IEEE Trans. Magnetics* **29**(1) (January 1993).
18. D. Zarco, *A Systematic Approach to Optimized Design of Permanent Magnet Motors with Reduced Torque Pulsations*, Ph.D. Thesis, Department of Electrical and Computer Engineering, University of Wisconsin–Madison, 2004.
19. A. M. EL-Refaie and T. M. Jahns, "Comparison of Synchronous PM Machine Types for Wide Constant Power Speed Range Operation," in *Rec. of 2005 IEEE Ind. Appl. Soc, Annual Meeting*, Hong Kong, Oct. 2005.
20. D. W. Novotny and T. A. Lippo, *Vector Control and Dynamics of AC Drives*, New York, Oxford University Press, 1996.
21. Z. Q. Zhu, U. S. Chen, and D. Howe, "Iron Loss in Permanent-Magnet Brushless AC Machines Under Maximum Torque per Ampere and Flux Weakening Control," *IEEE Trans. Magnetics*, **38**, 3285–3287, September (2002).
22. A. M. EL-Refaie, T. E. Jahns, and D. W. Novotny, "Analysis of Surface Permanent Magnet Machines Equipped with Concentrated Windings," *IEEE Trans. Energy Conversion*, **21**, 34–43, March 2005.

3.4 Extending the CPSR of Synchronous Reluctance Motors

Principal Investigator: John W. McKeever
Oak Ridge National Laboratory
National Transportation Research Center
2360 Cherahala Boulevard
Knoxville, TN 37932
Voice: 865-946-1316; Fax: 865-946-1262; E-mail: mckeeverjw@ornl.gov

DOE Technology Development Manager: Susan A. Rogers
Voice: 202-586-8997; Fax: 202-586-1600; E-mail: Susan.Rogers@ee.doe.gov

ORNL Program Manager: Mitch Olszewski
Voice: 865-946-1350; Fax: 865-946-1262; E-mail: olszewskim@ornl.gov

---

Objectives

The objective of this project was to determine if a reliable per-phase analytical model could be developed for a synchronous reluctance motor. A per-phase model, which has been developed for brushless dc permanent magnet (PM) motors and for switched reluctance motors, has been used to show that both of these motor types have unbounded constant power speed ratios (CPSRs) if resistance and speed sensitive losses are neglected. If a reliable per-phase model could be developed, it could be used to determine if a synchronous reluctance motor also has an unbounded CPSR. During the development of a per-phase model of the switched reluctance motor, detailed computer modeling revealed that, as the speed of the model increased, saturation did not impact its performance. The question is whether saturation-independent behavior is true for a synchronous reluctance motor, considering the different drive mechanisms.

Another objective was to model a synchronous reluctance motor using available commercial motor design software to determine performance targets that may be compared with the FreedomCAR targets. This would provide an idea of the extent to which performance targets had to be improved to make this motor an a hybrid electric vehicle (HEV) traction drive candidate.

Approach

Commercial software was used extensively during this part of the project. ORNL is a member of the SPEED Consortium, based at the University of Glasgow, Scotland. Consequently, SPEED software was used to model two synchronous reluctance motor inverter designs and to check their performance characteristics. Two other software packages employed were FLUX2D and COMSOL. Although FLUX2D has a good magnetic solution capability, construction of models was difficult, requiring extensive technical support from Magsoft. COMSOL proved to be far more versatile and, because of its ability to represent saturation, was helpful in determining how important it is that saturation be a part of any model we develop.

An attempt was made to define a per-phase model like the one used for brushless dc motors and switched reluctance motors. The winding function, which assumes an idealized machine with uniform air gap, was applied to a reluctance motor with salient rotor and salient stator poles. The double salient poles have a very nonuniform gap. This nonuniformity caused flux fringing at all positions of the rotor pole from its aligned to unaligned positions, making use of the winding function an approximation. A model of a synchronous reluctance motor using COMSOL showed that flux fringing effects are significant. Use of the winding function as an approximation gave equations for direct and quadrature inductances

corresponding to the aligned and unaligned positions of the rotor. A detailed finite-element analysis will be necessary to quantify the reliability of the per-phase model.

Meaningful analyses were provided by using COMSOL to examine the flux patterns between the rotor and stator during operation of a synchronous reluctance motor. The results and conclusions of this analysis are included in this report.

Major Accomplishments

1. We applied FLUX2D software to determine the phase advance, which is the angle between the center of a rotor pole and the stator current orientation, that will produce maximum torque. ORNL created a model of a PM motor with inset magnets and turned off the magnets to simulate a synchronous reluctance motor with doubly salient poles. The torque produced was then calculated for a fixed rotor as the current in the stator was varied over one pole and for current fixed in the stator with the rotor turned through one pole angle. Definite maxima were found with only rough agreement between the two approaches. A similar exercise with COMSOL demonstrated good agreement between the two approaches for estimating the phase advance for maximum torque.
2. Using SPEED as a design tool, two synchronous reluctance motors were modeled to try to meet FreedomCAR targets. The first model with four turns per pole could not deliver maximum power at 2000 rpm. Adequate power at 2000 rpm required eight turns per pole, which doubled the amount of copper to increase both cost and weight. The motor was too heavy and too expensive to meet FreedomCAR goals.
3. We defined a per-phase model by applying a winding function to a synchronous reluctance motor with salient rotor and stator poles to determine the inductance that should be used. This approach yielded direct and quadrature inductances, which had to be added for use in the model. Unfortunately, flux fringing, verified by a COMSOL analysis, indicated that use of the winding function was clearly an approximation. Later work showed that a reliable model should include not only flux fringing but also saturation.
4. We constructed detailed models of switched reluctance motors to study flux behavior in a synchronous reluctance motor. Variations in the study included (1) a solid rotor to study the effect of eddy currents on the rotor; (2) regular reluctance rotors turning inside stators with and without shoes in their teeth; and (3) a comparison of synchronous reluctance motor performance, assuming no saturation with performance, that included saturation as part of the model. Overall results strongly suggested that any reliable model of a synchronous reluctance motor must incorporate flux fringing as well as saturation.

Technical Discussion

Modeling a Synchronous Reluctance Motor using SPEED Software

Two SPEED models of a synchronous reluctance motor

Two similar synchronous reluctance motor designs were studied to assess their potential to meet the targets of the FreedomCAR program. The two designs differ in the number of turns used in the stator. Their rotors are identical and consist of four poles made of six U-shaped plates of magnetic steel separated by five air gaps. Figure 1 shows a schematic drawing of the synchronous reluctance motor design considered.

Table 1 contains the performance data for a synchronous reluctance motor with four stator turns per pole. Top speed is 10,000 rpm, and performance values are at 20% of top speed.

Table 2 contains the performance data for a synchronous reluctance motor with eight stator turns per pole. Again top speed is 10,000 rpm, and performance values are calculated at 20% of top speed.

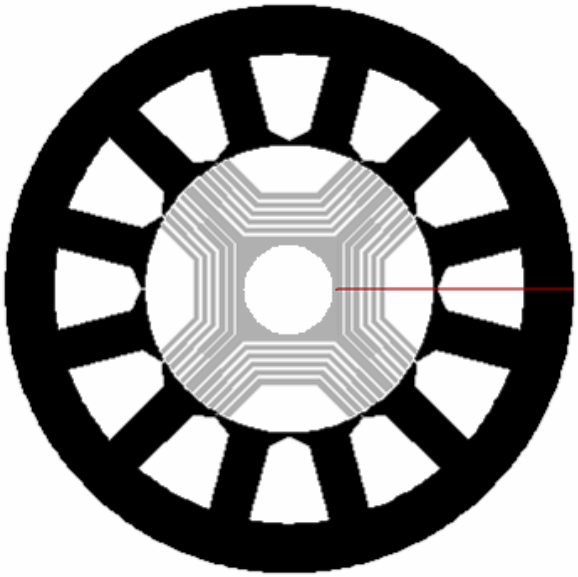

Figure 1. Schematic of a synchronous reluctance motor (4 poles, 12 slots, 40-cm diameter, 100 cm long, no permanent magnets).

Table 1. SPEED performance data for a synchronous reluctance motor whose stator has four turns per pole

25 kW at 2,000 rpm with 93% efficiency using γ = 65 eDeg 565-A peak current, 400-A_{rms} current, 92 V_{LL} => 118 V_{dc} Current density = 5.1 A/mm^2
55 kW at **10,000** rpm with 96% efficiency using γ = 49.5 eDeg 322-A peak current, 228-A_{rms} current, 342 V_{LL} => 438 V_{dc} Current density = 2.9 A/mm^2
30 kW at **10,000** rpm with 96% efficiency using γ = 46 eDeg 233-A peak current, 165-A_{rms} current, 262 V_{LL} => 336 V_{dc} Current density = 2.1 A/mm^2
Total weight 65.6 kg (30 kg of Cu and 45 kg of Fe) Total volume = 12.6 L Peak power/weight = 0.73 kW/kg [<**2.75**] Peak power/volume = 4.4 kW/L [<**12.5**] (i.e., about factor of 3 below target for power density)

Table 2. SPEED performance data for synchronous reluctance motor whose stator has eight turns

55 kW at **2,000** rpm with 94% efficiency using γ = 75 eDeg 565-A peak current, 400-A_{rms} current, 297 V_{LL} => 381 V_{dc} Current density = 5.1 A/mm^2 30 kW at **2,00**0 rpm with 96% efficiency using γ = 65 eDeg 330-A peak current, 233-A_{rms} current, 203 V_{LL} => 260 V_{dc} Current density = 2.9 A/mm^2
7.5 kW at **10,000** rpm with 96% efficiency using γ = 45 eDeg 58-A peak current, 41-A_{rms} current, 262 V_{LL} => 336 V_{dc} Current density = 0.5 A/mm^2
Total weight 106 kg (**61** kg of Cu and 45 kg of Fe) Total volume = 12.6 L Peak power/weight = **0.52** kW/kg [<**2.75**] Peak power/volume = 4.4 kW/L [<**12.5**] (i.e., about 5 and 3 times below targets for power density)

A sample SPEED design sheet for the Table 2 case is contained in Table 3.

Table 3. Design sheet for the reluctance motor shown in Figure 1

PC-SREL 1.5 for Windows (1.5.2.1) 2/8/2006 11:50:00 AM
F:\My Documents\pjo_srel_motor55kwFC2krp.sy1
UT-Battelle, LLC
PC-SREL main title
PC-SREL sub-title

1 Dimensions:----------

RotorRad	100.000 mm	BoreRad	102.000 mm	Gap	2.000 mm
FrameRad	200.000 mm	ShaftRad	34.000 mm	POLES	4
SLOTS	12	TWS	28.000 mm	SD	64.000 mm
SO	2.000 mm	TGD	2.000 mm	TGANG 4	0.000 mDeg
RNSQ	Square	Stf	0.970	RotType	Ax. Lam
LStator	100.000 mm	LRotor	100.000 mm	LShaft	150.000 mm
LMotor	175.000 mm	1stLayer	Guide	PoleMat	Insulation
NLayers	12	B_Thick	2.000 mm	G_Thick	4.000 mm
NumGuide	6	NumBarrs	6	PoleArc	42.200 mDeg

2 Control Data:----------

RPM	2000.000 rpm	I(rms)	233.000 A	Gamma	65.000 eDeg
Vs(dc)	450.000 V				
Vtrans	0.000 V	Rtrans	0.000 Ohms	Vdiode	0.600 V

3 Winding Data:----------

WdgType	Lap	Connex	Wye	Throw	3
TC	8	CoilsPer	1.000	NSH	1
Tph	32.000	PPATHS	1	SPP	1.000
Layers	2.000	CSidesPh	8	Z	0.000
MLT	917.191 mm	Ext	0.000 mm	LgthOEnd	328.289 mm
MaxSFill	0.492	EndFill	0.500	LaxPack	314.087 mm
SFill	0.492	WDia	10.000	WireSpec	BareDia
WireDia	10.000 mm	Liner	0.400 mm		
SlotArea	2554.242 mm^2	CondArea	78.540 mm^2	ASlotLL	2473.684 mm^2
WdgTemp	25.000 DegC	Rph	6.478E-03 Ohm/Ph	Rterm	0.013 Ohms
PCSlot	3.455	XET	1.000	Ax1	75.000 mDeg
ks1	1.000				
kw1	1.000	Nse	40.744		

Table 3. (continued)

4 Magnetic Circuit Design:----------					
Bg1OC	0.821 T	PhiM1	8.374 mWb	Bt_pk	1.614 T
Bg_pk	0.821 T	Bf_pk	1.270 T	Bg_pk	1.370 T
				BgBH_pk	3.426 T
5 Inductance Values:----------					
Kc_Rotor	1.054	Kc_Stat	1.007	Kc_Total	1.061
XLq_m	1.000	XLd_m	1.000	XLslot	1.000
XLendt	1.000	LSlot	0.445 mH/Ph	Lendt	0.088 mH/Ph
XLTthTip	1.000	LTthTipD	0.246 mH/Ph		
MSlot	0.000 mH/Ph	fz	1.020	Xq	0.860 Ohm/Ph
Xm0	1.249 Ohm/Ph	Xsigma	0.223	Xq	0.860 Ohm/Ph
Lq/Ld_i	25.500	L_m	2.982 mH	Ld_i	0.125 mH
Lq/Ld_mU	6.231	Lq_m(U)	2.343 mH	Ld_m	0.376 mH
Lq/Ld_mS	5.150	Lq_m(S)	1.936 mH	Ksat_Lmq	1.210
Lq/Ld(U)	2.491	Lq(Usat)	2.876 mH	Ld	1.154 mH
Lq/Ld(S)	2.139	Lq(Sat)	2.469 mH		
6 Sine-wave static performance [phasor diagram]:----------					
Torque	142.904 Nm	PowerM	29929.669 W	Eff	96.015 %
LossCu_S	1055.105 W	LossFe_R	0.000 W	LossFe_S	187.249 W
LossWF	0.000 W	LossTot	1242.354 W	Jrms	2.967 A/mm^2
IWpk	329.512 A	IWav	209.774 A	IWrms	233.000 A
ILpk	329.512 A	ILav	209.774 A	ILrms	233.000 A
IDchpk	0.000 A	IDchav	0.000 A	IDchrm	0.000 A
IDClinkS	69.271 A	LossConv	0.000 W	kVA	82027.629 kVA
Iq1	98.470 A	Id1	–211.170 A	Gamma	65.000 eDeg
Vq1	–79.742 V	Vd1	–86.094 V	Delta	132.806 eDeg
Vs1	350.864 V	Vs1Lin	275.568 V	Phi	67.806 eDeg
Vph1	117.350 V	VLL1	203.256 V	TempRise	37.271 DegC
PF_fund	0.378	PF	0.380	Appt_PF	0.365
7 Mechanical Data:----------					
NumBolts	6	BoltDia	10.000 mm	BoltLgth	66.000 mm
BoltTdDp	0.167 mm	BoltSpac	13.333 mm	BoltHdCl	1.650 mm
BoltInSh	1.650 mm	BtClInSh	64.700 mm	BHdClMin	1.149 mm
BltLoss%	0.600	BoltYStr	230.000 MPa	ShftYStr	300.000 MPa
TensBlt	16879.952 N	ShearThB	2881.233 N	ShearThS	3887.721 N
SpeedMax	2157.190 rpm				
8 Miscellaneous:----------					
WtCu	60.856 kg	WtFe	45.189 kg	WtMag	0.000 kg
WtTot	106.045 kg	RotJ	0.000 kg-m^2	LosFe/Wt	4.144 W/kg
Sigma	3.298 psi	XFe	1.000	Freq1	66.667 Hz
TempCalc	DegCW	DegCW	0.030 degC/W	HTransCo	265.258 W/m^2/C
Ambient	25.000 DegC	HTransCo	0.000 W/m^2/C		
Wf0	0.000 W	RPM0	1000.000 rpm	NWFT	1.000
9 Core loss analysis:----------					
SSteelNa Transil Bs=1.3T 35					
RSteelNa Transil Bs=1.3T 35					
WtTeeth	16.823 kg	WtYoke	28.366 kg	WtTroot	4.145 kg
LossTthE	25.082 W	LossTthH	82.736 W	LossTth	107.818 W
LTthE/Wt	1.196 W/kg	LTthH/Wt	3.946 W/kg	LTth/Wt	5.142 W/kg
LossYkE	20.985 W	LossYkH	58.446 W	LossYk	79.431 W
LYkE/Wt	0.740 W/kg	LYkH/Wt	2.060 W/kg	LYk/Wt	2.800 W/kg
LossE50	0.581 W	LossH50	2.376 W	LossFe50	2.957 W
End of Design sheet----------					

Both designs have the same overall volume and the same mass of steel. The motor with four stator turns has one-half the mass of copper of the motor with eight turns.

Because of its lower number of turns, the four-turn motor excels at high speeds, while the eight-turn motor is best for low speeds. Specifically, at 2,000 rpm, with the same 400-A_{rms} current limit, the four-turn motor produces 25 kW, while the eight-turn motor produces 55 kW. At 10,000 rpm, with the same voltage limit of 336 V_{dc}, the four-turn motor produces 30 kW, while the eight-turn motor produces only 7.5 kW.

The purely synchronous reluctance motor (no PM) will be large and must be capable of changing the number of active turns to cover the whole range of operation as required by the FreedomCAR specifications. The power density of both motors is one-third of the FreedomCAR goal.

Conclusions from the SPEED Modeling

The power density of synchronous reluctance motors will always benefit from the addition of PM in the rotor; however, adding magnets makes this motor configuration an internal permanent magnet motor, which should be researched with other IPMs. A major reason for studying reluctance motors is to learn how to harvest additional magnet-free torque from them at all speeds. Eliminating magnets could become strategic if their cost rises. Heavy vehicle manufacturers such as LeTorneau have incorporated this type of motor in their loaders and bulldozers because of their sturdy construction, high performance, efficiency, productivity, and simplicity. It is very likely that the synchronous reluctance motor can overcome the torque ripple problems encountered by switched reluctance motors because of its synchronous operation. Some fruitful areas for further research are (1) employing non-sinusoidal waveforms; (2) placing PM materials at symmetrical as well as asymmetrical places on the rotor; and (3) determining how to match the effective number of stator turns to the speed and power requirements of the motor and exploring how to switch the stator turns in and out of the circuit during operation of the motor.

Finite-Element Analysis of Reluctance Motors using COMSOL

Finite-element models of the synchronous reluctance motor were run using stators with and without shoes in their teeth and using several different rotors. To assess the effect of saturation and discreteness of the stator teeth, slot openings, and nonsinusoidal winding distribution on the shape of the rotating magnetic flux produced in the stator and motor, a solid cylindrical rotor was simulated. It was also used to compute the eddy currents induced when the cylinder is a good electrical conductor. The other rotors sported a conventional layered structure with different additions of PM material.

Solid Rotor Study

The colors in Figure 2 show the flux in Tesla, and the contours are lines of constant magnetic potential. Comparing Figures 2(a) and 2(b) illustrates the impact of eddy currents in the rotor. In Figure 2(b) the eddy currents induced in the rotor's surface prevent the stator magnetic flux from crossing the air gap into the rotor, as evidenced by the fact that the contours do not cross the gap.

The effect of magnetic saturation and the stator's heterogeneity on the magnetic flux crossing the air gap is shown in Figure 3. Figure 3(a) shows that the rotor's surface-averaged flux has a trapezoidal ripple of about 6% with a frequency equal to that of the slot-opening crossing. Colored dots correspond to the colored curves in Figure 3(b). The distribution of the flux around the rotor surface is shown in Figures 3(b) and 3(c) to be far from sinusoidal. The generation of torque around the periphery of the solid rotor is shown in Figure 4 to be very small but not uniform.

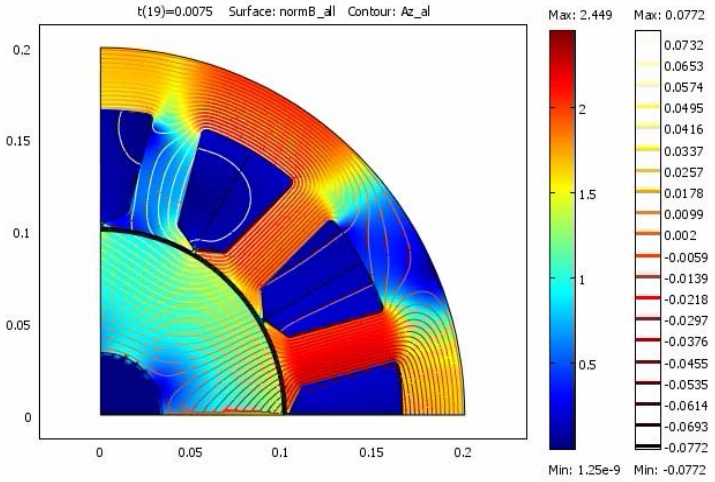

(a) Electrically nonconductive steel rotor.

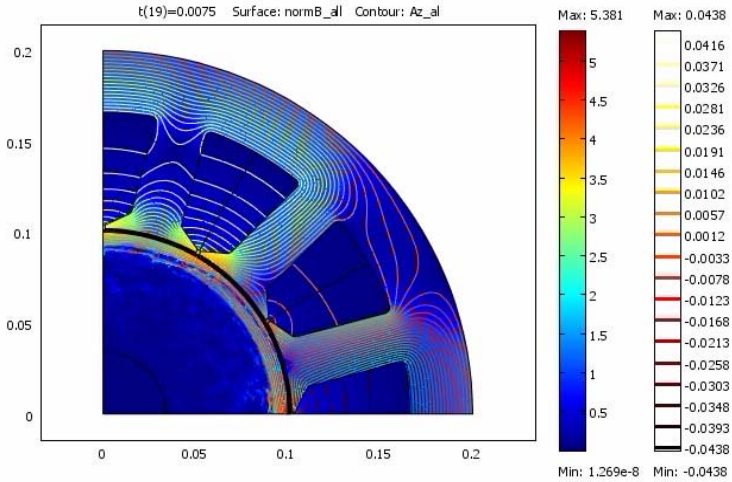

(b) Electrically conductive iron rotor.

Figure 2. Magnetic flux lines generated by the stator's rotating field in a reluctance motor with a solid rotor.

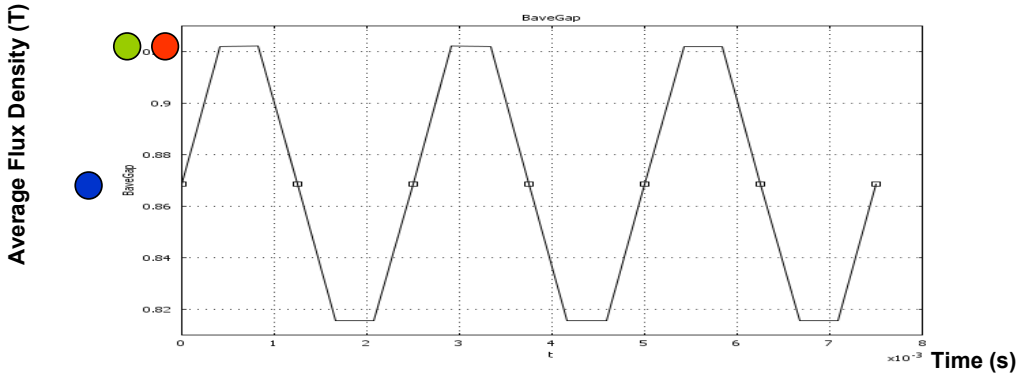

(a) Average air gap flux density for a solid nonconductive steel rotor as a function of time.

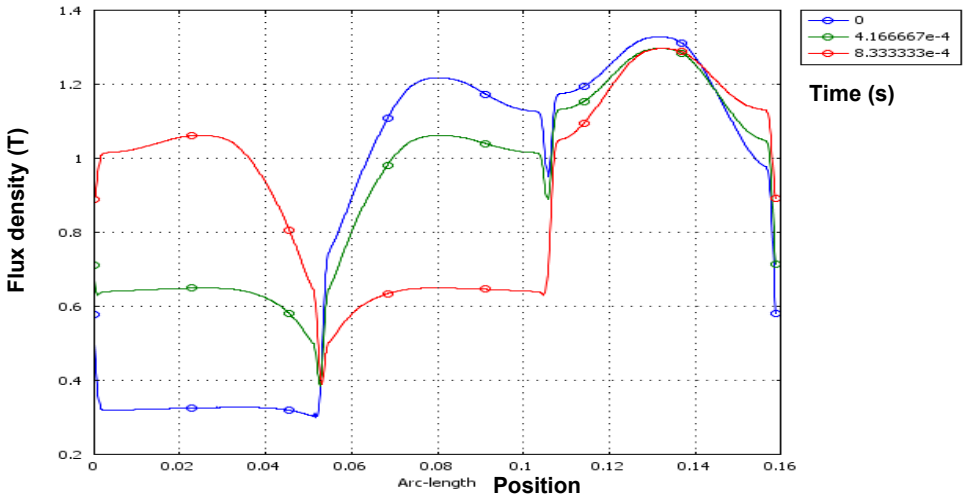

(b) Flux density distribution for a nonconductive steel rotor at the three times marked in (a).

Figure 3. Distribution of magnetic flux crossing the air gap generated by the stator's rotating field in a motor with a solid rotor.

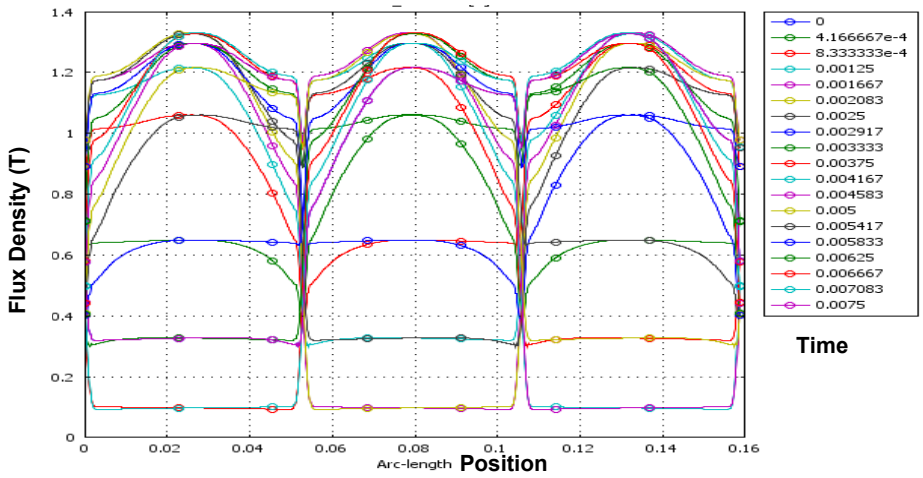

(c) Flux distribution for a nonconductive steel rotor at times spanning a quarter turn.

Figure 3. (continued).

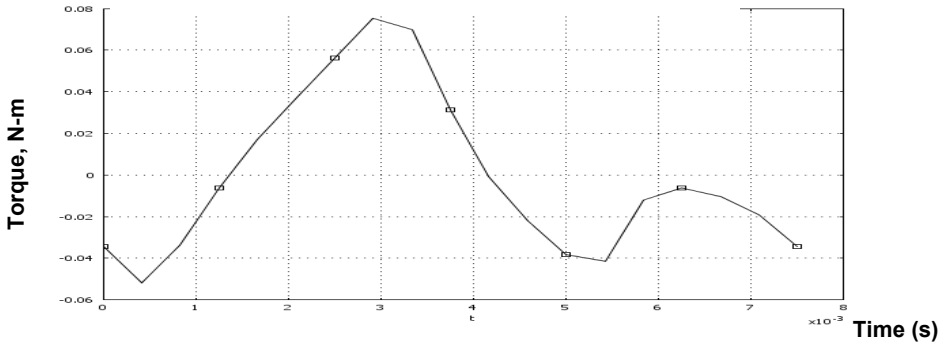

Figure 4. Total torque in the motor with a solid rotor made of nonconductive steel as a function of time for a quarter turn.

Layered Reluctance Rotors

In addition to the stators with and without shoes and the classic rotor shown in Figure 1, several configurations with varying amounts and locations of PM material inserted between the steel layers were simulated. The definitions of these configurations appear in Figure 5.

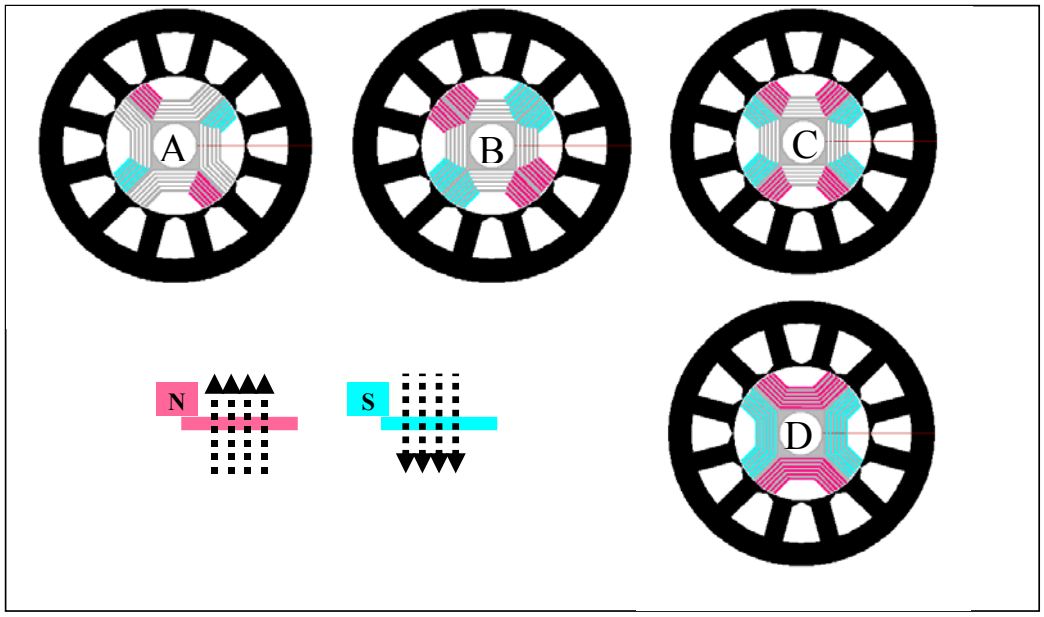

Figure 5. Modified synchronous reluctance motor types with PMs added between the rotor's steel layers. (a) alternating single magnets, (b) back-to-back magnets, (c) alternating dual magnets, and (d) full pole magnets.

Comparison of Torque Generation

In the following figures, the suffix to the rotor type _s indicates that the stator teeth had shoes attached, and _ns indicates that the teeth had no shoes attached. Figure 6 compares designs B_s and C_s and shows that C, the rotor with consecutive poles partially loaded with PMs of the **same** polarity has the highest peak torque value. For about one-half of the angle range, though, the type B design exhibits higher torque values.

Figure 7 compares the torque as a function of control angle for motors with different rotors for each of the two stator types. The designs fully loaded with PMs, D_ns and D_s, have the highest peak torque values. The design without shoes has a slightly higher maximum torque. Although torque is zero for γ = 120 eDeg, which is the angle where the radial flux is maximum corresponding to the green line in Figure 8, the maximum torque occurs for γ = 265 eDeg rotating in one direction and 335 eDeg in the other. The notation, eDeg, means electrical degrees. The average flux at 335 eDeg also happens to be a minimum. Comparison of the peaks and valleys in Figures 7 and 8 shows that higher average fluxes do not necessarily produce higher torques at the corresponding control angles.

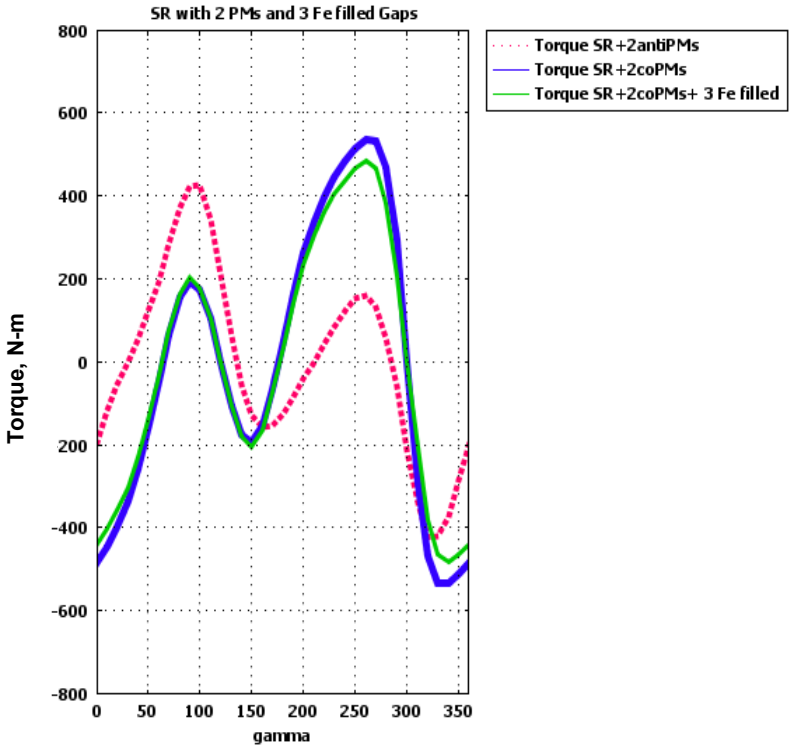

Figure 6. Torque as a function of stator current angle, γ.

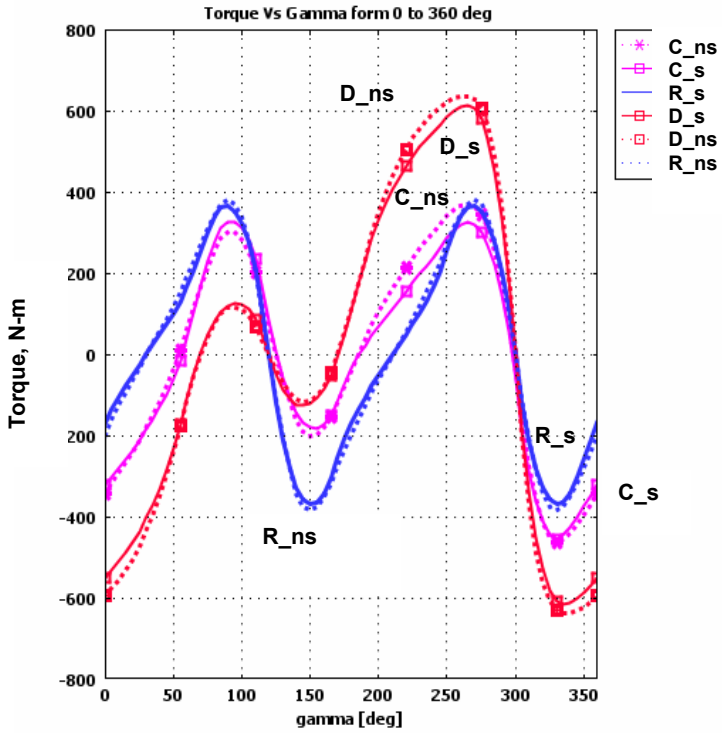

Figure 7. Torque as a function of stator current angles from 0 to 360 eDeg.

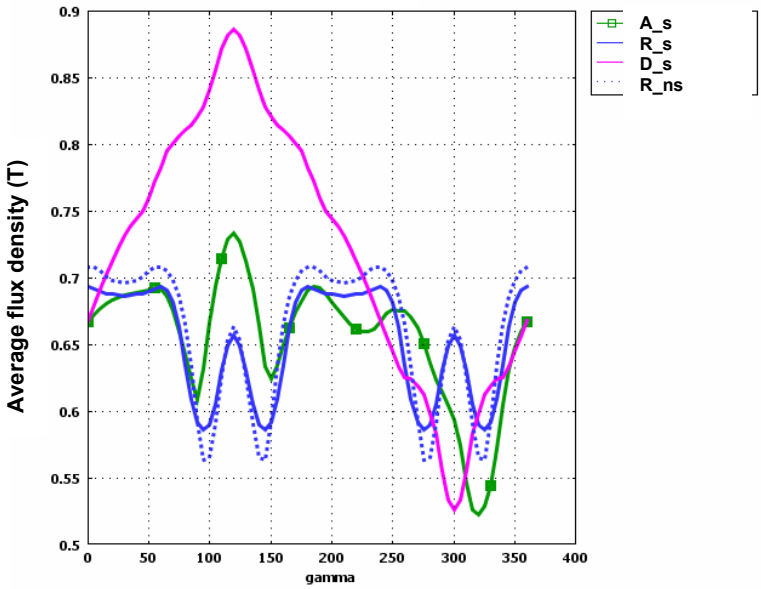

Figure 8. Average flux at the rotor surface for stator current angles from 0 to 360 eDeg.

Flux Shapes along the Rotor Periphery

In this section we illustrate the impact of saturation and stator/rotor nonuniformity on the magnitude and shape of the stator and rotor. Figure 9 shows the permeability dependence on local magnetic flux for the two cases considered: saturating and nonsaturating. The figures below correspond to a motor of type A with no shoes in the stator teeth. The stator current is 400 Arms. Figures 10 and 11 show the dramatic reduction in torque and flux levels and shape distortion when saturation is considered. The peak torque is three times smaller when saturation is considered.

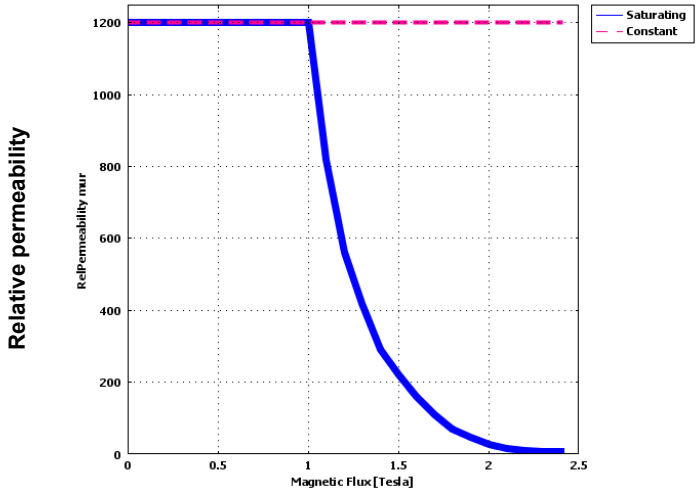

Figure 9. Permeability dependence on flux for study on the effect of saturation.

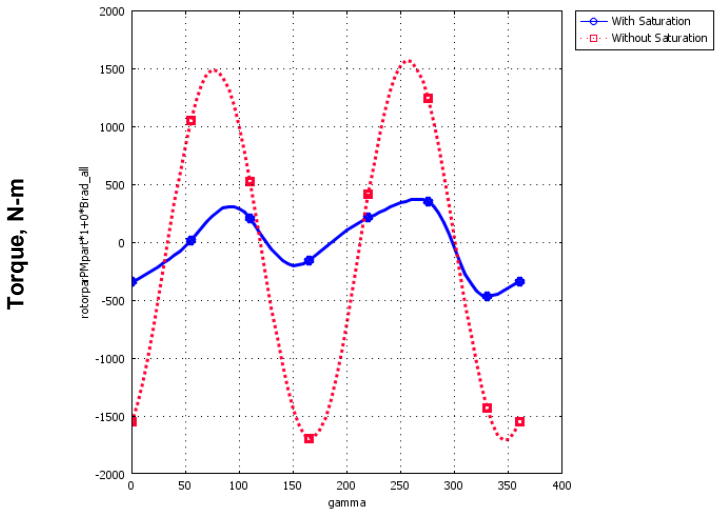

Figure 10. Torque vs control angle, γ, with and without saturation.

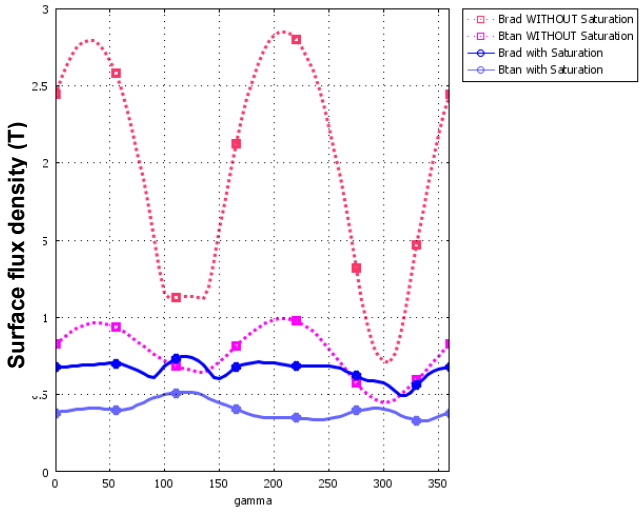

Figure 11. Average radial and tangential rotor surface flux components vs control angle, γ, with and without saturation.

Note that maximum torque corresponds to the situation in which the control angle is such that the two stator teeth close to the rotor iron pieces are unevenly loaded with magnetic energy. In Figure 12(b) the two are heavily loaded, saturated, and because they attract the rotor's iron in opposite directions, they cancel each other and produce no net torque.

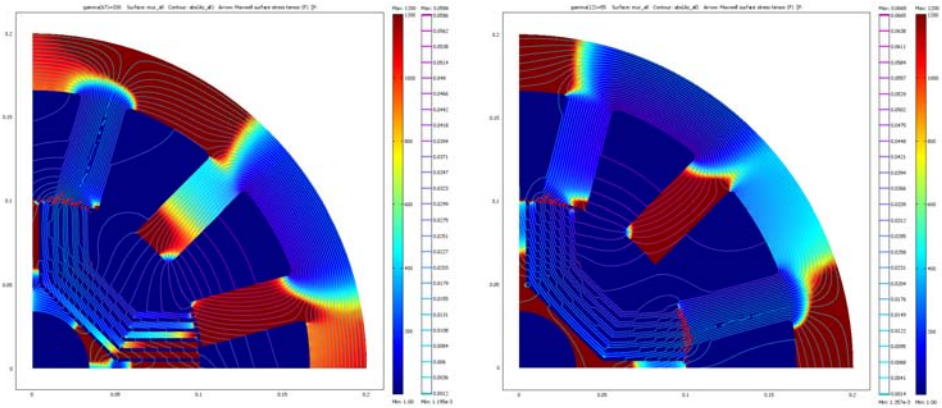

(a) for γ= 330 eDeg where torque is maximum **(b) for γ = 55 eDeg where torque is zero**

Figure 12. Permeability and flux lines in a type A motor with no shoes on the stator teeth. The bottom of the scale (dark blue) corresponds to $\mu_r = 1$ (saturated iron), and the top of the scale (dark red) corresponds to $\mu_r = 1200$ (unsaturated iron).

In Figures 13 and 14, the envelope created by the shapes of the radial and tangential components of the flux distribution around the rotor surface are shown for all angle control positions from 0 to 360 eDeg. For clarity, the same is shown only for control angles from 0 to 45 eDeg in Figures 15 and 16. Better yet, Figure 17 shows the flux shapes only for the control angle that produces optimal torque in the motor. As can be seen in Figure 10, these angles are 330 eDeg with saturation and 350 eDeg without saturation.

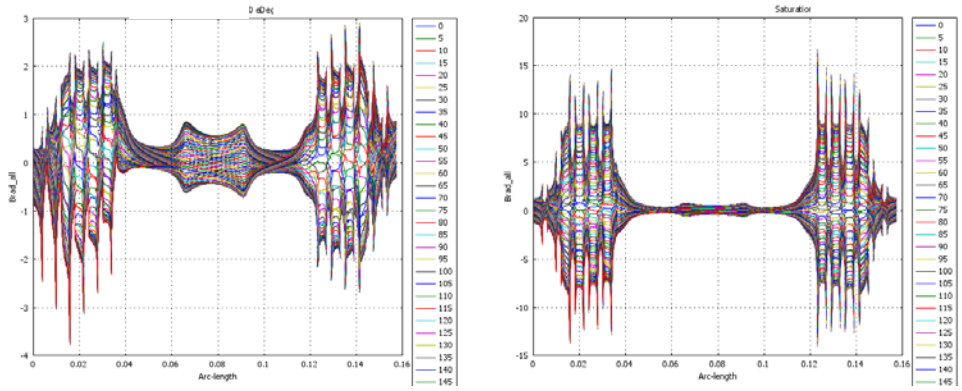

(a) Saturation **(b) No saturation**

Figure 13. Radial flux distribution along the rotor periphery for γ = 0 to 360 eDeg. [The Y-axis scale in (b) is much larger for the nonsaturating case.]

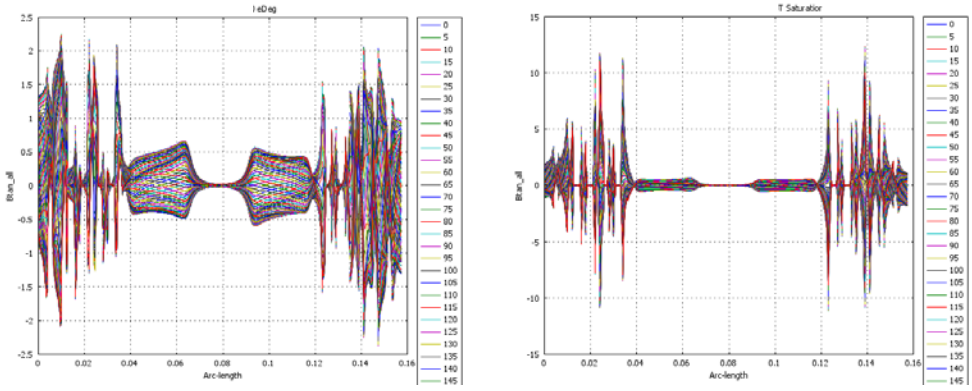

(a) Saturation **(b) No saturation**

Figure 14. Tangential flux distribution along the rotor periphery for γ = 0 to 360 eDeg. [The Y-axis scale in (b) is much larger for the nonsaturating case.]

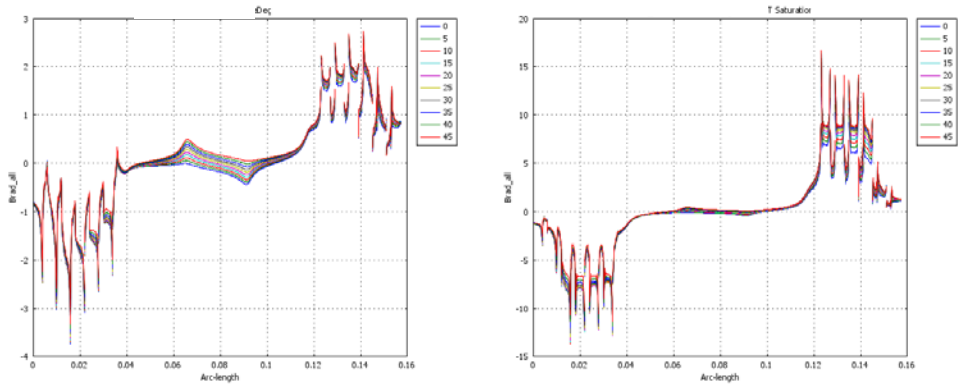

(a) Saturation **(b) No saturation**

Figure 15. Radial flux distribution along the rotor periphery for γ = 0 to 45 eDeg. [The Y-axis scale in (b) is much larger for the nonsaturating case.]

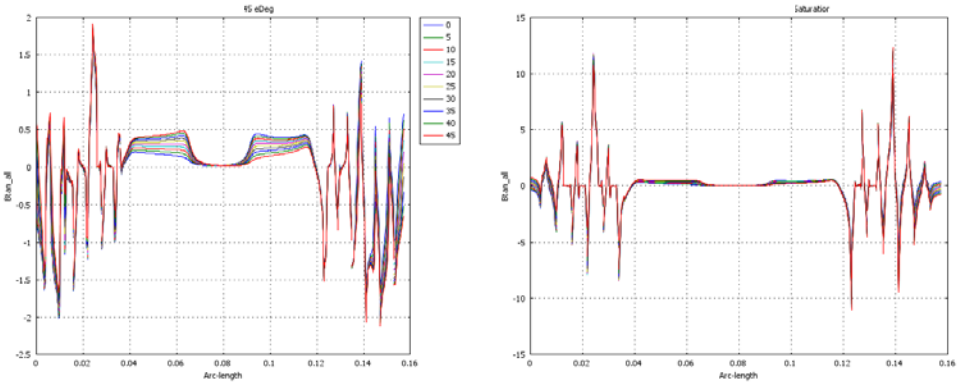

(a) Saturation **(b) No saturation**

Figure 16. Tangential flux distribution along the rotor periphery for γ = 0 to 45 eDeg. [The Y-axis scale in (b) is much larger for the nonsaturating case.]

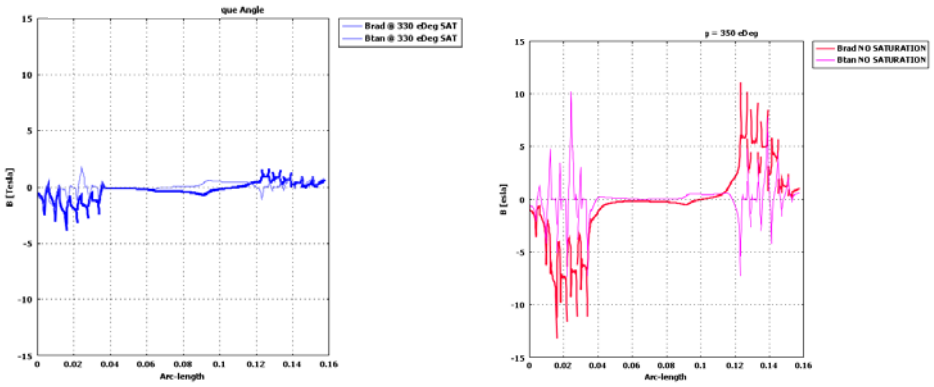

(a) Saturation for γ = 330 **(b) No saturation for γ = 350**

Figure 17. Radial and tangential flux distributions along the rotor periphery for optimal control angle.

Conclusions

Because today's performance of synchronous reluctance motors is below the FreedomCAR targets the potential of the synchronous reluctance motor is often overlooked. These motors exhibit sturdy construction, high performance, efficiency, productivity, and simplicity. It is very likely that the synchronous reluctance motor can overcome the torque ripple problems encountered by switched reluctance motors because of its synchronous operation. For these reasons it is plausible that synchronous reluctance motors may one day be utilized as traction motors if the cost of PMs escalates.

Motor modeling must use actual geometries and solve fundamental equations with as few approximations as possible. At this time finite element analysis seems the best way to directly solve the mathematical equations and account for specific geometric and material properties as well as nonlinear effects such as those introduced by magnetic saturation. Saturation needs to be accounted for as accurately as possible because it affects very significantly the magnitude and shape of the torque and flux distributions.

Because of geometry of stator slots, discreteness of windings, rotor asymmetries, and saturation, actual flux distribution shapes are far from sinusoidal; thus, lumped parameter simulations are always suspect until measured data are available and adjustments are made to the models. This suggests that it will be a challenge to develop a reliable per-phase model of a synchronous reluctance motor.

Our finite-element studies described above have shown that the power density of synchronous reluctance motors will always benefit from the addition of PM in the rotor; however, adding magnets makes this motor configuration an internal permanent magnet motor, which is a different research area. A major reason for studying reluctance motors is to learn how to harvest maximum magnet-free torque from them at all speeds; furthermore, eliminating magnets could become strategic in the future because of market trends.

Although these conclusions come from computations of a reluctance motor, they can be extended generically to modeling electric motors in general because most stators are similar and because saturation is unavoidable for high power densities.

Future Direction

Fruitful areas for further research on synchronous reluctance motors include developing ways to harvest additional torque. Approaches are to drive the motor with a nonsinusoidal waveform, to optimize the control for high-speed operation, and to match the effective number of stator turns to the speed and power requirements of the motor and explore how to switch the stator turns in and out of the circuit

during operation of the motor. It is expected that combining these approaches in a single design can meet the FreedomCAR performance targets as well as the cost targets.

Integrated design and modeling tools are needed to accurately compute the performance of a motor. Traditionally the interfacing between computer-aided drafting (CAD) and finite-element (FE) programs is limited to being able to import the CAD-created geometry to the FE software for analysis. Changes in the geometry require not only reimporting the drawing but also redefining properties, sources, and boundary conditions on the FE side. As a result progress has been slow and tedious. To overcome these interface problems, there is a new approach in which CAD and FE programs interact seamlessly so that changes in the CAD side are automatically incorporated into the FE side, and motor performance can be assessed quickly and effortlessly. Our experience has pointed toward the 64-bit operating system with SolidWorks CAD and COMSOL Multiphysics finite element packages as very promising for the simultaneous solution of electromagnetic, mechanical, and thermal equations of interest in motor design and evaluation computing.

Publications

P. J. Otaduy and J. W. McKeever, *Modeling Reluctance Assisted PM Motors*, ORNL/TM-2005/185, Oak Ridge National Laboratory, Jan. 2006.

References

1. T. J. E. Miller, *SPEED's Electric Motors*, University of Glasgow, 2002.
2. T. J. E. Miller, *SPEED CONSORTIUM PC-BDC Ver. 6 User's Manual,* University of Glasgow, May 1, 2002.
3. *COMSOL Multiphysics User's Manual*, Version 3.2, COMSOL, Inc., 2006.

3.5 Advanced Traction Motor Development

Principal Investigator: Sam Nelson
Oak Ridge National Laboratory
National Transportation Research Center
2360 Cherahala Boulevard
Knoxville, TN 37932
Voice: 865-946-1327; Fax: 865-946-1262; E-mail: nelsonscjr@ornl.gov

DOE Technology Development Manager: Susan A. Rogers
Voice: 202-586-8997; Fax: 202-586-1600; E-mail: Susan.Rogers@ee.doe.gov

ORNL Program Manager: Mitch Olszewski
Voice: 865-946-1350; Fax: 865-946-1262; E-mail: olszewskim@ornl.gov

---

Objectives

The objective of this task is the development of advanced traction drive motors that would not be pursued by industry alone because of the high risks and uncertainty of long-term earnings. The goal of this task is to develop an advanced traction drive motor with improvements in motor torque capability, efficiency, power density, and cost reductions that will meet the 2010 FreedomCAR goals.

Approach

As a result of a request for proposals, Unique Mobility, Inc. (UQM) was awarded a subcontract to design a state of the art motor to meet FreedomCAR targets. The approach by UQM was to consider the many motor topologies that have been used for traction drive applications, including brushed direct current (dc), permanent magnet (PM) brushless dc (BLDC), alternating current (ac) induction, switched reluctance, and synchronous reluctance machines. Each motor topology was assessed to determine the design that could best meet the 2010 FreedomCAR goals and traction motor technical targets. The advantages and disadvantages of each motor topology were considered, and it was determined that the PM BLDC has consistently demonstrated an advantage in terms of power density and efficiency. After the determination of the motor topology, a design trade study was performed to direct the design approach within that motor topology. A combination of finite-element analysis (FEA) and motor design equations was used to evaluate the design choices. A final design was solidified, and the expected performance of the design was determined.

Major Accomplishments

The technical report, *FreedomCAR Advanced Traction Drive Motor Development Phase 1*, was issued September 2006. This report documents the design effort and conclusions reached by UQM during the Phase 1 task. A 6 pole-pair machine with 36 slots in a 3-slot per pole configuration was determined to be the final design choice. The final design met or exceeded the majority of the 2010 FreedomCAR goals and traction motor technical targets.

Technical Discussion

Of the machine technologies, the PM brushless dc (PMDC) motor has consistently demonstrated an advantage in terms of power density and efficiency. A design trade study was performed for the PMDC motor to determine the motor configuration best suited to meet the motor requirements for the FreedomCAR specification. The three motor configurations that were evaluated in the trade study were the magnet-dominant internal PM machine (IPM), a reluctance-dominant IPM, and a surface-mounted PM machine (see Figure 1). Parametric finite-element models that define the geometry

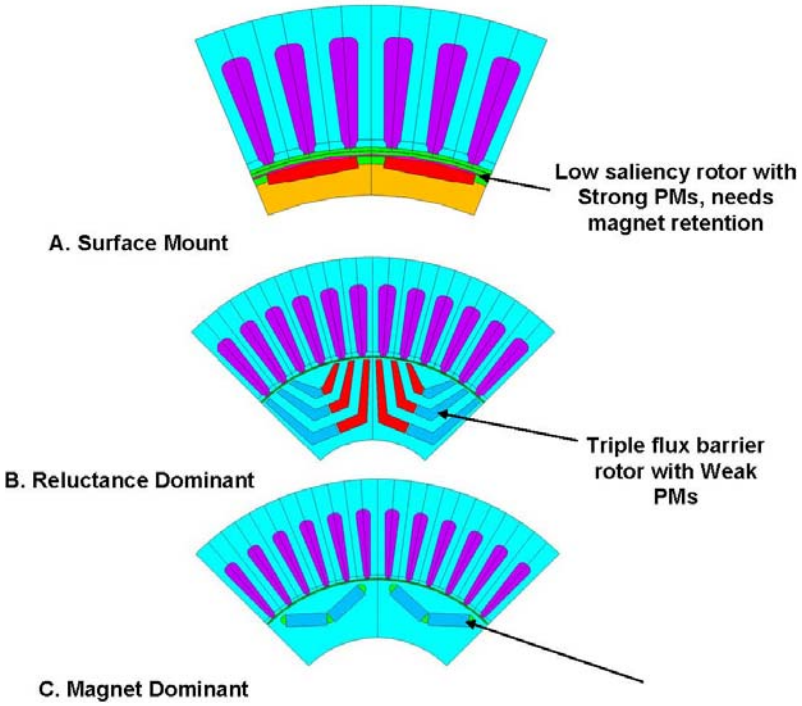

Figure 1. Physical topology, three designs.

of each configuration were created such that the geometry for each design could be quickly manipulated and reevaluated. FEA was used to evaluate motor parameters such as the back-emf constant (Ke) as well as the quadrature axis (q-axis) and direct axis (d-axis) inductance at a variety of currents. The flux density in the stator teeth and return path was also evaluated for use in calculating the iron losses. After the machine parameters were evaluated with FEA, a Mathcad model was used to simulate performance. The Mathcad model is based on the motor design equations and the equations for electric machine vector analysis. This model was used to predict motor performance by utilizing the motor parameters that were determined by FEA. This sequence of design iteration was chosen to provide a quick yet accurate method of design evaluation, given the geometry dependence on the motor parameters. The designs were iterated until each could meet as many of the FreedomCAR motor requirements as possible.

Trade Study

The purpose of the trade study was to identify a design direction for the FreedomCAR advanced traction motor and to identify aspects of each design that should be integrated into the advanced traction motor design. The results of the trade study indicated that the magnet-dominant design configuration would best fit the FreedomCAR specifications. Table 1 compares the performance predictions for each design with the FreedomCAR specifications. In Table 1, the values marked in red type indicate the performance predictions that did not meet the specification. The magnet-dominant design met all specifications except the peak power-to-volume specification (power density).

Table 1. Comparison of three design performances with specification

	Freedom Car Specification	Magnet Dominant Design MGDOM11	Reluctance Dominant Design REDOM	Surface Mount Design SURMO5
Top Speed (rpm)	10,000	10,000	10,000	10,000
325 Vdc (kW)	55	55	55	55
Battery Operating Range (V)	200-450	same	same	same
Nominal Battery Voltage (V)	325	same	same	same
Maximum Current at motor (Arms)	400	345	480	428
Characteristic Current (Arms)	<400	240.38	272.5	319.4
Efficiency at 10% of maximum Speed and 20% of Rated Torque (1000 rpm, 52.4 Nm)	>93	93.9	93.0	95.0
Efficiency at 20% of maximum Speed and 20% of Rated Torque (2000 rpm, 52.4 Nm)	>93	96.2	95.8	95.9
Efficiency at 100% of maximum Speed and 20% of Rated Torque (10,000 rpm, 52.4 Nm)	>93	95.4	97.2	92.7
Back-EMF at 100% of Maximum Speed (Vpeak, Line to Line)	<600	600	310	670
Peak Power to Volume Ratio (kW/Liter)	>12.5	10.4	8.8	10.0
Torque Pulsations % of peak Torque	<5	??	??	??
Peak Power to weight Ratio (kW/Kg)	>2.75	2.774	2.228	2.795

Magnet Cost Study

A magnet cost study was conducted to get an accurate picture of current magnet prices for NdFeB magnet materials from a variety of magnet sources, domestic and offshore. Because magnets are a relatively significant part of the total cost of a PM machine, it is beneficial to have good cost data for estimating manufacturing costs. UQM decided that the most accurate way to get cost data in volume is to have actual magnet suppliers quote a simple arbitrary shape in various volume quantities. After receiving the quotes, UQM calculated the magnet cost per pound from the official quotations. UQM requested quotes from magnet sources from the United States, Europe, Japan, and China. Also quoted were Chinese magnets distributed through a U.S. company and a U.S. company that processes finished magnets from Japanese magnet materials.

Each magnet manufacturer or distributor was given the same package of material and part specifications to quote pricing. The package included the drawing and magnetic material specifications. Each manufacturer or distributor was asked to quote each magnet specification in quantities of 10K/year to 100M/year. Each magnet manufacturer was asked to quote four different sets of material properties.

The magnet properties were chosen to a represent high-energy and a high-coercivity magnet in both a sintered and a bonded NdFeB magnet type.

The conclusion from the magnet cost study supports the conclusion from the trade study that the motor development effort should utilize sintered NdFeB magnets. The reason is that the cost per pound of high-coercivity sintered magnets is the same as that of bonded magnets (i.e., about $17 to $20 per pound). The trade study demonstrated that a motor with bonded magnets will utilize significantly more weight in magnets as well as total motor weight for the same performance level. This will significantly increase the cost for the motor.

Rotor Configuration Study

A rotor configuration study was performed with seven different rotor configurations. Characteristics that varied in the study were arranged for magnets (i.e., V-shape and U-shape), number of barriers (single or double), number of bridges (i.e., two, three, and four), and number of magnets per pole (two, three, and four). The stator arrangement, length of rotor, air gap, and current were constant for each configuration. The rotor configuration with U-shape barrier, two bridges, and three magnets per pole was determined to be the best configuration based on significantly more torque for the same size motor and same magnet mass. This rotor configuration will be slated for use in the final design (see Figure 2).

Many design iterations were generated in the development of the final design. The design iterations in this section illustrate the pros and cons of the possible pole count selections. Other design iterations that were not published were generated with a varying amount of analysis. For example, if the torque profile for a given design iteration was not acceptable, the design iteration would be dropped without further analysis. Analysis was performed on a given design iteration until it was found to be unacceptable or it was apparent that improvements could be made to meet the FreedomCAR specification.

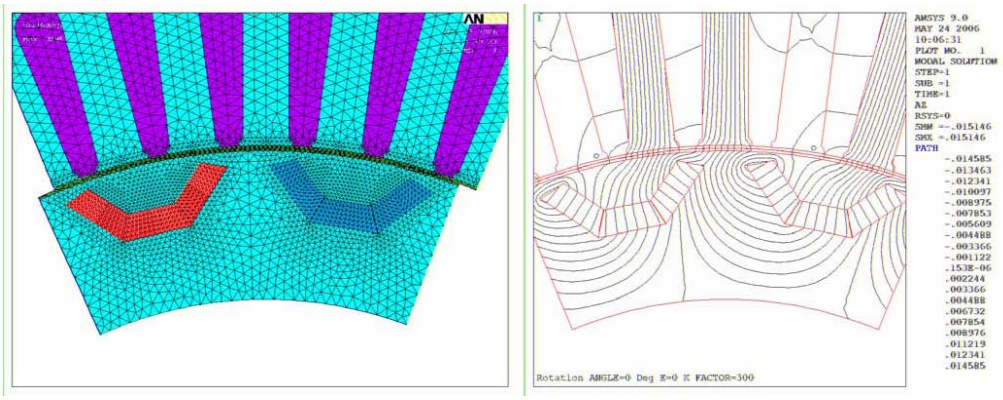

Figure 2. U-barrier, two bridges, three magnets per pole.

Iterative Design Method

All simulations in this section and following sections were conducted assuming an operating temperature of 150°C. This temperature was chosen as a target steady state design point, considering that 105°C is the required maximum inlet temperature and 150°C will allow for a reasonable temperature rise. All design iterations presented here were adjusted so that the maximum required torque, 262 Nm, was reached with 400 Arms leg current. The maximum allowable current according to the specification is 400 Arms. Designs were adjusted in length or turns to make 262 Nm at the maximum current to minimize the inductance and allow peak performance down to 200-V supply voltage. Higher turn counts and inductance will bring down the current but will not allow low-voltage operation.

Motor performance was predicted through means of evaluating the motor parameters, inductance profile (q- and d-axis inductance vs. current), and torque mapping in FEA. These values were then used in conjunction with vector analysis to predict motor performance. The performance models calculated the necessary current at a given operating point from the torque maps. The vector diagram was also evaluated for each point using the inductance values that corresponded to the current demand. The vector analysis determines what phase angle is necessary for operation at a given operating point and if the system will be voltage limited at that point.

The requirement for full-power operation down to 200 V of supply voltage drove the selection of many design features and contributed in determining the pole-pair selection as well. UQM took the approach that the highest pole count that would still allow the efficiency and power requirements to be met would lead to the most compact and power dense design, saving materials and cost. A higher pole count will nearly always give a net benefit in terms of power density so long as the other requirements can be accomplished, such as efficiency and the operating range for voltage, speed, and power.

Six-Pole Pair Design

Meeting the requirements of the specification at a higher power density, but a lower efficiency with the eight pole-pair design as compared with the four pole-pair design, prompted the study of pole-pair combinations between the two. The 6 pole-pair selection was a logical choice, having 36 slots in a 3-slot per pole configuration that allows a simple winding and relatively short end-turns. Iterations of the six pole-pair design led to the final design proving to have a better efficiency and power density than the designs with the other pole combinations.

Table 2 lists the important parameters of the six pole-pair design iteration that became the final design (see Figure 3). This combination yielded short end-turns (0.88 in.) and allowed a relatively short (3.4-in.)

Table 2. Motor parameters, six-pole pair, 3.4 in. (final design)

Overall stator diameter (in.)	8.7
Inner stator diameter (in.)	6.10
Rotor outside diameter (in.)	6.04
Stator stack length (in.)	3.4
End-turn length	0.88
Total axial length (over the end-turns) (in.)	5.165
Tooth thickness (in.)	0.380
Back-iron thickness (magnet return path) (in.)	0.39
Magnet strength (residual induction Br) (T)	1.10
Magnet thickness (in.)	0.165
Magnet weight (lb)	2.21
Minimum bridge thickness (in.)	0.04 (2 bridges)
Torque density (Nm/L)[a]	52.2
Power density (kW/L)[a]	11.0
Winding turns	3
Slots per pole	3
Back-EMF constant (Vpeak/krpm L-L)	47
Winding fill factor (%)[b]	74
Winding resistance (Ω L-L)	0.011
q-axis inductance (μH L-L)[c]	111
d-axis inductance (μH L-L)[c]	75

[a]Calculated using FEA at a 1200 ampere-turn load.
[b]Calculated using the conservative volume calculation.
[c]Includes insulation and copper in magnet wire based sum of square areas.

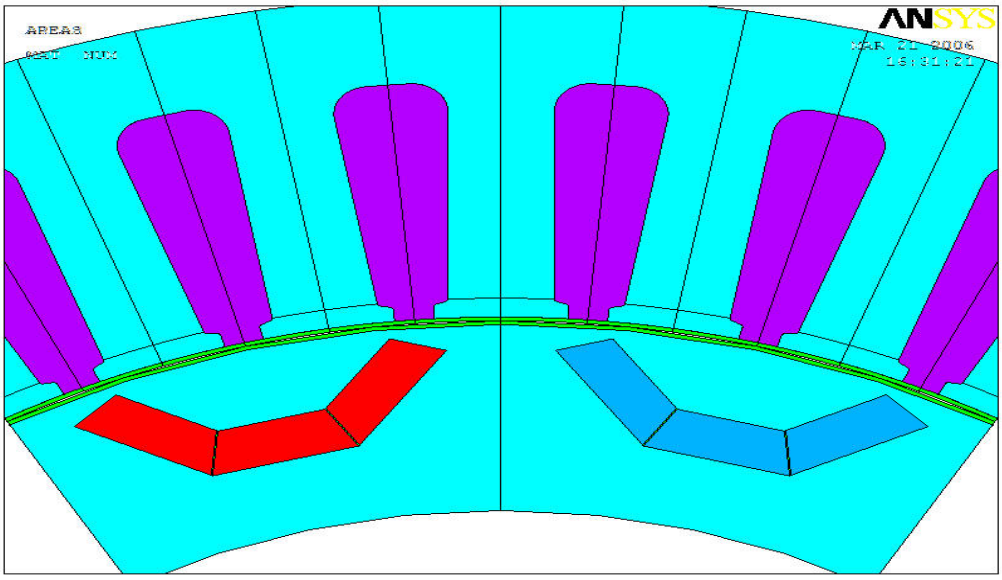

Figure 3. Six-pole pair machine configuration.

stack length as well. At 8.7-in. overall diameter and a total volume of 5 L, the power density is 11 kW/L, better than the design iterations in either of the other pole configurations.

Relatively wide stator teeth (0.380 in.) and back-iron (0.390 in.) reduced flux density and helped to control iron losses, giving good efficiency at high speeds. The motor will be 94.8% efficient at 1000 rpm and 95.6% at 10 krpm, well above the efficiency target of 93%. The peak efficiency, 96.5% is reached at about 4000 rpm and 52 Nm. Also, vector analysis indicated that operation at full power with a 200-V supply would be easily accomplished with this design. The minimum voltage for operation can be maintained below the buss voltage (Vdc) by phase advancing the current to a reasonable angle, and the current never exceeds the maximum allowable current of 400 Arms (see Figure 4).

The eight pole-pair version was able to meet most of the performance specs, but the girth of the iron in the magnetic circuit and the length had to be increased until the weight and volume were higher than expected. The tooth width and return path thickness had to be increased to lower flux density and therefore iron losses. Even so, this design barely met the 93% specification at 10 krpm. In addition, the turn count was dropped from three down to two to lower the inductance and allow performance down to 200 V. The length was increased to compensate for the loss of a turn. Although the end-turns are the shortest of all the designs (0.68 in.), the stack length was the longest (4.2 in.). Unfortunately, with the increased length, the power density of the machine was decreased, and the efficiency was reduced at high speeds. The eight-pole pair machines could not meet the required specification and were eliminated from consideration for the final machine design.

The four-pole pair configuration was evaluated; this configuration has been used in the Prius and other similar applications. The four-pole pair design was able to meet the performance specifications in terms of efficiency, peak power, and voltage range of operation. However, the resulting volume and weight were too high, making the power and torque densities low. Larger volume and weight are partially due to inherently longer end-turns and the requirement for thick stator features. More copper, iron, and magnet are necessary to compensate for less emf because of the lower-frequency operation in comparison to the higher pole counts. Additionally, because there is more magnet weight per pole, more structural support is needed to retain the magnets at high speeds. Consequently, the bridge thickness needed to be greater. With more bridges and/or thicker bridges, more magnet flux is shunted away from

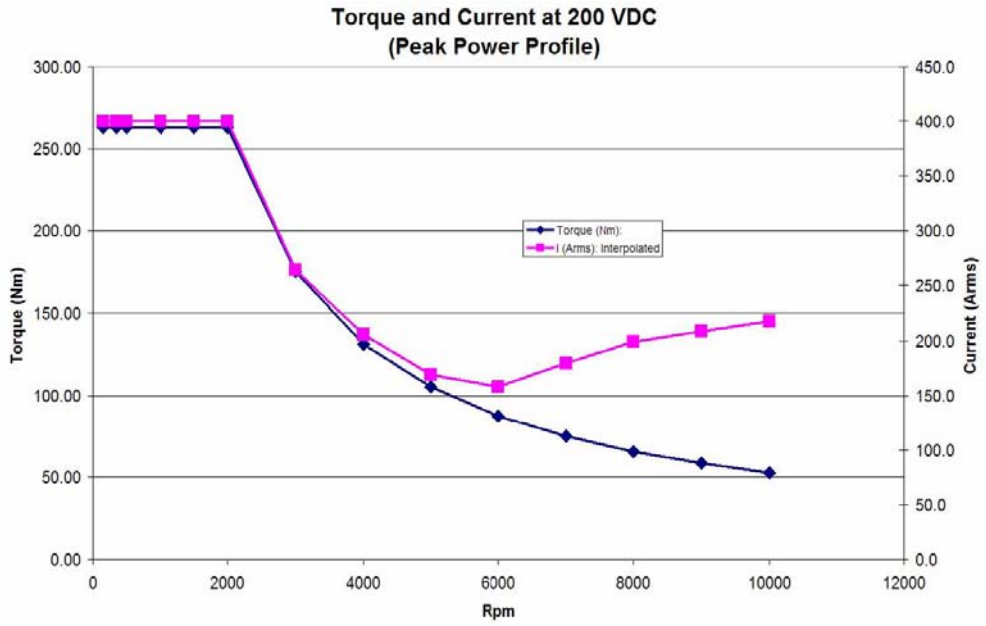

Figure 4. Current and torque profile at 200-Vdc, peak power.

the stator, reducing performance. The four-pole pair design met the efficiency requirements at 52 Nm across the speed range. The efficiency at 1000 rpm was slightly above 95% and slightly below 95% at 10,000 rpm. This four-pole pair design does meet the requirement for full power (i.e., 55 kW) at 200 V across the speed range and was eliminated from consideration for the final design.

During the Phase 1 design effort, pole-pair combinations between four- and eight-pole pairs were investigated. The six-pole pair configuration proved to be the best choice. Magnet weight was the lowest, and the power density was the best of the three: 11.0 kW/L for six-pole pairs, 10.4 kW/L for eight-pole pairs, and 8.6 kW/L for four-pole pairs. These power densities are based on conservative volume calculations.

Comparison with Prius Motor

The Prius motor is held in high regard in the industry and probably considered state-of-the-art in terms of electric propulsion motors for hybrid electric cars. For this reason, it makes sense to compare the motor design developed in this program with the Prius benchmark, in order to determine the value in continued development of this motor design. Because materials represent the most significant part of the cost in automotive volume production, size reduction is paramount. Figure 5 compares some of the major dimension and figures of merit of the two motors. In this section, all comparisons are made at the active materials level. Note that overall diameter and length are greatly reduced in the FreedomCAR design over the Prius motor design. Overall diameter of the Prius motor is 10.6 in., but the FreedomCAR design is only 8.7 in. The FreedomCAR design is nearly 2 in. smaller in diameter and down from 6.29 to 5.14 in. in overall length. Also, the reduction in the volume of the FreedomCAR design is approximately 40%, and weight is reduced by nearly 50% from the Prius motor. Some of this size reduction is due in part to the difference in operating profiles of the two motors. The FreedomCAR design makes more power, 55 kW as opposed to 50 kW for the Prius motor; however, the Prius motor operates in a lower speed range and

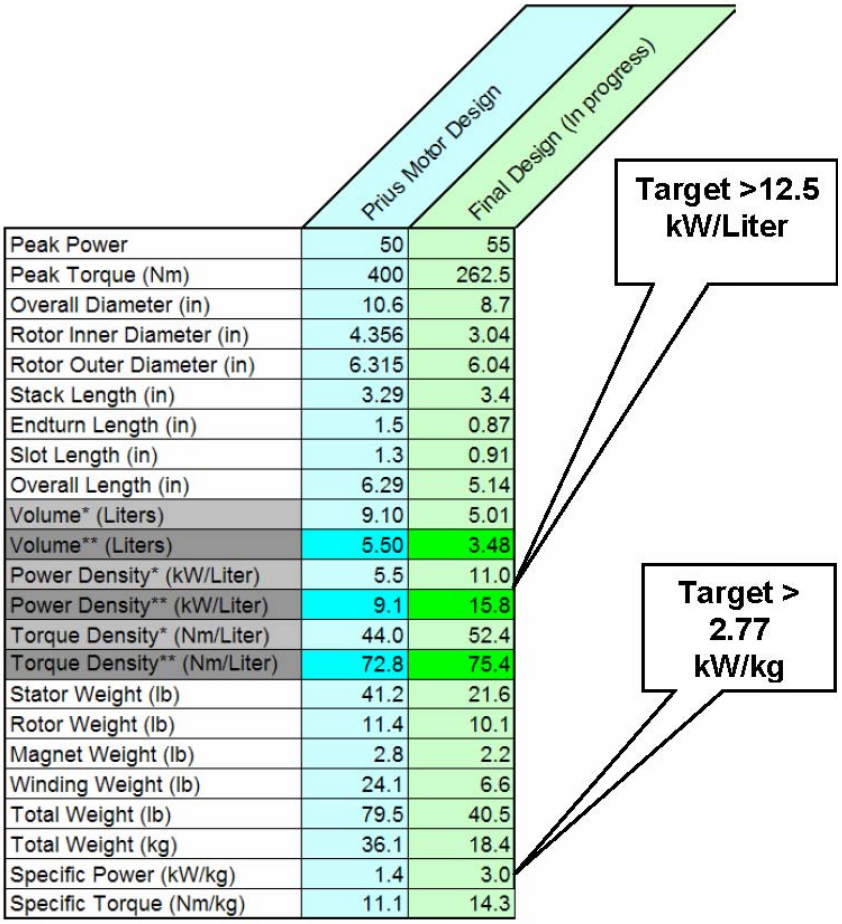

	Prius Motor Design	Final Design (In progress)
Peak Power	50	55
Peak Torque (Nm)	400	262.5
Overall Diameter (in)	10.6	8.7
Rotor Inner Diameter (in)	4.356	3.04
Rotor Outer Diameter (in)	6.315	6.04
Stack Length (in)	3.29	3.4
Endturn Length (in)	1.5	0.87
Slot Length (in)	1.3	0.91
Overall Length (in)	6.29	5.14
Volume* (Liters)	9.10	5.01
Volume** (Liters)	5.50	3.48
Power Density* (kW/Liter)	5.5	11.0
Power Density** (kW/Liter)	9.1	15.8
Torque Density* (Nm/Liter)	44.0	52.4
Torque Density** (Nm/Liter)	72.8	75.4
Stator Weight (lb)	41.2	21.6
Rotor Weight (lb)	11.4	10.1
Magnet Weight (lb)	2.8	2.2
Winding Weight (lb)	24.1	6.6
Total Weight (lb)	79.5	40.5
Total Weight (kg)	36.1	18.4
Specific Power (kW/kg)	1.4	3.0
Specific Torque (Nm/kg)	11.1	14.3

*Utilizes the most conservative method of calculating volume.
**Utilizes the least conservative method of calculating volume.

Figure 5. Power density comparison—FreedomCAR design vs Prius motor.

produces more torque, 400 Nm at 1200 rpm as opposed to 262 Nm at 2000 rpm for the FreedomCAR motor. Because electric motors scale with torque more closely than with power, note that the torque density of the FreedomCAR motor design is still 18% higher than that of the Prius Motor and its power density is 100% higher than that of the Prius.

The difference in motor parameters between the two machines includes a much higher back-emf voltage for the Prius motor, 141 as opposed to 48 Vpeak/Krpm (see Figure 6). This gives a maximum voltage of 480 V for the FreedomCAR design and 846 V for the Prius, necessitating a higher inverter voltage rating for the Prius system. Conversely, the Prius motor would require a lower current rating for the inverter, having a maximum motor current of 250 A, as opposed to 400 A for the FCVT motor.

	Prius Motor Design	Final Design (In progress)
Pole Pairs	4	6
Slots Per Pole	6	3
Back-EMF Constant @ 20 C	141.7	48
Resistance (Ohms L-L) at 20 C	--	0.011
Phase Inductance Lq (uH)*	--	111
Phase Inductance Ld (uH)*	--	75
Saliency Ratio	--	1.48
Slot Fill Factor	0.84	0.77
Residual Induction (T)	1.12	1.15
Maximum Current (Arms)	250	400
Maximum Speed (rpm)	6000	10000
Minimum Voltage	**200	200
Maximum Voltage	500	450
Max Operating Temp (Celcius)	170	>180
Magnet Retention Sleeve Required	No	No
Flux Barriers	V-Shape	U-Shape
Magnet Shapes	Rectangle	Rectangle

*Boost converter required to achieve this voltage range.

Figure 6. Motor parameter comparison—FreedomCAR design vs Prius motor.

Manufacturing Cost Estimate

UQM chose to estimate the cost of this machine in the most likely automotive production scenario, as a Tier 3 motor manufacturer supplying to a Tier 2 transmission manufacturer. As a result, the gearing cost is not included in the estimate, and the housing is at least partially integrated with the transmission as electric machines are presently being integrated in hybrid vehicles. UQM anticipates this transmission—electric machine integration trend to continue and therefore has chosen to estimate cost as a motor manufacturer would supply to the transmission manufacturer. The water jacket or heat sink is considered part of the motor, which will be included in the cost estimate. The water jacket will encompass the outer diameter of the stator laminations, and the assembly will be pressed into the transmission housing or bolted to the transmission housing as an attachment. The rotor is expected to be coupled and installed on one of the primary shafts of the transmission. Therefore, a hub that supports the rotor ring will be needed to adapt to the shafting of the transmission. Obviously, exact hardware would be application-specific; however, for the purpose of this cost study, a conceptual rendition of the applicable motor parts is depicted in Figure 7. This figure represents a good estimation of the necessary motor parts as supplied to a transmission manufacturer for electric machine integration within a transmission.

The parts and their estimated weights that were considered in this manufacturing cost analysis are listed in Table 3.

Material prices for copper, NdFeB, aluminum, and other materials were based on current market prices.

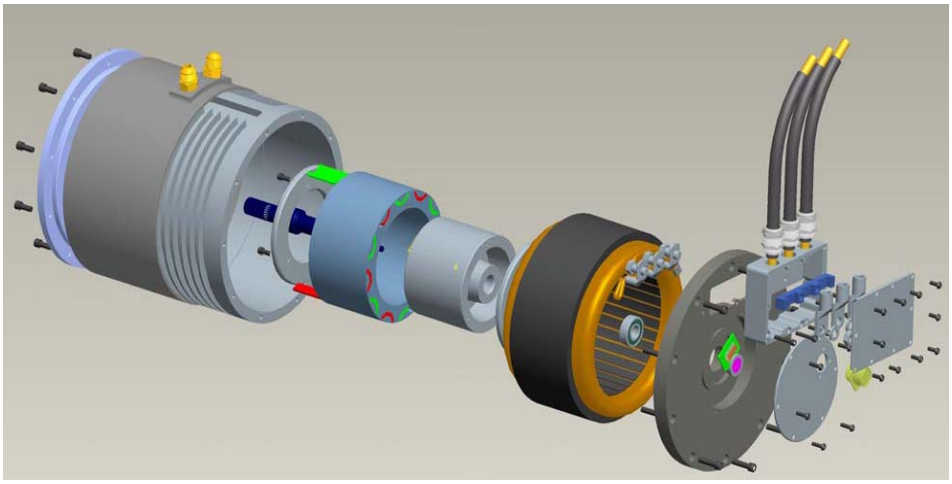

Figure 7. Motor assembly—exploded view.

Table 3. Parts included in manufacturing cost estimate

Part description	Weight of parts/unit (lb)
Stator lamination stack (243 laminations)	21.6
Rotor lamination stack (243 laminations)	10.0
Magnets NdFeB	2.215
Winding magnet wire (copper)	7.0
Bearings	2[a]
2 piece housing/water jacket (as cast)	5[a]
Stator finished (wound and insulated)	N/A
Rotor hub (as cast)	4[a]
Hub machining	N/A
Housing machining	N/A
Circuit board with position sensors (hall effects)	N/A

[a]Weights that are estimated, not actual values.

Figure 8, illustrates the results of the cost study generated by the UQM manufacturing group. The cost data presented here represent the cost of the motor and do not include tooling amortization or margin. The estimated unit prices are $399.60, $299.73, $239.78, and $203.85 at volumes of 100K, 250K, 500K, and 1M per year, respectively. The cost target for the 2010 specification was specified in at $7/kW. The chart also graphs the cost data in terms of cost/kW. The red horizontal line represents the cost target. At 55-kW peak power, the cost target is met for all quantities slightly over 100K units per year and above. As explained in the report, *FreedomCAR Advanced Traction Drive Motor Development-Phase 1*, the final design will actually be capable of up to 110 kW peak at nominal voltage and 4000 rpm. At 110 kW above 4000 rpm, the cost/kW is reduced well below the target.

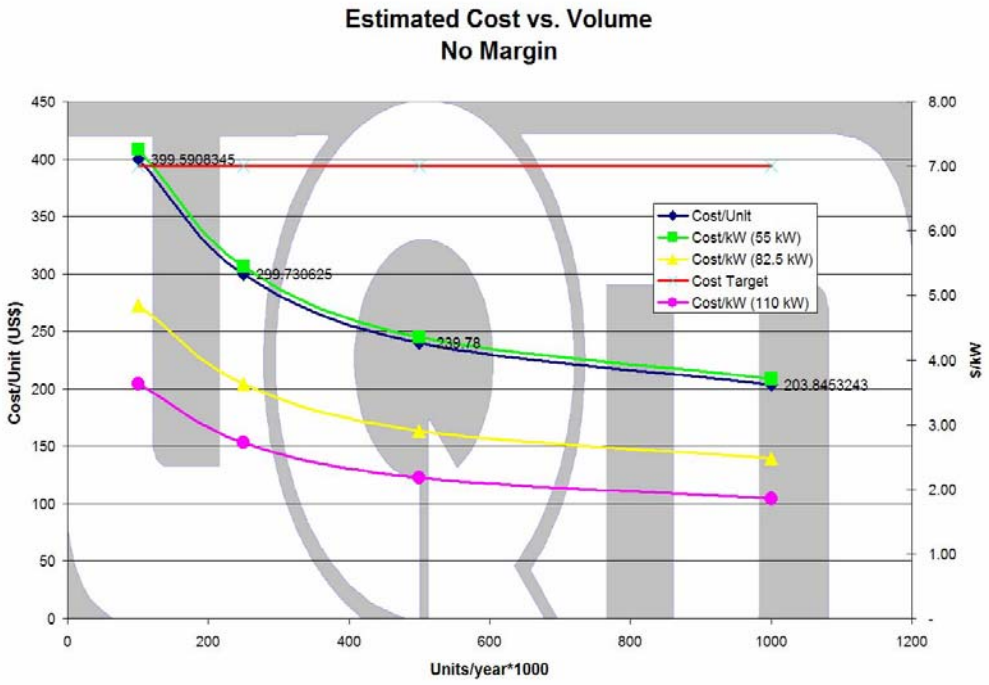

Figure 8. Cost vs volume for the FreedomCAR motor.

Conclusion

A six-pole pair configuration PM motor was determined to be the best choice for the FreedomCAR design. The rotor configuration has U-shaped barriers with two bridges per pole. The stator has 36 slots in a 3-slot per pole configuration that allows a simple winding and relatively short end-turns. Iterations of the six-pole pair design led to a final design with a better efficiency and power density than the designs with other pole combinations.

Table 4 compares the FreedomCAR target with the predicted performance for the FreedomCAR motor design. The motor meets or exceeds the target for power (i.e., continuous and peak) and efficiency. Because the peak power capability of the motor ranges from 55 kW at 2000 rpm to 110 kW at 4000 rpm, power density, specific power, and cost per kilowatt were calculated at both 55 and 100 kW.

Table 4. Comparison of FreedomCAR motor with target

Description	Predicted for FreedomCAR design	FreedomCAR target
Peak power (kW)	55–110[a]	55 kW
Duration at 55 kW (s)	40	18
Continuous power (kW)	30	30
Quantities based on active materials		
Power density (kW/L)—based on 55 kW	11–15.8[b]	>12.5
Power density (kW/L)—based on 110 kW	22–31.6[b]	>12.5
Specific power (kW/kg)—based on 55 kW	3	>2.75
Specific power (kW/kg)—based on 110 kW	6	>2.75
Cost per kW ($/k/W)—based on 55 kW	3.4–6.8[c]	<3.2
Cost per kW ($/k/W)—based on 110 kW	1.7–3.4[c]	<3.2
Quantities based on full motor package		
Power density (kW/L)—based on 55 kW	6.6	>5
Power density (kW/L)—based on 110 kW	13.3	>5
Specific power (kW/kg)—based on 55 kW	1.74	>1.3
Specific power (kW/kg)—based on 110 kW	3.47	>1.3
Cost per kW ($/k/W)—based on 55 kW	5–9.5[c]	<7
Cost per kW ($/k/W)—based on 110 kW	2.5–4.8[c]	<7
Other motor requirements		
Maximum current (Arms)	400	400
Back-EMF (V)	480	<600
Efficiency (%)	94.8–96.5	>93
Characteristic current (Arms)	344.6	<400
Maximum coolant temperature (ºC)	105	105

[a]Peak power is 55 kW at 2000 rpm, 82.5 kW at 3000 rpm, and 110 kW at 4000 rpm.
[b]The low end of the range is based on the most conservative volume calculation, and the high end of the range is based on the least conservative volume calculation.
[c]The range refers to the cost at 100k volume per year to the cost at 1M per year quantities.

Future Direction

This task completes the Phase 1 traction drive development task. Development of an advanced traction drive motor will continue with other tasks.

Publications

FreedomCAR Advanced Traction Drive Motor Development—Phase 1—September 2006, ORNL/TM-2006/UQM, Oak Ridge National Laboratory, September 2006.

3.6 Development of Improved Powder for Bonded Permanent Magnets

Principal Investigator: Iver E. Anderson
Metallurgy and Ceramics Program
Ames Laboratory, Iowa State University
Ames, IA 50011
Voice: 515- 294-9791; Fax: (515) 294-8727; E-mail: andersoni@ameslab.gov

DOE Technology Development Manager: Susan A. Rogers
Voice: 202-586-8997; Fax: 202-586-1600; E-mail: Susan.Rogers@ee.doe.gov

Program Manager: Mitch Olszewski
Voice: 865-946-1350; Fax: 865-946-1262; E-mail: olszewskim@ornl.gov

---

Objectives

- Increase the maximum operating temperature from 120 to 200˚C while maintaining desirable magnetic properties of permanent magnet (PM) materials to enable electric drive motors with improved operating characteristics.
- With goal of cost reduction for the new high temperature PM materials in electric drive motors, develop improved processing for bonded isotropic magnets produced by net-shape molding technologies for high-volume manufacturing.

Approach

- Develop innovative permanent magnet alloy design and processing technology for production of improved PM alloy powders for bonded isotropic magnets with a tolerance for high temperatures.
- Investigate PM alloy design improvements through melt-spinning methods, with the specific goal of developing an improved spherical magnet alloy powder through gas atomization processing.
- Develop an enhanced gas atomization process and a gas-phase powder surface reaction capability for simplified production and environmental protection of fine spherical powder for isotropic bonded magnets.
- Conduct experimental isotropic permanent magnet molding trials on as-atomized and annealed magnet powders to characterize isotropic bonded magnet properties and microstructures in collaboration with industrial partners, e.g., Arnold Magnetic Technologies (AMT) and Unique Mobility (UQM) and research partners, e.g., ORNL.

Major Accomplishments

- Achieved a further improvement of the room temperature maximum magnetic energy product, BH_{max}, with a reduced Co content (33% less) of our MRE-(Fe,Co)-B-TiC magnet alloy, demonstrating significant alloy cost benefits without any detectable decrease in magnetic performance up to 200C.
- Compression molded a large set of bonded magnet samples from a portion of the 100 kg commercial (Magnequench International) batch of magnet flake particulate (MQP-11HTP), formulated from an enhanced Ames magnet alloy design (WT-096), for the first stage of external testing of uncoated flake particulate.

- Successfully gas atomized the Zr + TiC modified MRE-Fe,Co-B magnet alloy with effective control of the composition and with the first demonstration of in-situ fluoride passivation (with NF_3), resulting in an energy product of 9.1 MGOe for a significant fraction (greater than 80% yield) of the spherical powder.
- Developed (and started atomization experiments on) a combined Zr and ZrC addition for the MRE-Fe,Co-B magnet alloy with phase nucleation and temperature stability properties more suitable than the previous Zr and TiC addition for direct translation to gas atomization of fine spherical powders for advantageous injection molding of bonded magnets.
- Confirmed the improved environmental stability with standard long term irreversible loss tests (LTILT) of bonded magnets that were compression molded with PPS at Ames Lab from as-received MQP-11HTP particulate and commercial MQP-14-12 particulate, where the LTILT testing was performed at Arnold Magnetic Technologies (AMT) and verified that our prototype (uncoated) powder matches the stability of the best commercial powders at 150C and provides enhanced magnetic performance at that temperature.
- Provided the second of two sets of net-shape isotropic bonded magnet samples to ORNL for testing in their experimental electric motor and in other devices to enable head-to-head comparisons, including high operating temperatures, of industrially bonded magnets (produced by AMT) made from commercial (MQP-type O) and experimental (MQP-11HTP) particulate, but testing problems have forced another partner to be sought.

Technical Discussion

Executive Summary

To meet performance and cost goals for advanced electric drive motors, it is essential to improve the alloy design and processing of permanent magnet (PM) powders. This project is expected to develop the materials and processes needed to fabricate high performance, isotropic bonded permanent magnets (PM) that can be used for traction motors with an internal PM rotor design. The fully developed PM material must be suitable for elevated temperature (180-200˚C) operation to minimize cooling needs, where the increased high temperature magnetic performance is more critical than room temperature magnetic properties. In addition to the importance of the magnetic alloy design for high temperature operation, a novel spherical powder production process, ideally with in situ powder coating capability, is a final project outcome. It should be noted that the starting alloy cost will be about the same as current alloys, but the powder production costs could be reduced and the total magnet material used per motor could be less, if motor design is optimized for bonded magnet use. Moreover, the spherical coated powder can promote manufacturing simplicity by reducing molding pressures and can enhance performance and reliability for the bonded magnets, through increased volumetric loading and reduced irreversible magnetic losses from oxidation and corrosion. The final project outcome is likely to be a significant reduction in the total manufacturing cost of PM traction motors, since isotropic bonded PM processing can utilize injection or compression molding technology in a net shape/assembly forming approach for mass production of internal PM rotors. These advantages should accelerate the widespread introduction of fuel-saving hybrids and could be claimed by the AEEPM program as a clear beneficial outcome.

Introduction

Permanent magnets based on RE2Fe14B intermetallic compounds, mostly Nd2Fe14B have had a large technological impact. Over the past 20 years, extensive research has been performed to develop and improve its magnetic properties. Commercially, two classes, aligned-sintered and isotropic nanocrystalline, Nd2Fe14B magnets have been successfully developed. It should be noted that aligned-sintered Nd2Fe14B magnets are used in current hybrid vehicle systems with motor designs that require high magnetic torque, but this magnet class and motor design have been judged to be impractical for very

large scale mass production at reduced cost. Alternatively, the opportunity exists to use a new motor design that utilizes reluctance torque, and, as such, is well suited to the reduced magnetic flux available (even at optimum) from bonded magnets.

To fully exploit this opportunity to switch to bonded magnets with great inherent advantage for mass production, one primary focus of this project is to develop an improvement of the existing magnet alloy that will enhance the performance of advanced motors that need high temperature tolerance. Current Nd2Fe14B magnet alloys exhibit excellent room temperature magnetic properties and they are well suited for applications with operating temperature at or below 120°C. However, the poor temperature stability of these magnets above 120°C limits their application for advanced drive motor designs. Although many approaches have been tried to improve high temperature properties of Nd2Fe14B magnets, the intrinsic properties of the Nd2Fe14B phase dictate large negative values of the temperature coefficients for coercivity and remanence. Consequently, it is necessary to find other compositions to improve the thermal stability of RE2Fe14B magnets. Recently, we have conducted a systematic study by melt spinning on magnetic properties of a series of isotropic nanocrystalline magnet alloys where a YDy-mixture replaces Nd or Pr as the primary RE constituent in MRE2Fe14B (MRE=Y+Dy+Nd). Our results show that the YDy-based MRE2Fe14B alloy can develop into isotropic magnets with superior magnetic properties above 125°C by a judicious mixture of Y, Dy, and Nd.

It should be noted that current Nd2Fe14B bonded magnets are produced from fragmented melt spun ribbon particulate with a flake morphology, and that the improved MRE2Fe14B alloy could be used as an immediate outcome to generate bonded magnets for experimental motor trials. In fact, this has been done recently within this project to help generate useful motor performance data to assess the benefits of the new alloy design. However, this flake particulate morphology has been judged unsuitable for optimum injection molding characteristics (critical for mass production of motor components) due to its excessive viscosity when heavily loaded into a polymer matrix. This results in molding pressures that are too high for practical use, requiring the magnet particulate loading to be reduced, which places an unacceptable upper limit on magnetic strength of the finished magnet. To overcome this limitation, the second primary focus of this project is to translate the enhanced alloy design that is being optimized for melt spinning to work with an alternative rapid solidification process, high pressure gas atomization (HPGA). The beneficial result of HPGA is a fine spherical powder which is known to have ideal (lowest viscosity) behavior in an injection molding process and, therefore, simplified molding of bonded magnets with increased magnetic strength. The challenge of translating the alloy design from melt spinning to HGPA lies in the differences in the heat transfer and the resulting solidification microstructure patterns between the two processes, although their average quenching rates are similar. Our latest results show the promise of using an alloy addition to promote direct nucleation of the most desirable phase in the HPGA powder, as will be discussed.

The challenge is to develop improved permanent magnet material for high-volume, low-cost production of advanced electric drive motors while meeting the system performance targets. As clearly stated in the APEEM Activity Plan of 2004, in the section on Electronics and Electric Machines and the subsection on Electric Motors and Generators (Task 2), we must perform this project to enable development of advanced motor materials and manufacturing processes to reduce costs. These lower-cost magnetic materials must be able to be implemented without sacrificing the performance of the drive motors.

Approach

Efficient screening of magnet alloy design modifications is accomplished by melt spinning methods, primarily using parameters (e.g., wheel speed of 10-16 m/s) that simulate the quenching rates accessible during gas atomization, the desired spherical powder processing method. A major aspect of

the project is the refinement of our design strategy for a family of novel MRE-Fe-B magnetic alloys (MRE = mixed rare earth, e.g., Y, Dy, Nd) to increase the remanence and energy product at ambient temperatures for isotropic PM material while maintaining superior temperature coefficient values to 200˚C, with commercial isotropic flake particulate and spherical atomized powder properties as benchmarks. The coupling of this melt spinning work with an increased number of gas atomization trials has accelerated the pace of alloy design specifically for the rapid solidification of fine spherical powders. During the last two years, the alloy design model for melt spinning (overquench to glass/anneal to nanocrystalline 2-14-1 phase) produced the MRE-Fe-Co-B-TiC (WT-096) that was selected for an industrial melt spinning batch. This particulate, called MQP-11HTP, was delivered by Magnequench International at the end of FY2005 and proved superior to the best commercial flake particulate (MQP-14-12) above 125C. Thus, for the last 18 months we could turn our attention to a specific alloy design model for gas atomized spherical powders (direct solidification to a nanocrystalline 2-14-1 phase, without annealing) and developed first an improved alloy, MRE-Fe-Co-B-TiC-Zr (WT-102) composition that was successfully gas atomized (GA-1-66) at the end of FY2005 and fully characterized during this year. Further alloy development for gas atomization produced MRE-Fe-Co-B-ZrC-Zr (WT-127) that replaced the TiC content with ZrC to enhance the crystallization potency for 2-14-1 phase. Gas atomization trials were partially successful at the high Zr level, truncated by apparent premature precipitation of ZrC in the atomizer nozzle. This result defined a direction, i.e., reduced Zr content, for continued work on this alloy type. It should be mentioned that a reduction in the Co level (reducing alloy cost) and an increase in the remanence and energy product while maintaining high temperature performance are all part of the current alloy design equation for the PM drive motor applications that can see operating temperatures up to 200C.

Comprehensive characterization of closely-related gas atomized and melt spun samples of a variety of promising MRE-Fe-B compositions continues as a strong emphasis in both as-solidified and annealed states. The initial magnetic characterization at both ambient and elevated temperatures is followed by x-ray diffraction and calorimetric characterization on all new samples. In addition, the bulk property measurements are clarified by microstructural observation with SEM, TEM, and 3-D atom probe (at HTML) to gain critical understanding about the product phase morphologies and spatial distributions that give rise to differences in as-solidified properties and in annealing response. After observing the similar microstructural basis for improved temperature stability (during annealing) of the magnetic properties of MRE-Fe-Co-B-TiC and MRE-Fe-Co-B-TiC-Zr and MRE-Fe-Co-B-ZrC-Zr alloys, we have continued searching for the mechanism that enhances nucleation of the 2-14-1 phase in melt spun ribbons and in the interior of atomized particles. Our overall goal is to explore the generality of MRE-Fe-B alloy rapid solidification behavior during gas atomization that minimizes glass formation and allows annealing to be avoided, because of the potential processing simplification advantage that can lead to reduced costs for bonded magnet production.

Some beneficial use has been made this year of the large (100kg) batch of annealed, flake particulate (MQP-11HTP) made from our improved MRE-Fe-Co-B-TiC alloy (WT-096) that was delivered at the end of FY2005. As reported in the results section a considerable quantity was blended with PPS polymer and compression molded in-house to provide a large set of samples for industrial bonded magnet testing at Arnold Magnetic Technologies (AMT) and for more detailed magnet characterization at ORNL. Since the flake particulate is already in a fully annealed state from the vendor, the immediate upscaling of the powder annealing capability is not needed. However, to enable this extensive work, the compression molding process was streamlined for fabrication of bonded magnet samples with conventional (about 60%) loading from a PPS binder blended with the new MQP-11HTP flake and with commercial PM particulate. This involved production of multiple heated die sets and other modifications. The industrial testing focused on short and long term exposure to high temperature environments and monitored the decay of magnetization. The ORNL testing utilized a hysteresis-graph and verified some in-house magnetic property characterization with a larger sample configuration. Extensive in-house development and testing at our partners of a protective coating for flake particulate

was delayed due to the need for significant up-scaling of our experimental coating capabilities. This up-scaling work expanded greatly (5-10X) the batch size of the current fluidized bed (fluorination) coating process, specifically intended to coat the flake particulate that is now available, as well as the spherical powder that will be produced from the improved alloys. Two experimental configurations, a gas-levitated or magnetically-stirred fluidized bed system and a horizontal rotating kiln system were designed and are in the fabrication stage. When completed early in FY2007, bonded isotropic magnet samples from fluoride coated commercial and experimental atomized powders will be provided to our industrial partner to compare the effect on reversible and irreversible magnetic loses. Also, at the request of ORNL, 20 kg of the as-received flake particulate (MQP-11HTP) was provided to AMT for industrial quality fabrication of bonded magnets that were precision machined for testing in a specific experimental PM motor system at ORNL. Unfortunately, funding limitations at ORNL prevented motor testing of these bonded magnets of this new high temperature alloy, in a direct comparison with an identical set of bonded magnets that were made from commercial MQP-14-12 particulate and delivered to ORNL in FY2005. Due to the extremely high value of such head-to-head testing of these two bonded magnet types that was recognized clearly by our peer reviewers, we will continue to seek this type of collaboration from other potential partners within the FreedomCAR program.

When an alloy is developed for gas atomization that has the same promise as the WT-096 alloy did for melt spinning, an up-scaling of gas atomization also will be needed to enable extensive injection molding process development with our recently installed compounding and injection molding equipment and in collaboration with AMT. As described above, a reasonably optimized alloy soon may be available, but another factor needed to be developed and verified to enable production of these modified MRE-Fe-B alloys as fine powder in our 5X scale gas atomization system and, eventually, in any commercial atomization system. This factor is adaptation of the fluorination process or another type of surface reaction/passivation approach for in situ treatment during the high-pressure gas atomization process to reduce the hazard and oxidation losses that are typical for powders with high surface area of this type of RE alloy. Our passivation process development built on the results of our post-atomization fluidized bed coating experiments and was extended to provide in-situ coating capability during the gas atomization process, using the atomization spray chamber of our research gas atomizer as a reaction vessel and the dispersed, high temperature state of the as-atomized powder spray as a natural fluidized (turbulent) state. This was explored by using the downstream addition of an NF^3-Ar gas mixture during the atomization process on two different experiments. The proper downstream location was determined by analysis of multiple process temperatures within the research atomizer chamber and by consideration of the spray chamber flow patterns and dynamic thermal conditions. The powder surface film effects were investigated by bulk oxygen content measurements, by air oxidation tests in a thermo-gravinometric analyzer (TGA), and by explosivity testing at an independent laboratory. If the current hazard reduction measurement (to a "moderate" explosivity level) can confirmed, both the larger scale and research scale atomization systems can be employed to produce prototype spherical powder batches that can be used for experimental injection molding trials. The resulting surface film structure and composition also was characterized by x-ray photoelectron spectroscopy (XPS), by Auger electron spectroscopy, and by microstructural analysis.

Results

The hard magnetic properties of any material are controlled by two sets of factors. The intrinsic properties of the hard magnetic phase, in our case $MRE_2TM_{14}B$, determine the saturation magnetization and magnetic anisotropy which are both temperature dependent, where MRE is a combination of Y, Dy and Nd, and TM is a combination of transition metals, primarily Fe and Co. Extrinsic properties, remnant magnetization and coercivity, are determined by the microstructure of the material which is in turn determined by the solidification process and thermal history of the material. These factors are significantly different for melt spinning and gas atomization. As demonstrated by the prototype

production of MQP-11HTP, based on $MRE_2TM_{14}B$ with TiC (WT-096), a magnet alloy microstructure can be very precisely controlled during melt spinning at normal (high wheel speed) ribbon production rates. Discussions with Magnequench about licensing of the new magnet alloy raised a question about the high cost of the Co in the TM portion and lead to a brief study of Co levels in the WT-096 alloy. Thankfully, it was found that a reduction of the Co level from TM = $(Fe_{12.5},Co_{1.5})$ to TM = $(Fe_{13},Co_{1.0})$, a reduction of 33% of the Co, actually improved the maximum magnetic energy product from 11.6 MGOe to 12.7 MGOe. Because of the Co reduction, the temperature coefficients for coercivity, $H_c(T)$, did not change, but the $B_r(T)$ did increase slightly to –0.078%/C, but this is still almost half of the benchmark commercial flake particulate, MQP-14-12. The effect of these differences in the optimized melt spun ribbon properties can be seen in Fig. 1, which shows the curves for the WT-096 (MS-FY2005) and the new low Co version (MS-FY2006).

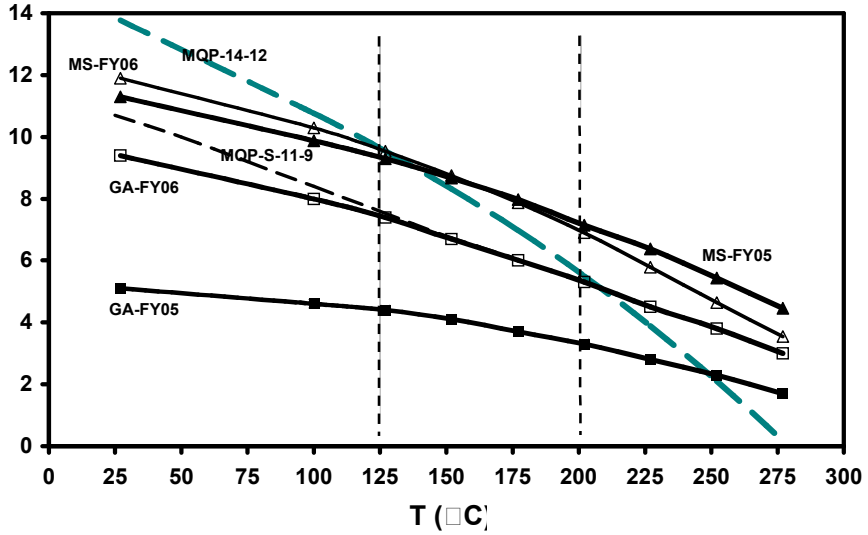

Figure 1. Comparison of the temperature dependence of maximum energy product for the experimental magnet alloys of this study as a function of the project year and of the type of processing, where MS is melt spun and GA is gas atomized, and the commercial benchmarks are listed by catalogue number, where MQP-S-11-9 is spherical (centrifugally atomized) powder and MQP-14-12 is melt spun.

This year, our magnet alloy development is focused primarily on microstructural control for the solidification conditions that exist during gas atomization, which is simulated by low speed melt spinning for this purpose, e.g., wheel speeds of 10, 13 and 16 m/sec. The microstructure of the as solidified ribbon is controlled by adjusting the chemistry of the alloy to influence the relative ease of nucleation of the competing phases during solidification. Alloy additions that control grain growth (once a phase has nucleated) also are employed to tailor the competition between nucleation and growth of the various phases. We have investigated these aspects by studying the effect of Zr substitution for MRE to enhance nucleation and by investigating additions of TiC and ZrC to control grain growth. The results for an improved gas atomized magnet alloy with Zr and TiC are shown in Fig. 1, as well, and more will be discussed about this alloy in the section below. Due to the similar structures and precipitation behavior of ZrC and TiC, it was expected that ZrC also could improve the as-solidified and annealed microstructure of both ribbons and powder. In addition, previous studies of Zr substitution for MRE show that Zr can change the crystallization behavior of ribbons or powder, apparently as an active solidification catalyst for 2-14-1 phase. Initial results on the effect of ZrC on magnetic properties in a base alloy with a fixed Zr substitution level, $[Nd_{0.45}(Y_2Dy_1)_{1/3*0.55}]_{2.2/17.3}Zr_{0.1}Co_{1.5}Fe_{12.5/17.3}B_{1/17.3}\}_{1-0.04}+Zr_xC_x$ resulted in very good magnetic properties for material melt spun at 16 m/sec. TEM images clearly showed that ZrC grains

(confirmed by convergent-beam electron diffraction) were formed along grain boundary regions (including triple-junction locations) with a grain size about 10 nm in diameter, or even less. The 2-14-1 phase microstructure has about 100 nm grain size. Hysteresis loops were generated of as-spun samples with x=0.01, 0.02 and 0.04. The addition of ZrC does not result in any serious decrease of saturation magnetization for these samples. The coercivity of these ribbon samples is in a very respectable range of 12.3 to 13.7 kOe. The remanence ranged from 6.6 to 6.8kG and the resulting energy product was 9.0 to 9.3MGOe, both very good for the as-solidified condition. Work to optimize the Zr and ZrC additions is on going.

Using the upgraded laboratory compression molding apparatus that was completed during this year, the initial set of 22 bonded isotropic magnets were compression molded with PPS polymer binder for extended environmental testing at AMT and ORNL. The particulate for this initial set was drawn from the large quantity of prototype commercial particulate, given the designation of MQP-11HTP by Magnequench International, as illustrated in Fig. 2.

Figure 2. Photograph of one of the packages that contained a total of 100 kg of industrially prepared flake particulate, formulated with the WT-096 magnet alloy composition.

The polymer processing temperature (slightly above melting) for the high temperature PPS (polyphenylene sulfide) polymer binder is approximately 300 C. Even with an inert processing atmosphere, the magnet material still must resist this aggressive environment during the molding process, in addition to possible long-term degradation during extended operation. We are currently developing a suitable surface fluorination process to provide protection (passivation) for flake particulate during compounding and molding at high temperature and to provide long term stability during high temperature bonded magnet use. This fluorination process is performed currently in a small (10 g capacity) gas flow reactor and incorporates magnetic stirring, gas mass flow control, and residual gas analysis for complete control of the process. The promise of this process was indicated last year when non-optimized fluorination parameters were used to produce 25 g of passivated WT-076 flake particulate that was bonded in PPS. The resulting bonded magnet was STILT tested at AMT and demonstrated about half of the Helmholtz field loss of a PPS bonded magnet made with commercial (uncoated) Magnequench

particulate at 200C. An investigation of controlled fluorination was initiated to determine the relationship between process parameters and coating thickness, using the highly controlled coating system and Auger electron spectroscopy (AES), but upgrades in the Auger signal analysis software must be completed before further progress can be made. Fortunately, x-ray photoelectron spectroscopy (XPS) was still useful for providing qualitative surface coating architecture information to help with our analysis of passivation in gas atomized powders (discussed below). Also, it was recognized that to provide a companion set of 22 compression molded bonded magnets to AMT for verification of the passivation effect; the small reaction vessel required a significant capacity upgrade. Thus, two alternative designs for scaled up batch processing of the fluoride coating layer were developed to compare the operating characteristics. Material to construct a larger fluidized bed reactor has been ordered. This reactor will allow 25-50 g of powder/flake to be fluorinated instead of only 10g in the current reactor and can use either a vertical-axis magnetic stirrer for flake or a gas distribution frit for spherical powder. The reaction vessel and drive train for a horizontal-axis rotary kiln reactor also have been completed. This reactor will process ~100g per batch of either flake or spherical powder without any modifications to the chamber. Both types of enhanced capacity will allow us to produce fluorinated bonded magnet samples to enable our industry partner, Arnold Magnetic Technologies, to perform STILT and LTILT measurements, which will be described below.

As reported last year, the first successful (operational) attempt at high pressure gas atomization of the MRE-Fe,Co-B magnet alloy with Zr and TiC additions did not exhibit improved magnetic properties, due to insufficient retention of Zr and B in the resulting fine spherical powder (GA-1-52). Thus, a repeat trial was performed with same starting parameters, but with boosted levels of Zr and B to compensate for anticipated losses. The resulting powder (GA-1-66) did exhibit an acceptable final composition and did produce improved magnet properties, especially in the powder with dia. < 20µm. It should be noted that particle size distribution analysis of the GA-1-66 powder batch showed that the average particle diameter is 8 µm and that about 80% of the total yield has dia. < 20 µm. A SQUID magnetometer trace of the hysteresis loop is given in Fig. 3, showing that annealing (700C, 15 min.) was required to transform the as-atomized powder microstructure into 2-14-1 phase with impressive magnetic properties, including a maximum energy product of 9.1 MGOe.

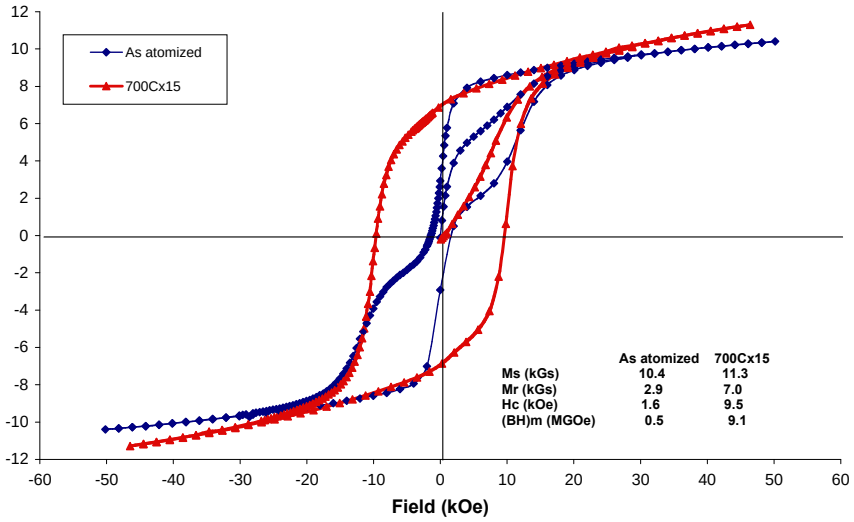

Figure 3. SQUID magnetization/demagnetization loop for the GA-1-66 powder with dia. < 20 µm.

One other significant accomplishment for the atomization experiment that produced the GA-1-66 powder batch was the successful downstream injection of Ar + 5%NF_3 gas to promote a fluoride reaction on the surface of newly-solidified particulate that were still at least 200C while freely falling in the spray chamber. Analysis of this first in situ passivation attempt was conducted initially by comparing the fluorinated powders from GA-1-66 to powders from GA-1-52, with our standard nitride and carbonaceous surface film reaction products. First, bulk tests of the average oxygen content were performed on the dia. < 45µm samples from each run. This test gives a metric for the total amount of oxide that forms on the particles following atomization. The average oxygen level for GA-1-52 was 1800ppm, a typical value for our magnet alloys under these conditions. For the in situ passivated material, GA-1-66, the average oxygen level was 585ppm. This significant decrease in oxygen indicates that we were successful at coating the resulting powder with a passivating (protective) layer of rare-earth fluoride or oxy-fluoride during atomization. For more detailed analysis of the coating, XPS was used to give highly surface specific chemical composition information that can detect F, Fe, O, and RE metals as discrete signals, unlike the more limited capabilities of AES. XPS measurements were made on samples of powder that had minimal exposure to air as well as those that had 24 h exposure to dry air. The results of these measurements indicated that an initial fluorine-containing layer is formed, probably not a pure $(RE)F_3$ compound, but likely to be a RE oxy-fluoride compound. When this layer was exposed to air, it remained a RE oxy-fluoride, but the oxygen content was increased. While the XPS measurements cannot quantify the thickness of the oxy-fluoride layer, the bulk oxygen analysis suggests that it is significantly thinner than the layer that forms without the passivating treatment. As an additional test of the passivation effectiveness, powders (dia. < 45 µm) of both the GA-1-52 and the fluorinated GA-1-66 powder were sent to a commercial laboratory to determine the minimum explosible concentration (MEC) of powder particles. In the MEC test, a higher concentration refers to a reduced explosibility hazard, an important property for powder handling and critical for successful technology transfer. The results given in Table 1 suggest that the passivated powder has a significantly reduced hazard and a consistent onset value, an improvement over the uncoated powder, but more such characterization will be needed on future powder batches to further quantify these results.

Table 1. A summary of the MEC test results for GA-1-66 powder with dia. < 45 µm.

MINIMUM EXPLOSIBLE CONCENTRATION (MEC):		**120-130g/m^3**		
Test No.	**Concentration (g/m^3)**	**Pressure (bar)**	**Rate of Pressure Rise (bar/s)**	**Ignition**
1	150	0.8	180	Yes
2	130	0.5	146	Yes
3	120	0.0	0	No
4	120	0.0	0	No
5	120	0.0	0	No

The translation of an alloy composition from melt spinning to gas atomization is complicated by not only the change in particle geometry, heat flow, undercooling potential, and cooling rate; but also by an increase in batch size of more than two orders of magnitude, a change in the crucible material, the complications of charge pre-alloying prior to atomization, and an increase in the superheat temperature required to reduce the melt viscosity when it passes through the pour tube. Increased superheat

temperature and possible crucible reaction can result in changes in the melt chemistry and produce unwanted secondary phases that are detrimental to the magnetic properties. Last year, the addition of TiC to the alloy resulted in attack on the typical crucible material (alumina) and a number of failed runs, before a crucible coating and a reduced superheat temperature permitted successful production of the GA-1-52 powder. These modifications and other alloy adjustments (see above) permitted atomization of the GA-1-66 powder and further trials with Zr and ZrC additions to the MRE-Fe,Co-B magnet alloy, which all included the new in situ passivation treatment. The resulting spherical powders were size classified, providing a complete range of particle size fractions for characterization by SEM, TEM, XRD, DTA, SQUID (magnetometer), and VSM. In our TEM studies of the gas atomized GA-1-66 powder microstructures, the as-atomized 20-25μm powder was predominantly nanocrystalline with a extremely fine grained (<3 nm) rim region and occasional 50nm interior grains, and a sub-optimum (20 nm) average grain size, very consistent with the reduced coercivity in the SQUID measurements for the as-atomized dia. < 20 μm powder in Fig. 3. After annealing at 700C for 15 min., the TEM results show (in Fig. 4) that the average interior grain size has increased to about 100nm and each particle retains an outer rim of about 50nm thickness with a 10nm grain size. Line scan analysis by EDS has demonstrated that there is no significant difference in composition between the rim and the interior region of these particles, i.e., the apparent sharp boundary seems to be only a remnant of the as-atomized quench history.

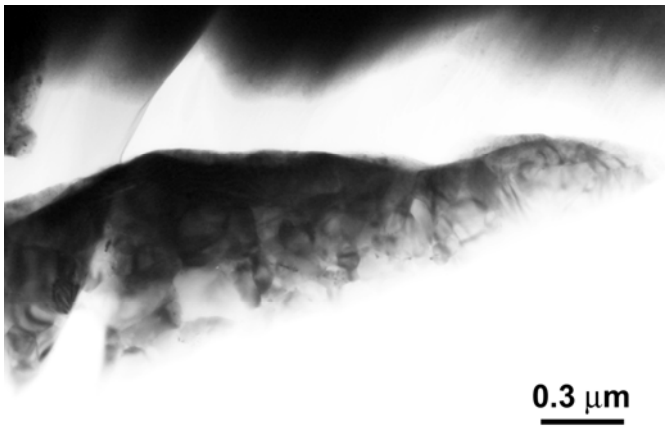

a)

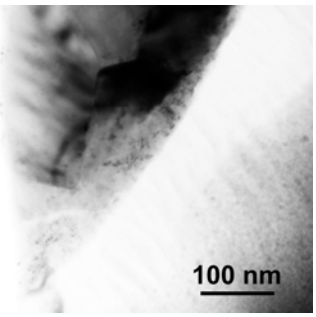

b)

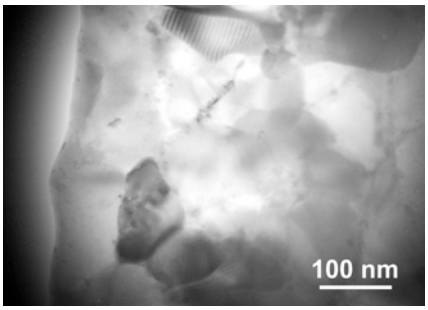

c)

Figure 4. TEM bright-field images of GA-1-66, 20–25 μm powder size, after annealing at 700˚C for 15 min, showing: a) a fragment of a spherical particle that contains both rim and interior

microstructures, b) a nanocrystalline rim layer of about 50 nm thickness formed at the exterior of the particle, and c) an increased grain size (~100 nm) inside the particle.

As result of the most recent alloy studies, a new (nominal) composition, WT-127, with Zr substitution and ZrC addition was developed: $\{[Nd_{0.45}(Y_2Dy_1)_{1/3*0.55}]_{1.9/17.3}Zr_{0.4/17.3}Co_{1.5/17.3}Fe_{12.5/17.3}B_{1/17.3}\}_{0.96}+Zr_{0.02}C_{0.02}$. The initial atomization experiment with this alloy was not a full operational success, since about half of the molten charge remained in the crucible due to an apparent blockage of the pour tube. Metallographic analysis, including optical microscopy and SEM (with EDS) allowed identification of premature precipitation of massive primary ZrC particles as the cause of the run termination. While future work will be focused on reduction of the apparent supersaturation condition without losing the beneficial nucleation effect, sufficient powder was produced to permit additional analysis as a function of powder size. The as-atomized dia. ≤ 5μm powder was mostly amorphous and highly spherical with a few irregular shapes. As-atomized spherical particles in the 10-15μm range exhibited a noticeable increase in (2-14-1 phase) crystallinity based on the amount of etching taking place, correlated with XRD and SQUID results. This size fraction was also investigated after annealing at 700°C for 15 minutes. The annealed samples contained multiple particles with large and highly faceted primary ZrC precipitates, consistent with the observation of pour tube blockage by the same particles. The best magnetic properties for GA-1-74 occur in the 5-15 μm powder, where an energy product of 5.9 MGOe was obtained for as-atomized powder. While not as high as GA-1-66 (see Fig. 3), no annealing was required to reach this level. In 20-45μm particles, a highly dendritic microstructure is seen throughout the matrix. This finding is consistent with some previous as-atomized powder, where particles typically above 20μm posses a dendritic and or cellular structure due to reduced solidification rates. XRD analysis of as-atomized and annealed GA-1-74 with a particle size of 10-15 μm show that the as-atomized sample is mainly composed of 2:14:1 and amorphous phases. After annealing at 700°C for 15 min., the sample exhibits a typical 2:14:1 structure. No other phases were detected. The new GA-1-74 powder, with a combination of Zr and ZrC obtained as-atomized magnetic properties enhanced over those of previous runs, but still below the as-solidified melt spun samples with the similar compositions, providing motivation for further study of this type of MRE-Fe,Co-B magnet alloy with Zr and ZrC additions.

A major goal of this project is the industrial validation of the alloys and coating processes that are being developed. This includes contracting for production scale melt spinning runs, making compression molded bonded magnets, and subjecting those magnets to industry standard tests. As reported above, a major step in this validation was the preparation of 100 kg of melt spun ribbon material by Magnequench International (MQI). Short term irreversible loss tests (STILT), performed by AMT were also reported previously and mentioned above. At this time it can be reported that long term irreversible loss tests (LTILT) on 22 compression molded bonded magnet samples made from unfluorinated MQP-11HTP and MQP-14-12 magnet alloy flake particulate have now been completed at AMT. As Fig. 5 illustrates, the long term stability of our materials matches that of currently available commercial material at 150 C. Thus the superior behavior of our alloy at this temperature is maintained after prolonged exposure to high temperature. Since the particulate material used in these test samples was in the uncoated condition, it is expected that the surface passivation process currently being developed will significantly enhance both the STILT and LTILT behavior.

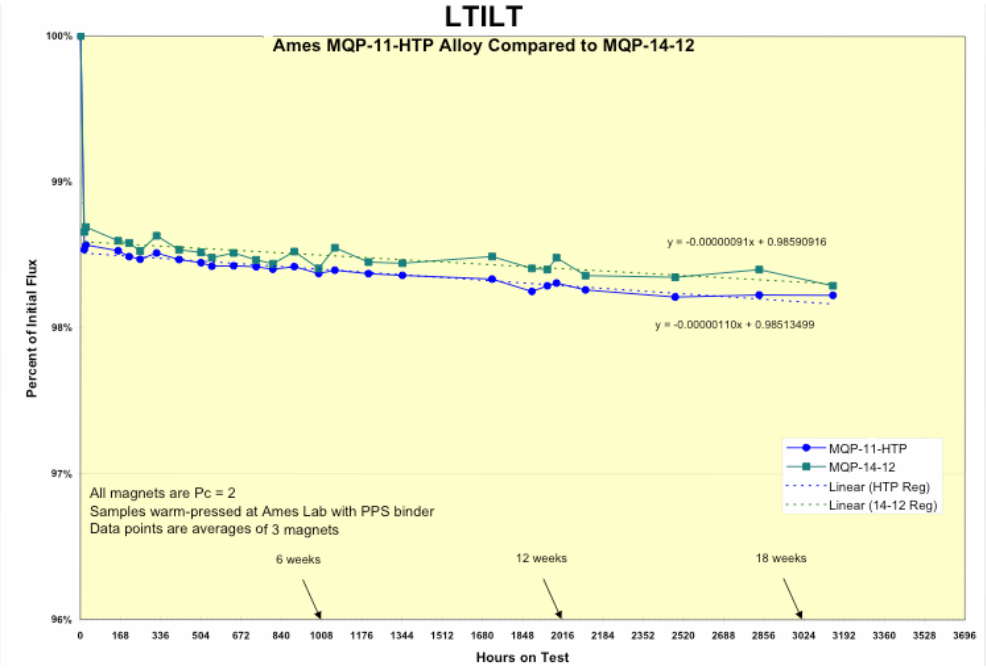

Figure 4. Summary of LTILT measurements performed by AMT that compare PPS bonded magnets made from uncoated MQP-11HTP and commercial MQP-14-12 flake particulate, showing essentially identical results out to 18 weeks.

Additional plans have proceeded for utilizing portions of our 100kg batch of melt-spun, annealed, and milled flake particulate, produced by Magnequench International (MQI) from our WT-096 alloy. These plans include collaborations with ORNL, Ford, and GM. In the plans with Ford, a new exploratory project has been developed that involves cold spray deposition of soft phase coated magnet alloy particulate.. Since Ford anticipates performance of a significant share of the experimental work and these processing experiments may develop new methods, a CRADA project is anticipated. The plans also include collaborations with GM for prototype motor testing, where Daimler-Chrysler may collaborate with GM in their efforts. In support of the motor design activity at ORNL, we reported last year on the production of PPS bonded magnets (produced by AMT from MQP-O type powder) designed for incorporation in the ORNL prototype motor. During the current year, a second identical set of magnets made from MQP-11HTP powder was produced also for the ORNL motor specifications to allow head-to-head bonded magnet tests. Unfortunately, we were informed by ORNL toward the end of the year that it was not possible to perform the motor tests at ORNL because of a shortage of funding. This circumstance has motivated a search for an alternative motor testing partner, with the possibility of re-machining the existing bonded magnets to fit a new rotor cavity design or starting the bonding and molding process over again with the available particulate to fit a new partner's requirements.

It is also worth noting that Ames Lab was instrumental in organization of a Motor/Magnet workshop at Ames during the current year, gathering many industrial and laboratory investigators for a 2-day set of discussions on strategies to move forward with collaborative efforts, where the presentations were collected on a C-D as a record (available on request). Another beneficial outcome was the shared recognition that the participants at this workshop should become more closely linked in future magnet development efforts. Moreover, during the year our ability to perform TEM studies on the spherical

powder was significantly enhanced at Ames Lab by the acquisition of two new pieces of equipment funded by the Office of Basic Energy Sciences, Department of Energy. Early in the year a new specimen thinning device termed a PIPS was purchased from Gatan Instruments The PIPS can operate its ion beam etching device at an extremely low angle, permitting much wider regions of thin area to be revealed in the powder particle cross-sections. Just prior to the end of the year, the installation of the state-of-the-art FEI Tecnai G^2 F20 scanning transmission electron microscope (STEM) also was completed.

Conclusions

During this year this project has achieved a further improvement of the room temperature maximum magnetic energy product, BH_{max}, with a reduced Co content (33% less) of our MRE-(Fe,Co)-B-TiC magnet alloy, demonstrating significant alloy cost benefits without any detectable decrease in magnetic performance up to 200C. A large set of bonded magnets were also compression molded from a portion of the 100 kg commercial (Magnequench International) batch of magnet flake particulate (MQP-11HTP) that was formulated from an enhanced Ames magnet alloy design (WT-096), for the first stage of external testing of uncoated flake particulate. The previous Zr + TiC modified MRE-Fe,Co-B magnet alloy also was gas atomized with effective control of the composition. This run was also the first demonstration of in-situ fluoride passivation (with NF_3), resulting in an energy product of 9.1 MGOe for a significant fraction (greater than 80% yield) of the spherical powder. A new magnet alloy design direction also lead to development of combined Zr and ZrC addition for the MRE-Fe,Co-B magnet alloy with phase nucleation and temperature stability properties more suitable than the previous Zr and TiC addition for direct translation to gas atomization of fine spherical powders for advantageous injection molding of bonded magnets. Confirmation also was obtained of improved environmental stability with standard long term irreversible loss tests (LTILT) of bonded magnets that were compression molded with PPS at Ames Lab from as-received MQP-11HTP particulate and commercial MQP-14-12 particulate. This LTILT testing was performed at Arnold Magnetic Technologies (AMT) and verified that our prototype (uncoated) powder matches the stability of the best commercial powders at 150C and provides enhanced magnetic performance at that temperature. The project also provided the second of two sets of net-shape isotropic bonded magnet samples to ORNL for testing in their experimental electric motor and in other devices to enable head-to-head comparisons, including high operating temperatures, of industrially bonded magnets (produced by AMT) made from commercial (MQP-type O) and experimental (MQP-11HTP) particulate. Unfortunately, testing problems have forced another partner to be sought.

Future Directions

Pursue the specific alloy design strategy for gas atomized spherical powders based on the novel MRE-Fe-B magnetic alloys (MRE = mixed rare earth, e.g., Y, Dy, Nd) that attempts to generate direct crystallization of the hard magnetic (2-14-1) phase with a desirable grain size in a dominant portion of the powder yield. Achieving this goal should lead to simplified (low-cost) processing and high yields of spherical isotropic magnet alloy powders with increased remanence and energy product at room temperature while maintaining superior magnetic performance to 200˚C, compared to commercial isotropic magnet alloy powder.

Continue comprehensive characterization of closely-related spherical powder and flake particulate samples of promising MRE-Fe-B compositions in both as-solidified and annealed states using magnetic, calorimetric, and microstructural methods to gain critical understanding of the linkage between rapid solidification structures and magnetic properties in gas atomization and melt spinning processes. This will enable successful translation of improved alloy designs from flake to spherical powders, which could be superior for injection molding of bonded magnets to net shape.

Perform comparison of flake and spherical powder in injection molding with initial series of lab injection molding trials on fine spherical powders and as-received flake particulate to determine practical upper range of magnet loading for both forms of magnet particulate without significant modification of the size distributions. Measure magnetic properties of bonded magnets with maximum loading.

Complete fabrication and testing of the up-scaled fluidized bed and rotating kiln processing options for batch fluorination of MRE-Fe-B alloy powder to enable selection of the best device for critical coating experiments that will lead to optimized protection of PM powders during magnet molding and bonded magnet use. The coating improvement experiments will include surface characterization and oxidation resistance testing of melt spun flake particulate and gas atomized spherical powders and should permit the full potential for high temperature use to be achieved with the new bonded magnets.

Collaborate with industrial partners, e.g., AMT, and research partners, e.g., ORNL, on an expanded range of environmental and magnetic testing for further study of bonded isotropic magnet samples produced by laboratory molding processes using fluoride-coated experimental flake particulate and spherical powders to facilitate direct comparisons with commercial flake particulate and spherical powders in coated and uncoated (as-received) forms, measuring progress against APEEM goals.

Seek appropriate partnerships to test bonded isotropic net shape magnets produced by industrial molding and fabrication processes using the prototype batch (MQP-11HTP) of flake particulate and commercial (e.g., MQP-14-12) flake particulate (coated and uncoated) in experimental motor designs in collaboration with industrial partners, e.g., Unique Mobility, or research partners, e.g., University of Wisconsin-Madison, to characterize motor performance and temperature tolerance, measuring progress against APEEM goals.

Continue development of the dynamic surface reaction (fluorination) approach to in situ passivation of the fine spherical MRE-Fe-B powders during the gas atomization process experiments that test improved magnet alloy designs. Successful development will result in minimal flammability and explosivity during the gas atomization process and will enable successful formation of an industrial partnership with a commercial powder producer.

Perform initial evaluation by a melt spinning approach of the compatibility of the MRE-Fe-B magnet alloy design to composition modification that produces a dual (soft/hard) phase “nanocomposite” magnetic microstructure with a suitable interphase spacing. If successful, the enhanced exchange coupling of bonded magnets produced from this nanocomposite flake particulate could generate a superior room temperature energy product that is maintained to 200C, completely surpassing commercial isotropic magnet alloy flake particulate.

Eventual plans are to explore methods to generate anisotropic MRE-Fe-B magnet alloy particulate using modified melt spinning processes and/or gas atomization approaches to facilitate a major boost in the magnetic energy product of bonded magnets.

Publications

P.K. Sokolowski, I.E. Anderson, W. Tang, Y.Q. Wu, K.W. Dennis, M.J. Kramer, and R.W. McCallum, “Microstructural and Magnetic Studies of Gas Atomized Powder and Melt Spun Ribbon for Improved $MRE_2Fe_{14}B$,” in *Advances in Powder Metallurgy and Particulate Materials-2006* , compiled by W.R. Gasbarre and J.W. von Arx (Metal Powder Industries Federation, Princeton, NJ, 2006), Part 9, pp. 152-167.

Wu, Y. Q.; Tang, W.; Miller, M. K.; Anderson, I. E.; McCallum, R. W.; Dennis, K. W.; Kramer, M. J. Microanalytical characterization of multi-rare-earth nanocrystalline magnets by transmission

electron microscopy and atom probe tomography. Journal of Applied Physics (2006), 99(8, Pt. 2), 08B515/1-08B515/3.

Xu, Youwen; Kramer, M. J.; Wu, Y. Q.; Dennis, K. W.; McCallum, R. W.. The mechanism of magnetic properties improvement and microstructure refinement of Zr in Nd2Fe14B. Journal of Applied Physics (2006), 99(8, Pt. 2), 08B511/1-08B511/3.

Tang, W.; Wu, Y. Q.; Dennis, K. W.; Kramer, M. J.; Anderson, I. E.; McCallum, R. W.. Effect of TiC addition on microstructure and magnetic properties for MRE2(Fe,Co)14B melt-spun ribbons (MRE=Nd+Y+Dy). Journal of Applied Physics (2006), 99(8, Pt. 2), 08B510/1-08B510/3.

Patents

None

References

R. W. McCallum, K. W. Dennis, B. K. Lograsso, and I. E. Anderson, "Method of Making Bonded or Sintered Permanent Magnets," U.S. Patent 5,240,513, August 31, 1993.

I. E. Anderson, B. K. Lograsso, and R. L. Terpstra, "Environmentally Stable Reactive Alloy Powders and Method of Making Same," U.S. Patent 5,372,629, December 13, 1994.

R. W. McCallum, K. W. Dennis, B. K. Lograsso, and I. E. Anderson, "Method of Making Bonded or Sintered Permanent Magnets (continuation)," U.S. Patent 5,470,401, November 28, 1995.

I. E. Anderson and R. L. Terpstra, "Apparatus for Making Environmentally Stable Reactive Alloy Powders," U.S. Patent 5,589,199, December 31, 1996.

I. E. Anderson, B. K. Lograsso, and R. L. Terpstra, "Environmentally Stable Reactive Alloy Powders and Method of Making Same," U.S. Patent 5,811,187, September 22, 1998.

R. W. McCallum and D. J. Branagan, "Carbide/Nitride Grain Refined Rare Earth-Iron-Boron Permanent Magnet and Method of Making," U.S. Patent 5,803,992, September 8, 1998.

R. W. McCallum and D. J. Branagan, "Carbide/Nitride Grain Refined Rare Earth-Iron-Boron Permanent Magnet and Method of Making," U.S. Patent 5,486,240, January 23, 1996.

D. J. Branagan and R. W. McCallum, "The Effects of Ti, C, and TiC on the Crystallization of Amorphous $Nd_2Fe_{14}B$," *J. Alloys and Compds.*, **245** (1996).

D. J. Branagan, T. A. Hyde, C. H. Sellers, and R. W. McCallum, "Developing Rare Earth Permanent Magnet Alloys for Gas Atomization," *J. Phys. D: Appl. Phys.*, **29**, p. 2376 (1996).

M. J. Kramer, C. P. Li, K. W. Dennis, R. W. McCallum, C. H. Sellers, D. J. Branagan, L. H. Lewis, and J. Y. Wang, "Effect of TiC Additions to the Microstructure and Magnetic Properties of $Nd_{9.5}Fe_{84.5}B_6$ Melt-spun Ribbons," *J. Appl. Phys.*, **83**(11), pt. 2, p. 6631 (1998).

D. J. Branagan and R. W. McCallum, "Changes in Glass Formation and Glass Forming Ability of $Nd_2Fe_{14}B$ by the Addition of TiC," *J. Alloys and Compds.*, **244** (1–2), p. 40 (1996).